SAINT PETERSBURG STATE UNIVERSITY



Khachatryan Andranik Shotaevich

# Magnetic properties of transition metal-doped topological materials

Scientific specialty
1.3.8. Condensed matter physics

Dissertation for the degree of
Candidate of Physical and Mathematical Sciences

*Translation from Russian*

Research advisor:
Doctor of Physical and Mathematical science, professor
Charnaya Elena Vladimirovna

Saint Petersburg – 2025

# Table of contents

# Introduction

Significant attention to topological materials doped with magnetic impurities is driven by promising new applications in spintronics, as well as fundamental interest in the stability of certain non-trivial topology of electronic bands. Transition metals can induce ferromagnetic or antiferromagnetic order types in the bulk of topological materials, breaking the symmetries that ensure non-trivial band topology.

Doping with transition metal atoms can lead to modification of surface states in topological materials, significantly influencing their transport properties [1-6]. Magnetically induced order through doping also promotes the emergence of the quantum Hall effect and the anomalous quantum Hall effect [7-11]. The presence of magnetic order plays a crucial role in the problem of creating molecular rotors [12]. Consequently, diamagnetic topological materials such as topological insulators and Weyl semimetals doped with transition metals are being actively investigated.

Three-dimensional topological insulators (TIs), such as $Bi_{1-x}Sb_x$, $Bi_2Se_3$, $Bi_2Te_3$, and others, whose topological features are due to strong spin-orbit coupling and band inversion, are characterized by a finite energy gap in the bulk and a zero gap at the surface. The non-trivial band topology in TIs is ensured by time-reversal symmetry. The spin of electrons on the surface is rigidly coupled to their momentum, which provides polarization of surface states during charge transfer [1, 13]. Breaking time-reversal symmetry by applying a magnetic field or doping with paramagnetic impurities opens up the possibility to control transport spin polarization and observe new phenomena, such as topological quantum phase transition [7, 9]. $Bi_2Te_3$ and $Bi_2Se_3$ dichalcogenide crystals belong to the class of "strong" three-dimensional TIs, i.e., possessing the property of maintaining their topological properties even in the presence of some defects [1, 14, 15]. It was predicted that doping these crystals with 3d transition metal ions would lead to the formation of long-range magnetic order [9, 16-20]. Furthermore, recent theoretical calculations have shown that some 4*d* elements and non-magnetic impurities can also induce ferromagnetism in TIs [21-24].

Ferromagnetism in doped $Bi_2Te_3$ and $Bi_2Se_3$ dichalcogenides can be due to the participation of free charge carriers, but it can also exist without their involvement [22].

Weyl semimetals (WSMs) also belong to three-dimensional topological materials [2, 3, 25, 26], where the non-trivial topology of electronic bands arises due to band inversion resulting from strong spin-orbit coupling. This is associated with the breaking of time-reversal symmetry (*T*-symmetry) [28-30] or the breaking of inversion symmetry of the crystal lattice (*P*-symmetry) [31-34], as well as with the existence of pairs of gapless Weyl points with opposite chirality in the bulk Brillouin zone of WSMs. The surface Brillouin zone contains Fermi arcs that connect the projections of Weyl nodes [2]. It has been suggested that non-centrosymmetric tungsten ditelluride $WTe_2$ and molybdenum ditelluride $MoTe_2$, mixed ditellurides $Mo_xW_{1-x}Te_2$ [35-43], and the Heusler alloy LaAlGe [44] belong to type II WSMs. Although the classification of $WTe_2$ as a WSM was initially doubted [45], recent studies have confirmed its non-trivial topological nature [41, 46-48].

Like bismuth selenide, tungsten ditelluride was well known as a good thermoelectric material before it was classified as a WSM [49]. With temperature changes, $WTe_2$ also demonstrated a Lifshitz transition [50], non-saturated magnetoresistance, likely related to hole and electron compensation [51, 52], and anisotropic nonlinear magnetoresistance [53]. Recently, a ferroelectric phase was experimentally discovered in two-dimensional $WTe_2$ [54]. In [55], it was shown that the structure and symmetry in $WTe_2$ can be dramatically altered by special optical excitation. Great interest was aroused by the behavior of $WTe_2$ monolayers, which demonstrated strain-induced transition to a topological phase [56], excitonic insulator properties [57], and the anomalous Hall effect in a heterostructure with a ferromagnetic insulator [58].

From the above discussion, it follows that magnetic studies of $Bi_2Se_3$ and $WTe_2$ single crystals doped with transition metals, particularly iron and chromium, demonstrate a variety of properties that require new information to understand their relationship with crystal composition and growth conditions. Detailed investigation of the doping effects on the magnetic properties of topological insulators and Weyl semimetals is essential for developing new electronic devices with enhanced functional characteristics. It is important to examine the stability of magnetic phases and the possibility of their control through magnetic field application. The research findings on doped topological materials open new opportunities for tuning electronic properties, which can have significant implications for applications [59-62]. However, to determine promising directions, it is necessary to study a broader range of various doped topological materials.

Thus, **the main objective of this dissertation can be briefly formulated** as the investigation of magnetic and thermal properties of magnetically doped TIs based on bismuth selenide and WSM tungsten telluride across a wide range of magnetic fields and temperatures. In accordance with this objective, the following **tasks** were set:

1. To verify the single crystallinity and perfection of the crystal structure, as well as the homogeneous distribution of magnetic impurities in TI samples of $\mathbf{Bi_{2-x}Fe_xSe_3}$ (**x=0.006; 0.03; 0.06**), $\mathbf{Bi_{2-x}Cr_xSe_3}$ (**x=0.01; 0.03; 0.06**) and WS $\mathbf{Fe_{0.03}W_{0.97}Te_2}$.
2. To identify the existence and nature of magnetic ordering in single crystals of TI $\mathbf{Bi_{2-x}Fe_xSe_3}$ (**x=0.006; 0.03; 0.06**), $\mathbf{Bi_{2-x}Cr_xSe_3}$ (**x=0.01; 0.03; 0.06**) and WS $\mathbf{Fe_{0.03}W_{0.97}Te_2}$ through the investigation of magnetic properties and heat capacity of the samples across a wide range of temperatures and magnetic fields.
3. To determine the temperatures of magnetic phase transitions and their evolution under external magnetic fields in single crystals of TI $\mathbf{Bi_{2-x}Fe_xSe_3}$ (**x=0.006; 0.03; 0.06**), $\mathbf{Bi_{2-x}Cr_xSe_3}$ (**x=0.01; 0.03; 0.06**) and WS $\mathbf{Fe_{0.03}W_{0.97}Te_2}$. To establish the temperature dependence of coercivity for these samples.
4. To investigate the possibility of magnetic field-induced phase transitions in doped TI and WS samples.

To address the stated objectives, the following **investigations** are required:

1. Testing of TI $\mathbf{Bi_{2-x}Fe_xSe_3}$ (**x=0.006; 0.03; 0.06**), $\mathbf{Bi_{2-x}Cr_xSe_3}$ (**x=0.01; 0.03; 0.06**) and WS $\mathbf{Fe_{0.03}W_{0.97}Te_2}$ using a *Bruker D8 DISCOVER* X-ray

diffractometer, *DRON-2.0* X-ray diffractometer, and Tescan Mira scanning electron microscope equipped with an *Oxford Instruments INCA x-act EDS* detector.

2. Measurement of temperature-dependent magnetization of TI $\mathbf{Bi_{2-x}Fe_xSe_3}$ (**x=0.006; 0.03; 0.06**), $\mathbf{Bi_{2-x}Cr_xSe_3}$ (**x=0.01; 0.03; 0.06**) and WS $\mathbf{Fe_{0.03}W_{0.97}Te_2}$ single crystals using a *SQUID MPMS 3 Quantum Design* magnetometer in the temperature range of 1.8 – 400 K, magnetic fields up to 70 kOe, and orientations $\mathbf{c} \parallel \mathbf{H}$ and $\mathbf{c} \perp \mathbf{H}$.
3. Measurement of field-dependent magnetization of TI $\mathbf{Bi_{2-x}Fe_xSe_3}$ (**x=0.006; 0.03; 0.06**), $\mathbf{Bi_{2-x}Cr_xSe_3}$ (**x=0.01; 0.03; 0.06**) and WS $\mathbf{Fe_{0.03}W_{0.97}Te_2}$ single crystals using a *SQUID MPMS 3 Quantum Design* magnetometer in the temperature range of 2 – 400 K and magnetic fields from -70 to +70 kOe, with the crystallographic **c**-axis oriented parallel and perpendicular to the external magnetic field.
4. Heat capacity measurements of TI $\mathbf{Bi_{2-x}Fe_xSe_3}$ (**x=0.006; 0.03; 0.06**) and WS $\mathbf{Fe_{0.03}W_{0.97}Te_2}$ single crystals using a *PPMS-9+Evercool II Quantum Design* relaxation calorimeter in the temperature range of 1.8 – 400 K and magnetic fields from 0 Oe to 1 kOe.
5. Theoretical investigation of the crystal lattice stability of WS $\mathbf{WTe_2}$ when doped with transition metals.

**The scientific and practical significance** of this dissertation is determined by the acquisition of new data on the magnetic properties of topological materials doped with transition metals. The results obtained within the framework of this dissertation can be applied in magnetoelectronics research, particularly in the development of new classes of magnetic topological insulators and Weyl semimetals, and other materials with unique properties.

The magnetic susceptibility data of doped topological materials are used in the investigation of phase transitions associated with changes in magnetic order. The data obtained, described, and systematized within this dissertation will contribute to more accurate prediction of similar materials' properties and the creation of new materials with desired characteristics, which is crucial in the design of new materials and devices.

The materials studied in this work may find practical applications in magnonics, quantum computers, or other high-tech devices due to their unique combination of physical properties. The obtained results will be valuable in expanding the applications of topological materials in various technological processes and devices, including magnetic devices and nanoelectronics. The dissertation results can also be utilized in the educational process for science students in lecture courses or practical training sessions.

**Scientific Novelty**:

1. The magnetic susceptibility of TI $\mathbf{Bi_{2-x}Fe_xSe_3}$ (**x=0.006; 0.03; 0.06**), $\mathbf{Bi_{2-x}Cr_xSe_3}$ (**x=0.01; 0.03; 0.06**) and WS $\mathbf{Fe_{0.03}W_{0.97}Te_2}$ single crystals has been thoroughly investigated for the first time in the temperature range of 1.8-400 K. Significant anisotropy in magnetic properties has been discovered in the samples. The coexistence of different types of magnetic ordering has been revealed.
2. Data on the coercivity of TI $\mathbf{Bi_{2-x}Fe_xSe_3}$ (**x=0.006; 0.03; 0.06**), $\mathbf{Bi_{2-x}Cr_xSe_3}$ (**x=0.01; 0.03; 0.06**) and WS $\mathbf{Fe_{0.03}W_{0.97}Te_2}$ single crystals have been obtained for the first time. Anomalies have been detected and correlated with phase transitions observed in the temperature-dependent magnetic susceptibility curves.
3. Metamagnetism has been observed for the first time in TI $\mathbf{Bi_{2-x}Cr_xSe_3}$ (**x=0.03; 0.06**) and WS $\mathbf{Fe_{0.03}W_{0.97}Te_2}$, identified through the investigation and analysis of magnetization hysteresis loops at different temperatures.
4. Sequential low-temperature phase transitions in WS $\mathbf{Fe_{0.03}W_{0.97}Te_2}$ have been observed for the first time.
5. Temperature-dependent diamagnetism has been observed for the first time in WS $\mathbf{WTe_2}$, presumably attributed to the topological nature of the sample's electronic bands.

The **credibility** of the experimental findings is established through the utilization of contemporary research infrastructure and their agreement with previously reported scientific observations in the relevant literature.

**Validation of the Work**. The main findings of the study were presented and discussed at five conferences – *XXIII All-Russian Youth Conference on Semiconductor and Nanostructure Physics, Semiconductor Opto- and Nanoelectronics*, St. Petersburg, Russia, 22–26 November 2021; *XXIV Ural International Winter School on Semiconductor Physics, Yekaterinburg*, Russia, 14–19 February 2022; *IX International Youth Scientific Conference Dedicated to the 100th Anniversary of the Birth of Professor S. P. Raspopin*, Yekaterinburg, Russia, 14–19 February 2022; *XIX Conference "Strongly Correlated Electronic Systems and Quantum Critical Phenomena"*, Moscow, Russia, 26 May 2022; *VII Conference of the Euro-Asian Symposium "Trends in MAGnetism"*, Kazan, Russia, 22–26 August 2022.

**Personal Contribution of the Author**

The main research results presented in this dissertation have been published in scientific articles and conference proceedings, listed at the end of this work. The preparation of materials for publication was carried out in collaboration with co-authors, where the author's contribution was decisive and constituted no less than 70 percent.

The author conducted all investigations of magnetic and thermal properties of TI bismuth selenide and WS tungsten telluride single crystals doped with magnetic impurities, in conjunction with experimental equipment operators. The author independently performed the processing of experimental results and their interpretation within the framework of modern theoretical concepts, and wrote draft versions of articles and conference presentations.

The approaches, methods, and obtained results presented in the dissertation were discussed jointly with the scientific supervisor, E. V. Charnaya, who provided overall guidance and task formulation. Co-authors E.V. Shevchenko and M.V. Likholetova participated in measuring the magnetic moment and heat capacity of single crystals. Co-authors A.O. Antonenko, M.K. Lee, and L.-J. Chang participated in discussions of the obtained results for magnetic susceptibility, magnetization, and heat capacity of single crystals. V.V. Marchenkov, A.N. Perevalova, and S.V. Naumov conducted the single crystal growth work.

**Publications.** The main findings related to the dissertation topic are presented in three published articles in journals indexed in both the *Scopus* and *Web of Science* citation databases:

1. Shevchenko, E. V. Magnetic Properties of Iron-Doped $Bi_2Se_3$, a Topological Insulator / E. V. Shevchenko, A. Sh. Khachatryan, A. O. Antonenko, E. V. Charnaya, S. V. Naumov, V. V. Marchenkov, V. V. Chistyakov, M. K. Lee, L.-J. Chang // Phys. Solid State – 2019. – Vol. 61. - № 6. – P. 1037 – 1042.
2. Khachatryan, A. Sh. Coexistence of magnetic states and metamagnetism in the $Bi_{2-x}Cr_xSe_3$ topological insulators / A. Sh. Khachatryan, E. V. Charnaya, E. V. Shevchenko, M. V. Likholetova, M. K. Lee, L. J. Chang, S. V. Naumov, A. N. Domozhirova, V. V. Marchenkov // Europhysics Letters. – 2021. – Vol. 134. - № 4. – P. 47002.
3. Khachatryan, A. S. Magnetic Studies of Iron-Doped Probable Weyl Semimetal $WTe_2$ / A. S. Khachatryan, E. V. Charnaya, M. V. Likholetova, E. V. Shevchenko, M. K. Lee, L.-J. Chang, S. V. Naumov, A. N. Perevalova, E. B. Marchenkova, V. V. Marchenkov // Condensed Matter – 2023. – Vol. 8. - № 1. – P. 6.

**Dissertation Structure.** The dissertation comprises an introduction, six chapters, the principal findings, a list of the author's publications on the dissertation topic, and a list of cited references.

**Chapter 1** provides a brief overview of the dissertation topic, examining the characteristics of topological insulators and Weyl semimetals, as well as magnetic states in solids. Additionally, this chapter includes a review of studies focused on the magnetic properties of specific topological insulators and Weyl semimetals.

**Chapter 2** describes the sample preparation methods and experimental approaches used in the research. It details the melt crystallization and chemical vapor transport methods, equipment, and techniques for sample testing and analysis.

**Chapter 3** presents the research findings on the magnetic properties of $Bi_{2-x}Fe_xSe_3$ single crystals. This chapter provides detailed descriptions of magnetic phase transitions, coercivity anomalies, and strong magnetic property anisotropy in these samples.

**Chapter 4** describes the investigation of magnetic properties in $Bi_{2-x}Cr_xSe_3$ single crystals. This chapter emphasizes antiferromagnetic and ferromagnetic ordering, low-temperature coercivity anomalies, and paramagnetism. The dependence of these properties on chromium content is examined. The possibility of metamagnetic phase transitions in certain $Bi_{2-x}Cr_xSe_3$ samples, attributed to collectivized electrons, is discussed.

**Chapter 5** examines the specific magnetic properties of iron-doped tungsten telluride single crystals in comparison with undoped $WTe_2$. The chapter explores the effect of annealing on ferromagnetic ordering and the detection of anomalies related to antiferromagnetism and paramagnetism. For the unannealed $Fe_{0.03}W_{0.97}Te_2$ sample, a phase transition due to itinerant metamagnetism is described.

**Chapter 6** presents density functional theory calculations for the $WTe_2$ unit cell and $Cr_{0.03}W_{0.97}Te_2$ and $Fe_{0.03}W_{0.97}Te_2$ supercells. The chapter evaluates the stability of supercells when doped with transition metals.

The Conclusion lists the main results of this work. At the end, a list of primary publications related to the dissertation and a bibliography of cited literature are provided.

**Main Results of the Dissertation:**

1. Temperature dependencies of magnetic susceptibility and magnetization isotherms of $\mathbf{Bi_{2-x}Fe_xSe_3}$ (**x=0.006, 0.03, 0.06**), $\mathbf{Bi_{2-x}Cr_xSe_3}$ (**x=0.01, 0.03, 0.06**), and $\mathbf{Fe_{0.03}W_{0.97}Te_2}$ single crystals were experimentally obtained over a wide range of temperatures (1.8 – 400 K) and magnetic fields (±70 kOe). Significant anisotropy of magnetic properties was discovered in the studied samples for magnetic field directions along and perpendicular to the crystallographic **c**-axis (**c** || **H** and **c** ⊥ **H**) [**103**] (pp. 1037 – 1042), [**113**] (pp. 47002-p1 – 47002-p6), [**124**] (pp. 1 – 12).

2. It was shown that in **$Bi_{2-x}Fe_xSe_3$** (**x=0.006, 0.03, 0.06**), competition between ferromagnetism and antiferromagnetic correlations plays an important role, which is attributed to two magnetic phase transitions (see [**103**] pp. 1038).

3. Experimental data on coercivity of **$Bi_{2-x}Fe_xSe_3$**, **$Bi_{2-x}Cr_xSe_3$**, and **$Fe_{0.03}W_{0.97}Te_2$** single crystals were obtained for the first time. Several anomalous features were revealed in the coercivity curves for **$Bi_{2-x}Fe_xSe_3$** (**x=0.006, 0.03, 0.06**) and **$Bi_{2-x}Cr_xSe_3$** (**x=0.01, 0.06**) single crystals (see [**103**] pp. 1041, [**113**] pp. 47002-p4).

4. In the course of research on **$Bi_{2-x}Cr_xSe_3$** (**x=0.01, 0.03**) and non-annealed **$Fe_{0.03}W_{0.97}Te_2$** single crystals, metamagnetism was discovered, manifesting as the opening of magnetization hysteresis loops with increasing external magnetic field. The shape of the field-dependent magnetization corresponded to the phenomenon of itinerant metamagnetism, caused by charge carriers (see [**113**] pp. 47002-p5, [**124**] pp. 5).

5. During the investigation of magnetic properties of **$Fe_{0.03}W_{0.97}Te_2$** single crystal, a sequence of several phase transitions at temperatures below 40 K was discovered for the first time. These transitions indicate a complex nature of magnetic ordering (see [**124**] pp. 6).

6. It was shown that the temperature dependence of magnetic susceptibility in undoped **$WTe_2$** crystal has a minimum at 80 K, which can be explained by the topological nature of electronic bands (see [**124**] pp. 5).

7. It was shown that effective magnetic moments of iron impurities in **$Bi_{2-x}Fe_xSe_3$** (**x=0.006; 0.03; 0.06**) single crystals and annealed **$Fe_{0.03}W_{0.97}Te_2$** indicate mixed **$Fe^{+3}$** and **$Fe^{+2}$** valence states. In **$Bi_{2-x}Cr_xSe_3$** (**x=0.01; 0.03; 0.06**) single crystals, ions with **$Cr^{+2}$** valence are present (see [**103**] pp. 1039, [**113**] pp. 47002-p4, [**124**] pp. 6.

**Main Statements for Defense**:

1. Topological insulators **$Bi_{2-x}Fe_xSe_3$** (x=0.006; 0.03; 0.06) and **$Bi_{2-x}Cr_xSe_3$** (x=0.01; 0.03; 0.06), as well as the Weyl semimetal **$Fe_{0.03}W_{0.97}Te_2$**, exhibit coexistence

of ferromagnetic ordering and antiferromagnetic correlations within specific temperature ranges.

2. The anomalous decrease in coercivity observed in $\mathbf{Bi_{2-x}Fe_xSe_3}$ (x=0.006; 0.03; 0.06) and $\mathbf{Bi_{2-x}Cr_xSe_3}$ (x=0.01; 0.06) single crystals below 30 K results from partial disruption of magnetic order.

3. Topological insulators $\mathbf{Bi_{2-x}Cr_xSe_3}$ (x=0.03; 0.06) and Weyl semimetal $\mathbf{Fe_{0.03}W_{0.97}Te_2}$ exhibit metamagnetic behavior.

4. The minimum in magnetic susceptibility at 80 K for pure Weyl semimetal $\mathbf{WTe_2}$ is a consequence of the topological nature of its electronic structure.

5. Iron ions in $\mathbf{Bi_{2-x}Fe_xSe_3}$ (x=0.006; 0.06) and $\mathbf{Fe_{0.03}W_{0.97}Te_2}$ single crystals, as well as chromium ions in $\mathbf{Bi_{2-x}Cr_xSe_3}$ (x=0.01; 0.03; 0.06) single crystals, exhibit mixed valence states.

# Chapter 1. Review

This chapter provides a concise overview of the dissertation topic. The first section presents general information about topological insulators and Weyl semimetals. The second section examines fundamental concepts of magnetic states in solids: diamagnetism, paramagnetism of dilute magnetic systems, and magnetic phase transitions, along with a brief discussion of crystal heat capacity theory. The third and fourth sections provide a literature review of research works focused on the magnetic properties of transition metal-doped topological insulators $Bi_2Se_3$, $Bi_2Te_3$, and the Weyl semimetal $WTe_2$, respectively.

## 1.1 Concepts of Topological Insulator and Weyl Semimetal

### 1.1.1 Topological Insulators

Topological insulators (TIs) represent a class of compounds characterized by an electronic energy gap in their bulk and a vanishing gap at their surface [1]. In TIs, surface states with wave vector **k** feature electron spins perpendicular to their momentum lying in the crystal surface plane (Fig. 1.1a) [5]. Strong spin-orbit interaction establishes a rigid coupling between momentum direction and electron spin on the TI surface. Thus, the presence of strong spin-orbit interaction distinguishes TIs from trivial insulators. Under the influence of strong spin-orbit coupling, an inversion of conduction and valence bands occurs (Fig. 1.1b) [4]. This distinguishes TIs from Dirac semimetals, which lack an inverted phase due to insufficient spin-orbit coupling strength (Fig. 1.1c). Surface electrons in TIs maintain stable conductivity even in the presence of moderate defects and behave as Dirac fermions. In TIs, the non-trivial band topology is protected by time-reversal symmetry (*T*-symmetry) [1]. The properties of three-dimensional TIs were first experimentally observed in bismuth dichalcogenides: $Bi_{1-x}Sb_x$, $Bi_2Se_3$, and $Bi_2Te_3$. These crystals belong to the class of narrow-gap semiconductors with bulk band gaps of $E_g \approx 0.1 – 0.3$ eV. Such band gap values allow the preservation of topological properties even at room temperature. Observation of TI topological properties is performed using angle-resolved photoemission spectroscopy (ARPES). $Bi_2Se_3$ and $Bi_2Te_3$ crystals are classified as "strong" TIs due to their ability to maintain their topological properties in the presence of moderate defects (Fig. 1.1d) [1].

### 1.1.2 Weyl Semimetals

Topological semimetals include both Dirac and Weyl semimetals. The topological Dirac state emerges at the critical Fermi-surface point between trivial and topological insulators.

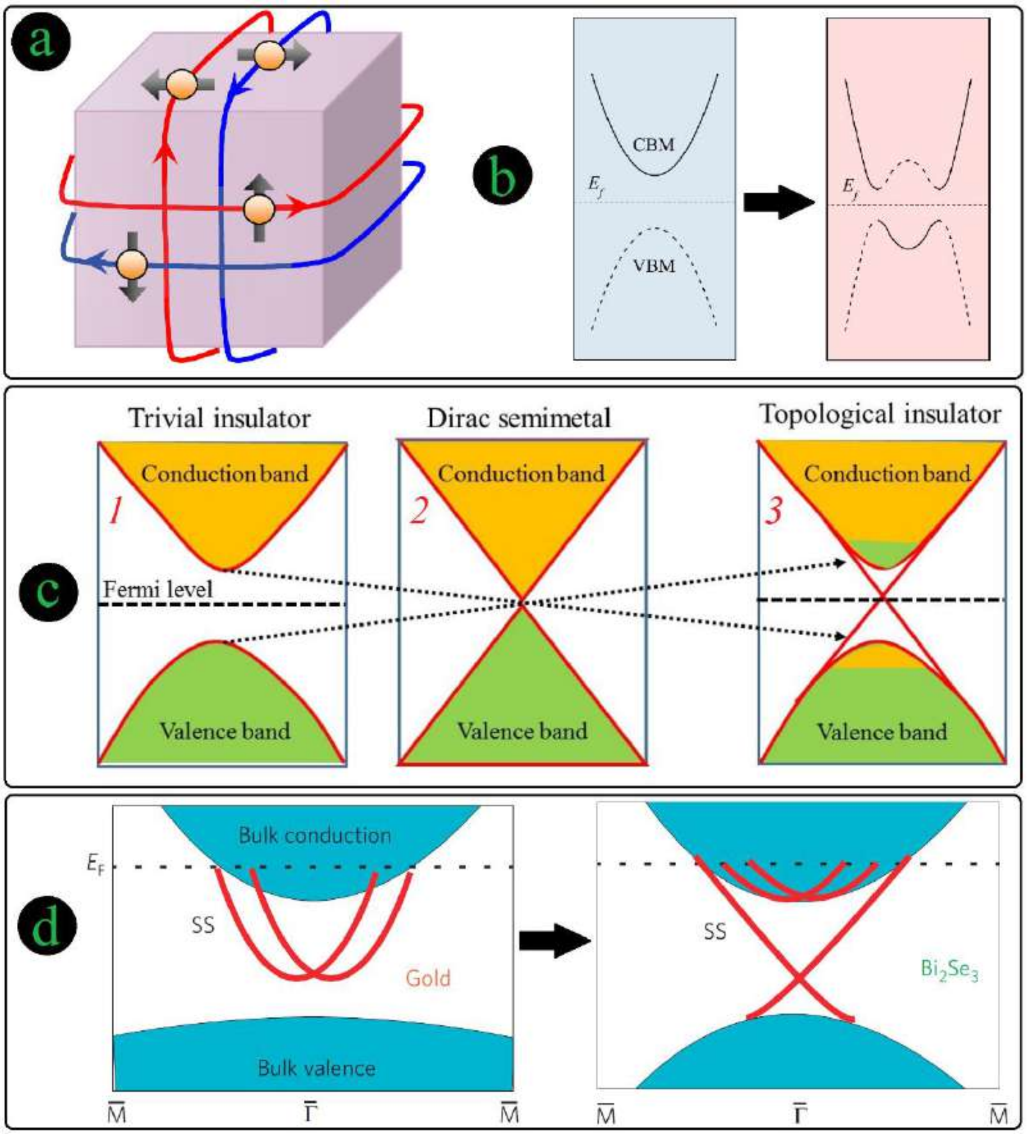


**Fig. 1.1 a**) Schematic representation of surface states in three-dimensional TIs: red and blue bands represent surface currents with oppositely directed spins [5]. **b**) Transition from a trivial insulator (left) to band inversion under strong spin-orbit coupling (right) [4]. **c**) Evolution scheme of the energy spectrum with increasing spin-orbit interaction leading to band inversion: from trivial insulator phase (1) through gapless phase ("critical point") (2) to inverted spectrum in TI phase (3) [6]. **d**) Surface states for a conventional conductor (left, for Au) and for a TI (right, for $Bi_2Se_3$) [5].

In Dirac semimetals, the conduction and valence bands touch only at discrete Dirac points. These materials exhibit linear dispersion along three momentum directions, forming Dirac cones (Fig. 1.2a) [2].

These materials are characterized by strong spin-orbit coupling, similar to TIs. The intersection of valence and conduction bands is protected at the Dirac point by spatial group symmetry. In the presence of both time-reversal and inversion symmetries, linear dispersion of the energy spectrum is observed. Surface states in Dirac semimetals differ from those in topological insulators [2].

In Dirac semimetals, surface states form an arc-like contour connecting the projections of Dirac nodes in the Brillouin zone on the $k_z$=0 plane.

The topological features of Weyl semimetals' band structure arise from breaking either inversion symmetry (*P*-symmetry) or *T*-symmetry. When one of these symmetries is broken, a pair of Weyl points forms in the Brillouin zone (Fig. 1.2b). It is proposed that breaking time-reversal symmetry, for example through external magnetic fields or magnetic element doping, can lead to the formation of various types of Weyl semimetals [2].

Weyl points are discrete nodes where conduction and valence bands touch, forming linear dispersion. Unlike Dirac semimetals, Weyl points possess definite chirality (a numerical topological index) that determines their kinematic properties. An important consequence of Weyl points is the presence of arc surface states (Fermi arcs) connecting the projections of Weyl points on the Brillouin zone surface (Fig. 1.2c) [27].

There are two types of Weyl semimetals. In Type I, the Fermi surface contracts to zero at Weyl points, while in Type II, electron and hole bands have contact points and form tilted Weyl cones with finite density of states at the nodes [26] (Fig. 1.2d). Additionally, Lorentz invariance in Type II Weyl semimetals is broken due to tilted Weyl cones. Weyl point pairs in Weyl semimetals can be considered as Dirac points separated by breaking either *P*-symmetry or *T*-symmetry [2, 3].

Like TIs, Weyl semimetals can exhibit unique electronic properties and effects, such as anomalous Zeeman effect, anomalous Hall effect, and colossal magnetoresistance. These properties make Weyl semimetals promising and potentially useful for various technological applications, including electronics, spintronics, and quantum information technologies [23].

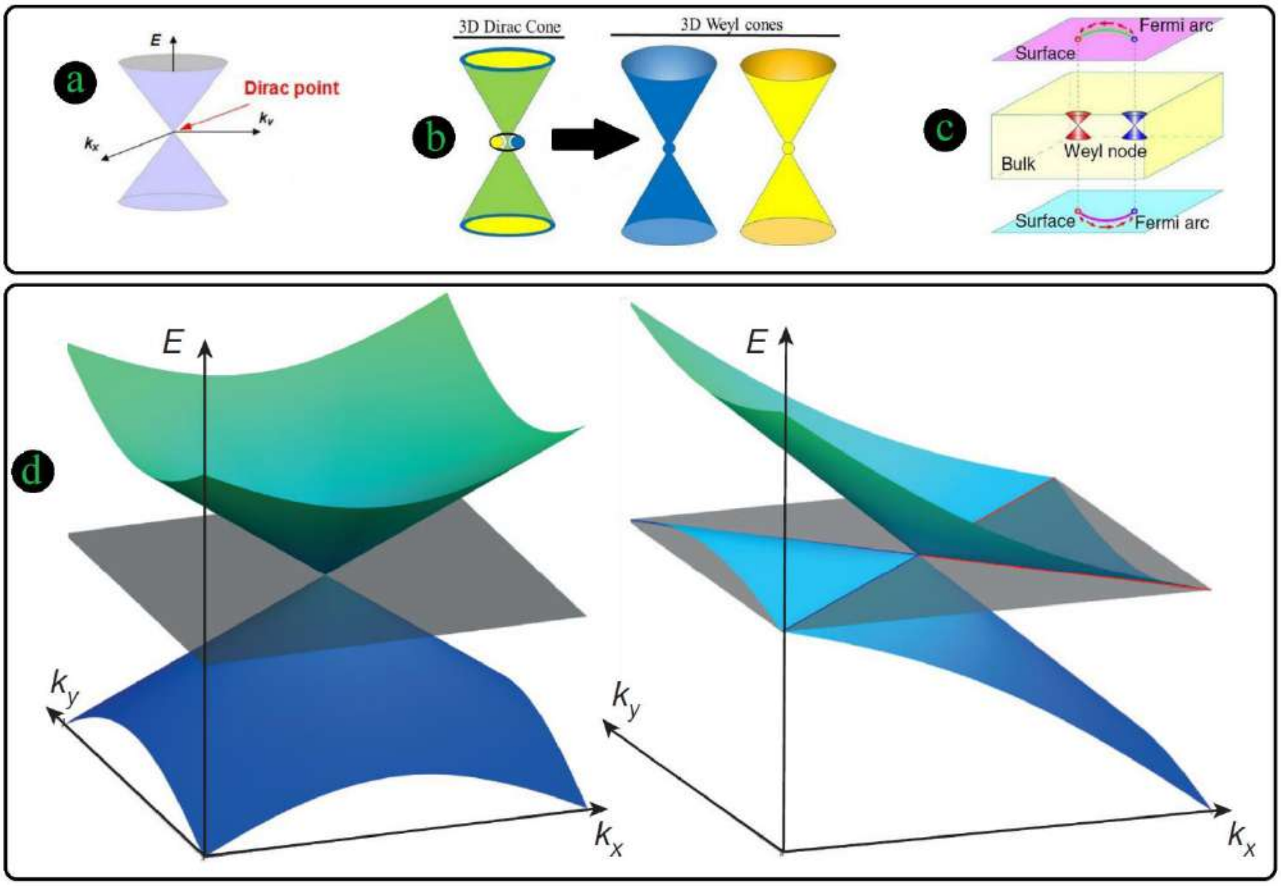


**Fig. 1.2 a**) Linear dispersion in the bulk of a topological semimetal with a Dirac point [2]. **b**) Formation of a pair of Weyl points [3]. **c**) Fermi arcs connecting the projections of Weyl points on the Brillouin zone surface [27]. **d**) Type-I (left) and Type-II (right) Weyl cones [26].

## 1.2 Review of Magnetic Properties in Doped $Bi_2Se_3$ and $Bi_2Te_3$ Topological Insulators

Studies of doped topological insulators (TIs) have revealed diverse magnetic ordering phenomena, including ferromagnetic and antiferromagnetic correlations, and spin glass properties. However, these experiments have also shown significant contradictions in their results.

Specifically, in Mn-doped $Bi_{1.97}Mn_{0.03}Se_3$ crystal, a spin glass state was observed [63] (Fig. 1.3a), while crystals of similar composition exhibited paramagnetic behavior with low-temperature antiferromagnetic correlations [64] (Fig. 1.4b). At higher manganese concentrations ($x \geq 0.05$), ferromagnetic correlations were detected (Fig. 1.3b). It was also noted that increasing manganese content led to higher Curie-Weiss temperatures in $Bi_{1.97}Mn_{0.03}Se_3$ [64] and $Bi_{2-x}Mn_xTe_3$ with x=0.04 and 0.09 [65] (Fig. 1.3c). Similar trends were observed in nickel-doped $Bi_2Te_3$ and $Bi_2Se_3$ crystals [66].

Two sequential phase transitions to spin glass and ferromagnetic phases were discovered in cobalt-doped $Bi_2Se_3$ crystal [67] (Fig. 1.3d). Meanwhile, studies of iron-doped $Bi_2Se_3$ crystals demonstrated ferromagnetic ordering [68, 69, 70], which apparently was not related to inclusions of other phases [70].

Magnetic properties of chromium-doped $Bi_2Se_3$ crystals were investigated in studies [69-73]. Negative paramagnetic temperature was observed in bulk $Bi_{1.85}Cr_{0.15}Se_3$ crystal, which showed antiferromagnetic correlations [69] (Fig. 1.3e). Paramagnetic behavior was reported in [73] for bulk $Bi_{2-x}Cr_xSe_3$ crystals with $x \leq 0.02$, while the temperature dependence of susceptibility in crystal with x=0.04 was characteristic of antiferromagnets (Fig. 1.3f).

In contrast, MBE-grown $Bi_{2-x}Cr_xSe_3$ films demonstrated ferromagnetic ordering with composition-dependent critical temperatures of 35 K for x=0.1 and 20 K for x=0.03 [69, 71, 73]. Study [74] showed that depositing a thin cobalt film on top of Cr: $Bi_2Se_3$ film increases the critical temperature from 7 K to 19 K in the near-surface layer, while in the bulk it only rises to 10 K. This indicates a limited proximity effect range in doped TIs and may be valuable for developing new physical models.

The nature of magnetic ordering in doped TIs remains a subject of active discussion. According to theoretical calculations [19, 75], substitution of Bi or Sb atoms with 3*d* elements in $Sb_2Te_3$, $Bi_2Se_3$, or $Bi_2Te_3$ lattices should result in high-spin states of impurity ions. However, experimentally observed magnetic moments of manganese [64, 65], iron [68, 70, 76], and chromium [69, 72] ions in $Bi_2Se_3$ are significantly lower than expected for high-spin state values. This could be explained by partial formation of transition metal chalcogenides as clusters [68] or impurity segregation between TI layers [66, 71].

Simultaneously, the observed magnetization anisotropy [65, 67] indicates that some impurity ions substitute Bi or Sb ions in the TI lattice. It was suggested [69, 73] that doping-induced charge carriers play a crucial role in ferromagnetic ordering formation through RKKY exchange interaction between local magnetic moments of transition metal ions. However, several studies showed that charge carrier concentration does not significantly affect magnetic properties of doped $Bi_2Se_3$ [68], $Bi_2Te_3$ [65], and $Sb_2Te_3$ [77]. Doping of $Bi_{0.97-x}Sb_{0.03}$ topological insulators with magnetic Ni and Fe ions was found to affect magnetoresistance [78].

The question of magnetic ordering's influence on TI topological surface states remains open. Some studies reported the opening of a gap in the surface state spectrum of doped TIs, observed by photoemission spectroscopy [65, 69]. However, the extent of magnetization localization in the near-surface layer is not fully understood. Polarized neutron reflectometry studies showed that magnetization is distributed throughout the entire Cr: $Bi_2Se_3$ film volume [71]. Meanwhile, work [74] demonstrated that the Co film proximity effect leads to a stronger increase in critical temperature in the near-surface layer compared to the bulk.

### 1.3 Review of Magnetic Properties in Doped Bulk Weyl Semimetal $WTe_2$

Topological semimetals, particularly doped Weyl semimetals (WSMs), attract significant interest due to their unique properties and potential applications in quantum technologies. Studies [79, 80] demonstrated that doping with S and Ir ions substantially

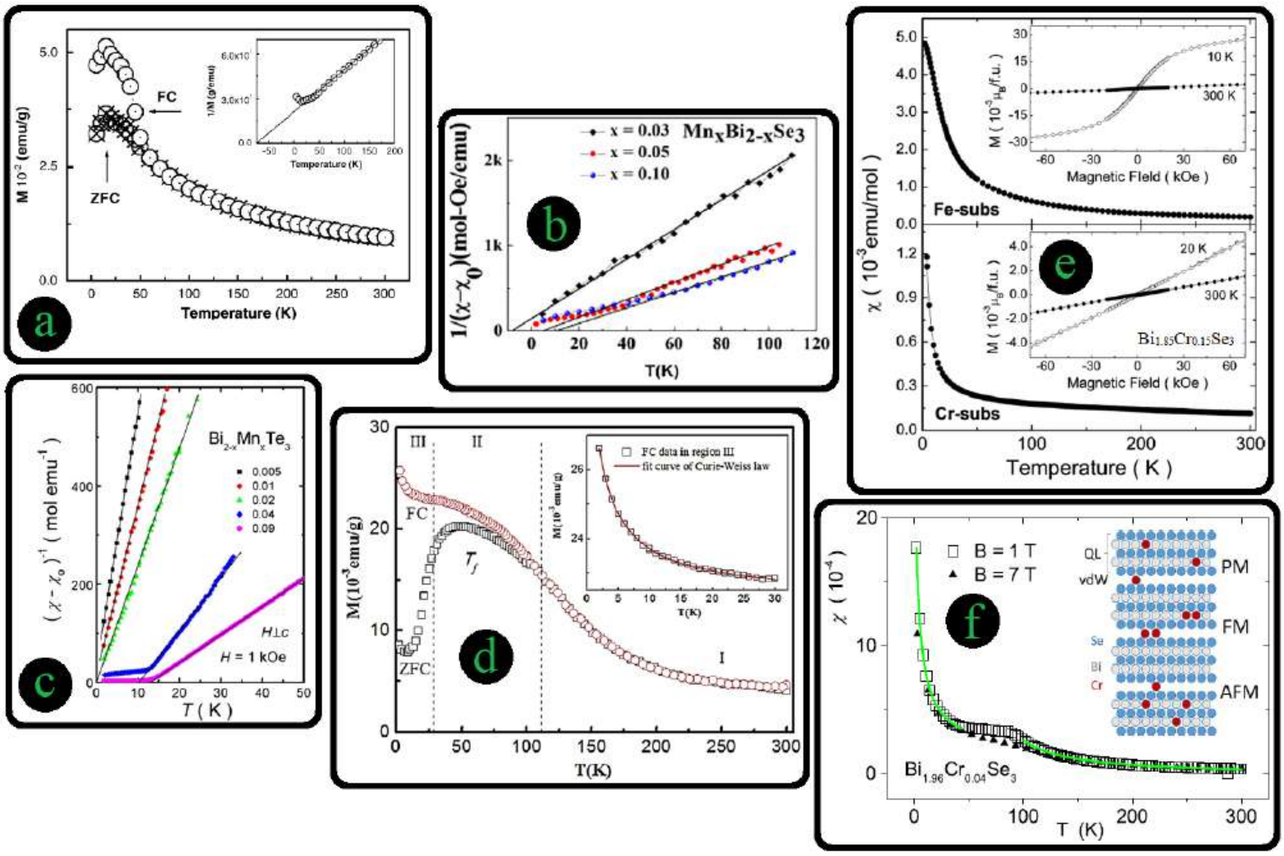


**Fig. 1.3 a**) ZFC-FC magnetization curves of TI $Bi_{2-x}Mn_xTe_3$ measured in a magnetic field of 1 kOe [63]. **b**) Inverse magnetic susceptibility of bulk TI $Bi_{2-x}Mn_xSe_3$ [64]. **c**) Inverse magnetic susceptibility of TI $Bi_{2-x}Mn_xTe_3$ film [65]. **d**) ZFC-FC temperature-dependent magnetization curves for $Co_{0.08}Bi_{1.92}Se_3$ [67]. The inset shows the Curie-Weiss law fitting of the low-temperature region of the FC magnetization curve. **e**) Temperature dependencies of magnetic susceptibility for iron- and chromium-doped $Bi_2Se_3$ crystals, measured in fields of 20 kOe and 30 kOe, respectively [69]. The insets show field dependencies measured at 10 K and 300 K for chromium-doped, and at 20 K and 300 K for iron-doped $Bi_2Se_3$ crystals. **f**) Magnetic susceptibility of bulk TI $Bi_{1.96}Cr_{0.04}Se_3$. The inset shows possible locations of Cr ions in the $Bi_2Se_3$ matrix [73].

enhances superconductivity in $MoTe_2$ single crystals. The maximum phase transition temperature for $MoTe_{1.8}S_{0.2}$ reached approximately 1.3 K, which is 13 times higher than in pristine $MoTe_2$. This result was confirmed by both resistance and magnetic susceptibility measurements.

Another study [81] showed that magnetic ion doping can induce a topological phase transition from a Dirac semimetal to a Weyl semimetal. Experimental confirmation of this effect was obtained for Mn-doped $VAl_3$ semimetal [82]. In this case, Weyl phases coexisted with the Kondo effect arising from electron interactions with magnetic impurities.

It was also demonstrated that Ni doping reduces the resistance growth with increasing magnetic field in $WTe_2$ [83], which is consistent with the general disorder effect on magnetoresistance [84]. However, *p*-type doping with fluoroplastics in $WTe_2$ led to increased magnetoresistance, likely due to better carrier compensation [85].

Other studies revealed that potassium intercalation in $WTe_2$ induces superconductivity below 2.6 K [86]. The influence of Fe doping on $WTe_2$ transport properties was investigated in works [87, 88]. Fe substitution for Te induced a metal-insulator phase transition and changes in electron transport.

Notably, magnetic ordering was recently discovered only in chromium-doped $WTe_2$ (Fig. 1.4) [89]. The study published in [89] demonstrated that introducing chromium into the $WTe_2$ matrix leads to stable ferromagnetism with tunable properties. The Curie temperature $T_c$ and magnetic moment can be controlled by varying chromium concentration. The maximum $T_c$ value for Cr-doped $WTe_2$ can reach 283 K, close to room temperature. Magnetization can vary from 2.26 to 4.20 emu/g, significantly exceeding most values reported for similar materials. Although chromium-doped $WTe_2$ maintains its semimetallic properties, these results indicate the possibility of controlling the topological phase in $WTe_2$ using an external magnetic field.

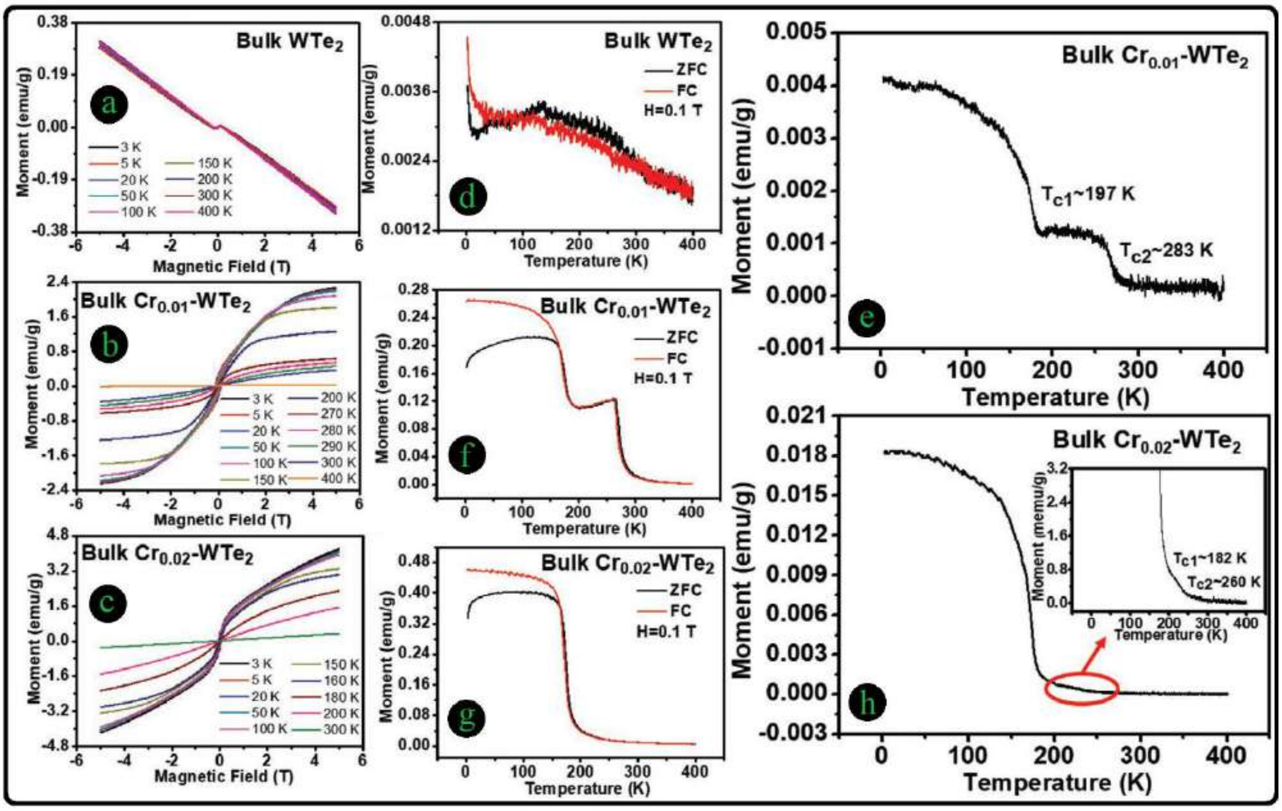


**Fig. 1.4** Magnetic properties of pristine and chromium-doped *Td*-WTe2 single crystals. Magnetization isotherms for **a**) pristine $WTe_2$, **b**) $Cr_{0.01}$-$WTe_2$, and **c**) $Cr_{0.02}$-$WTe_2$ measured in the temperature range from 3 to 400 K and magnetic fields up to ±50 kOe. Temperature dependencies of ZFC and FC magnetization for **d**) pristine WTe2, **f**) $Cr_{0.01}$-$WTe_2$, and **g**) $Cr_{0.02}$-$WTe_2$ in the temperature range from 3 to 400 K under an applied magnetic field of 1 kOe. Spontaneous magnetization curves ($H$ = 0 kOe) for **e**) $Cr_{0.01}$-$WTe_2$ and **h**) $Cr_{0.02}$-$WTe_2$ samples in the temperature range from 3 to 400 K measured in zero-field mode (without external magnetic field) [89].

## 1.4 Chapter 1 Conclusions

After analyzing two unique classes of materials - topological insulators and Weyl semimetals, with emphasis on their magnetic properties, it can be noted that these materials are distinguished by their unique electronic characteristics, which present a vast field for technological research and applications. The key point is that the magnetic properties of these materials can significantly vary depending on doping and growth quality. It has been discovered that these factors can cause substantial changes in magnetic ordering, which in turn can lead to various effects on the electronic structure and behavior of these materials in magnetic fields.

# Chapter 2. Experimental Equipment and Samples

This chapter describes the sample synthesis methods and experimental techniques used in the research. The first part is devoted to describing the melt crystallization using the Bridgman-Stockbarger method and the chemical vapor transport method. The second part provides a brief description of the MPMS SQUID magnetometer and PPMS calorimeter with EverCool-II attachment. The third part focuses on describing the crystal structure of the samples, testing using X-ray diffraction analysis and energy-dispersive X-ray spectroscopy (EDS), as well as the setup of experiments on the MPMS SQUID magnetometer and PPMS calorimeter.

## 2.1 SQUID Magnetometry and Relaxation Microcalorimetry

### 2.1.1 SQUID MPMS 3

SQUID MPMS 3 (Magnetic Property Measurement System) is an advanced magnetic property measurement system developed by Quantum Design. This vibrating sample magnetometer uses a Superconducting Quantum Interference Device (SQUID) as a detector for highly sensitive measurements of magnetic characteristics in various materials. SQUID is a device that converts magnetic flux into direct or alternating current electrical signals [90]. This operation is based on the phenomenon of magnetic flux quantization in a superconducting ring with integrated Josephson junctions. The ring made of superconducting material containing one or two Josephson junctions serves as the sensitive component of the SQUID. The current flowing in the ring depends on the magnetic flux passing through the closed loop. When the internal magnetization of the measured sample changes, the current in the ring changes accordingly, and this variation is detected.

The SQUID magnetometer at the Research Center "Diagnostics of Functional Materials for Medicine, Pharmacology and Nanoelectronics" operates in a temperature range of 1.8 - 400 K. Working in a closed cycle, the device does not require helium refilling. Depending on the samples being measured, either extraction or vibrating modes can be used for magnetic moment measurements. The SQUID MPMS 3 measurement accuracy reaches $10^{-8}$ emu. The magnetic field strength goes up to ±70 kOe. All measurements in this work were performed in magnetic field stabilization mode. The sample holder design and MPMS SQUID magnetometer calibration methodology are described in [95].

### 2.1.2 PPMS-9 + EverCool-II

PPMS-9 (Physical Property Measurement System) is a versatile and modular physical property measurement system also developed by Quantum Design. The

PPMS-9 + EverCool-II complex at the Research Center "Diagnostics of Functional Materials for Medicine, Pharmacology and Nanoelectronics" is designed to study various material characteristics, including magnetic, electrical, thermal, and mechanical properties, over a wide range of temperatures (1.9 - 1000 K) and in static or alternating magnetic fields (±90 kOe). When working with the "Heat Capacity (HC) Quantum Design" relaxation microcalorimeter option, special cells are used where the sample is fixed using Apiezon N vacuum grease [96]. The relative error in determining heat capacity values on such systems typically does not exceed 5% [97]. EverCool-II is a cryogenic system integrated into PPMS-9 that provides autonomous cooling using only gaseous helium. This device simplifies the operation of the PPMS-9 system. Working in a closed cycle, PPMS-9 + EverCool-II does not require helium refilling.

## 2.2 Samples and Experiment

### 2.2.1 Characteristics of $Bi_{2-x}Fe_xSe_3$ and $Bi_{2-x}Cr_xSe_3$ Single Crystals, Nominal Composition Analysis and Crystal Structure

Single crystals of $Bi_{2-x}Fe_xSe_3$ with x=0.006, 0.03, and 0.06, and $Bi_{2-x}Cr_xSe_3$ with x=0.01, 0.03, and 0.06 were grown in two stages. The first stage involved placing initial components in powder form into quartz ampoules, followed by heating under pressure of $10^{-4}$ atm up to 750 - 800 °C for 5 hours and holding for about 12 hours for $Bi_{2-x}Fe_xSe_3$ single crystals and 30 hours for $Bi_{2-x}Cr_xSe_3$ single crystals. After cooling, the material was ground again and used for single crystal growth by the Bridgman-Stockbarger method [91, 92]. The maximum furnace temperature was 850 °C. The ampoules were moved in the growth region at a rate of 3 mm/h. Symmetry was controlled by powder X-ray diffraction. Samples for investigation were cleaved perpendicular to the [001] axis from the grown boule and had a plate-like shape with thickness about 0.1-0.3 mm with masses for $Bi_{2-x}Fe_xSe_3$: 3.4 mg (x=0.006); 12.4 mg (x=0.03); 5.67 mg (x=0.06) and for $Bi_{2-x}Cr_xSe_3$: 48.08 mg (x=0.01); 7.52 mg (x=0.03); 11.94 mg (x=0.06).

The crystal structure of the samples and single crystallinity were verified using a Bruker D8 DISCOVER powder X-ray diffractometer for $Bi_{2-x}Cr_xSe_3$ single crystals and a DRON-2.0 X-ray diffractometer for $Bi_{2-x}Fe_xSe_3$ single crystals (Fig. 2.1a). $Bi_{2-x}Fe_xSe_3$ and $Bi_{2-x}Cr_xSe_3$ single crystals have rhombohedral symmetry with space group $R\bar{3}m$ [98], similar to undoped $Bi_2Se_3$ single crystals (Fig. 2.1b). The quintuple atomic layers Se1-Bi-Se2-Bi-Se1 are highlighted by a square, where Se1 and Se2 are two crystallographically inequivalent positions of selenium ions (upper part of Fig. 2.1b). Two layers (Bi-Se2) with Cr or Fe ion substituting Bi (lower part of Fig. 2.1b). The nominal composition was close to the composition obtained on a Zeiss Merlin SEM equipped with an Oxford Instruments INCA x-act EDS spectrometer (Fig. 2.1c). Mapping confirms sufficiently good homogeneity of impurities in the bismuth selenide crystal matrix. Chemical composition analysis of the single crystals demonstrated clear correspondence to stoichiometric $Bi_2Se_3$, $Bi_{2-x}Fe_xSe_3$, and $Bi_{2-x}Cr_xSe_3$. Elemental mapping of magnetic impurities for $Bi_{1.994}Fe_{0.006}Se_3$ and $Bi_{1.99}Cr_{0.01}Se_3$ samples was unfeasible due to spectrometer limitations related to its sensitivity to low concentrations of magnetic impurities.

### 2.2.2 Characteristics of $Fe_xW_{1-x}Te_2$ Single Crystals, Nominal Composition Analysis and Crystal Structure

Single crystals of tungsten ditelluride $WTe_2$ and iron-doped $Fe_{0.03}W_{0.97}Te_2$ were grown by chemical vapor transport method using iodine as a transport agent [93]. The crystal growth process was conducted in an evacuated quartz glass ampoule for three weeks [94]. Plates for magnetic measurements were cut from the grown ingots perpendicular to the crystallographic **c**-axis. One plate of iron-doped tungsten ditelluride was annealed at $T$ = 1183 K for two hours followed by water quenching before measurements, while another plate was studied as-grown. The weights of the unannealed $Fe_{0.03}W_{0.97}Te_2$, annealed $Fe_{0.03}W_{0.97}Te_2$, and undoped $WTe_2$ samples were 3.96, 6.32, and 23.53 mg, respectively. The undoped $WTe_2$ was not subjected to annealing.

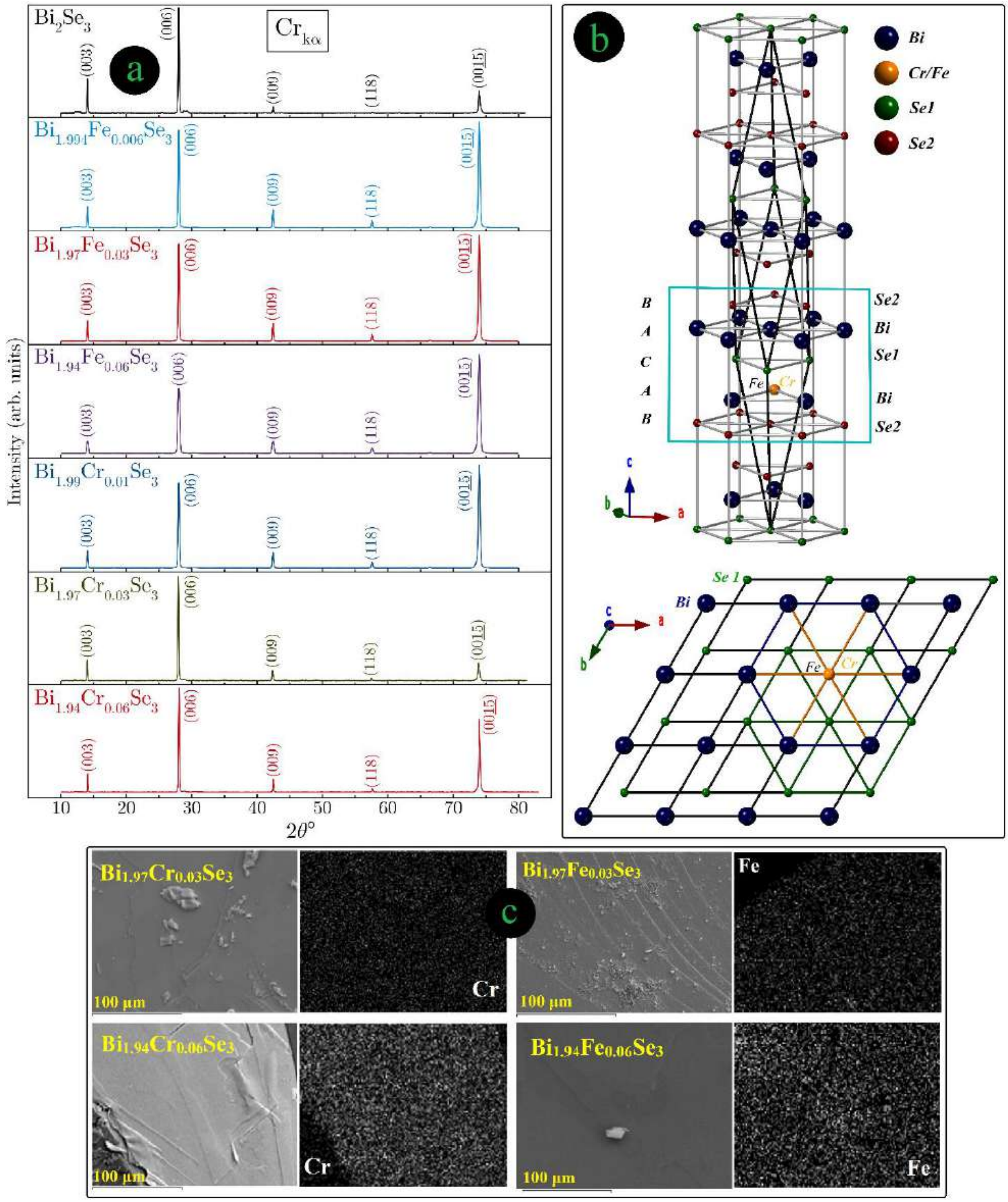


**Fig. 2.1** (**a**) Fragments of diffraction patterns taken from the surface of $Bi_2Se_3$, $Bi_{2-x}Fe_xSe_3$, and $Bi_{2-x}Cr_xSe_3$ single crystals. (**b**) Hexagonal unit cell of $Bi_2Se_3$ with chromium or iron impurity ion. (**c**) Elemental surface mapping of $Bi_{2-x}Fe_xSe_3$ and $Bi_{2-x}Cr_xSe_3$ performed for doped samples.

X-ray diffraction performed at room temperature confirmed that both doped and undoped samples belong to *Td* symmetry and are single crystals. The layered $WTe_2$ crystal has an orthorhombic, non-centrosymmetric *Td* lattice structure (space group *Pmn21*) [99]. The $WTe_2$ structure remains stable with temperature changes [100, 101]. The diffraction patterns for unannealed and annealed $Fe_{0.03}W_{0.97}Te_2$ samples are identical (Fig. 2.2a). Minor differences in X-ray peaks between doped and undoped samples may be caused by some disorder induced by doping.

The *Td* lattice consists of triple layers of Te-W-Te atoms connected by weak van der Waals interactions, while intralayer bonds are covalent. The triple layers are stacked along the **c**-axis. The unit cell consists of four formula units. Iron ions substitute for tungsten (Fig. 2.2b).

The nominal composition was close to the composition obtained using a Tescan Mira SEM equipped with an Oxford Instruments INCA x-act EDS spectrometer and electron backscatter diffraction. Elemental mapping obtained for annealed and unannealed $Fe_{0.03}W_{0.97}Te_2$ samples confirmed that Fe doping was uniform without formation of iron clusters (Fig. 2.2c). This suggests that the magnetic properties reported in this work are not due to the presence of secondary phases.

### 2.2.3 Magnetization and Heat Capacity Measurements using MPMS (SQUID-VSM) and PPMS-9 + EverCool-II

The majority of temperature and field-dependent static magnetization measurements were performed using a Quantum Design MPMS (SQUID-VSM) vibrating magnetometer in the temperature range from 1.8 to 400 K and in magnetic fields up to ±70 kOe. Temperature dependences of magnetization were measured in heating mode under various fields after zero-field cooling (ZFC) and in field cooling (FC) mode. The sample was oriented in the magnetic field such that the crystallographic **c**-axis was either parallel (**c** ∥ **H**) or perpendicular (**c** ⊥ **H**) to the magnetic field. The specific magnetic susceptibility $\chi$ was calculated as $\chi = M / H$, where $M$ is the specific magnetization of the sample, and $H$ is the magnetic field strength [102].

Heat capacity was measured using a Quantum Design Physical Property Measurement System PPMS-9+Ever-Cool-II using the built-in procedure at temperatures from 1.9 to 300 K in fields from 0 to 1 kOe. The magnetic field was applied along the **c**-axis.

The Levenberg-Marquardt algorithm was chosen as the optimization method for fitting magnetic susceptibility and heat capacity curves.

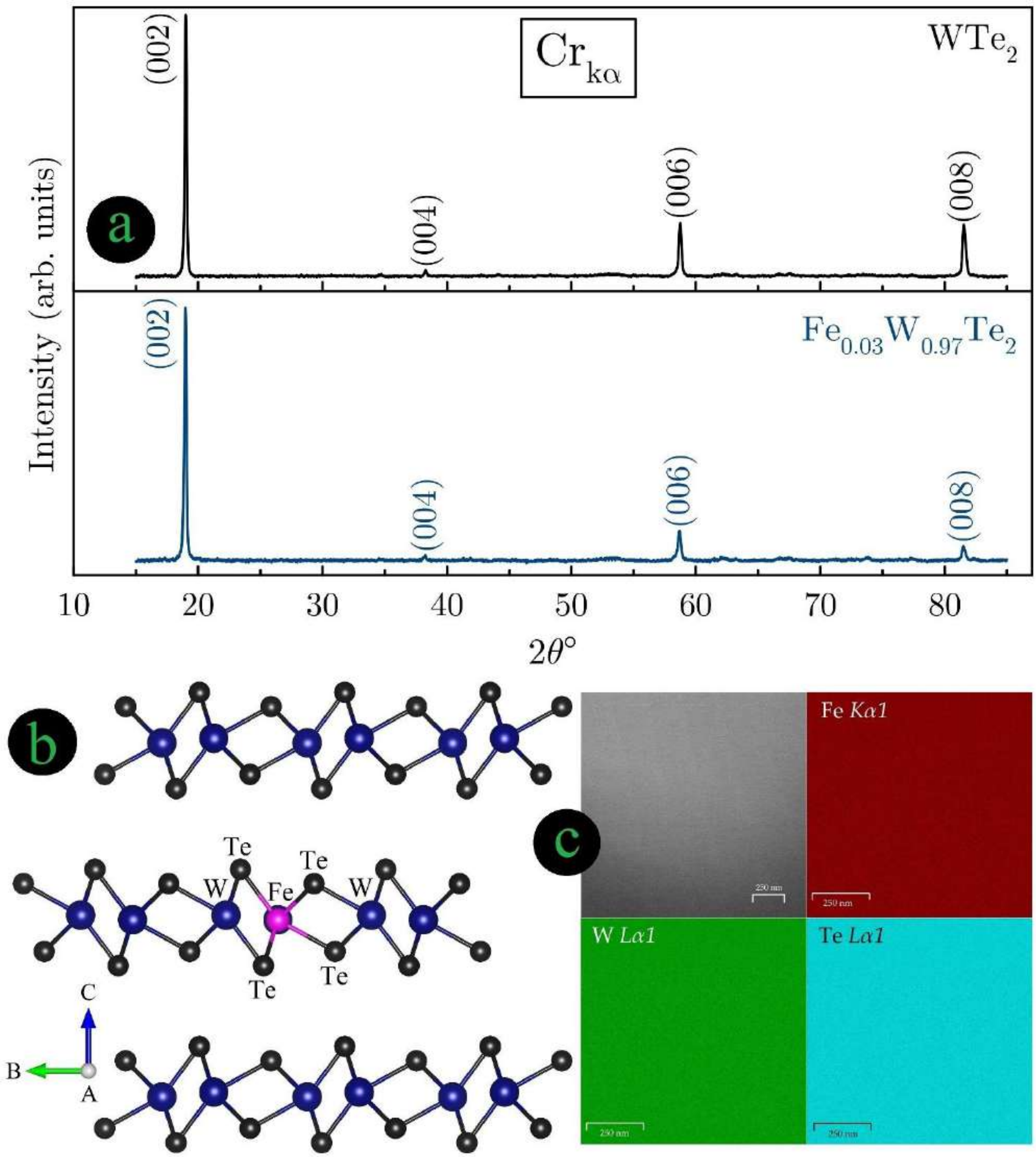


**Fig. 2.2** (**a**) Fragments of diffraction patterns taken from the surface of $WTe_2$ and unannealed $Fe_{0.03}W_{0.97}Te_2$ single crystals. (**b**) Crystal lattice of $WTe_2$. An example of iron substitution for tungsten is shown. (**c**) Elemental surface mapping of unannealed $Fe_{0.03}W_{0.97}Te_2$.

# Chapter 3. Magnetic Studies of Iron-Doped Topological Insulator $Bi_2Se_3$

This chapter presents the results of investigations of *dc* magnetic susceptibility and magnetization isotherms of $Bi_{2-x}Fe_xSe_3$ single crystals with x=0.006, 0.03, and 0.06 in the temperature range from 1.8 K to 400 K under applied magnetic fields up to 70 kOe for two sample orientations in the field. Two magnetic phase transitions were identified, and significant anisotropy of magnetic properties was observed. For samples in the paramagnetic state, effective and absolute magnetic moments per iron atom were calculated, along with temperature-independent contributions to magnetic susceptibility and Curie-Weiss temperatures [103].

## 3.1 Magnetic Susceptibility and Magnetization Isotherms of Undoped Topological Insulator $Bi_2Se_3$

Fig. 3.1 shows the temperature dependences of ZFC and FC dc magnetic susceptibility $\chi$ of $Bi_2Se_3$ powder, obtained under an applied magnetic field of 1 kOe. The magnetic susceptibility of $Bi_2Se_3$ is negative and exhibits a very weak temperature dependence. This is consistent with the expected behavior for diamagnetic materials, whose magnetic susceptibility is typically temperature-independent. Characteristic diamagnetic isotherms measured at 50 K are also presented in Fig. 3.1. The linear dependence of magnetization isotherms confirms the diamagnetic behavior of $Bi_2Se_3$. The diamagnetic contribution of $Bi_2Se_3$ is not only due to the diamagnetism of ionic cores (Langevin diamagnetism). The relatively low effective electron mass $m_e = 0.16m_0$ [104] and the free electron density characteristic of narrow-gap semiconductors $n_e = 1.8 \cdot 10^{19}$ cm$^{-3}$ (at $T$ = 300 K) [105] create conditions for Landau diamagnetism, which in the case of $Bi_2Se_3$ is comparable in magnitude to Langevin diamagnetism.

## 3.2 Magnetic Susceptibility of Iron-Doped $Bi_2Se_3$ Single Crystals

Fig. 3.2 shows the temperature dependences of *dc* magnetic susceptibility $\chi$ for $Bi_{1.994}Fe_{0.006}Se_3$ and $Bi_{1.97}Fe_{0.03}Se_3$ samples, measured in ZFC and FC modes under an applied magnetic field of 50 Oe. Measurements were performed for two crystallographic axis orientations: $\mathbf{c} \parallel \mathbf{H}$ and $\mathbf{c} \perp \mathbf{H}$. The bends in the curves indicate the presence of two magnetic phase transitions in the samples. The first phase transition occurs below 335 K for both sample orientations in the magnetic field. It corresponds to a divergence (bifurcation) of ZFC and FC curves in the temperature range of 112−335 K, accompanied by an increase in magnetic susceptibility curves. The second phase transition is observed at temperatures below 112 K. In the transition region, the behavior of the curves changes significantly for both sample orientations in the magnetic field. For the $\mathbf{c} \parallel \mathbf{H}$ orientation at temperatures below 112 K, a significant increase in the FC susceptibility curves of the samples is observed.

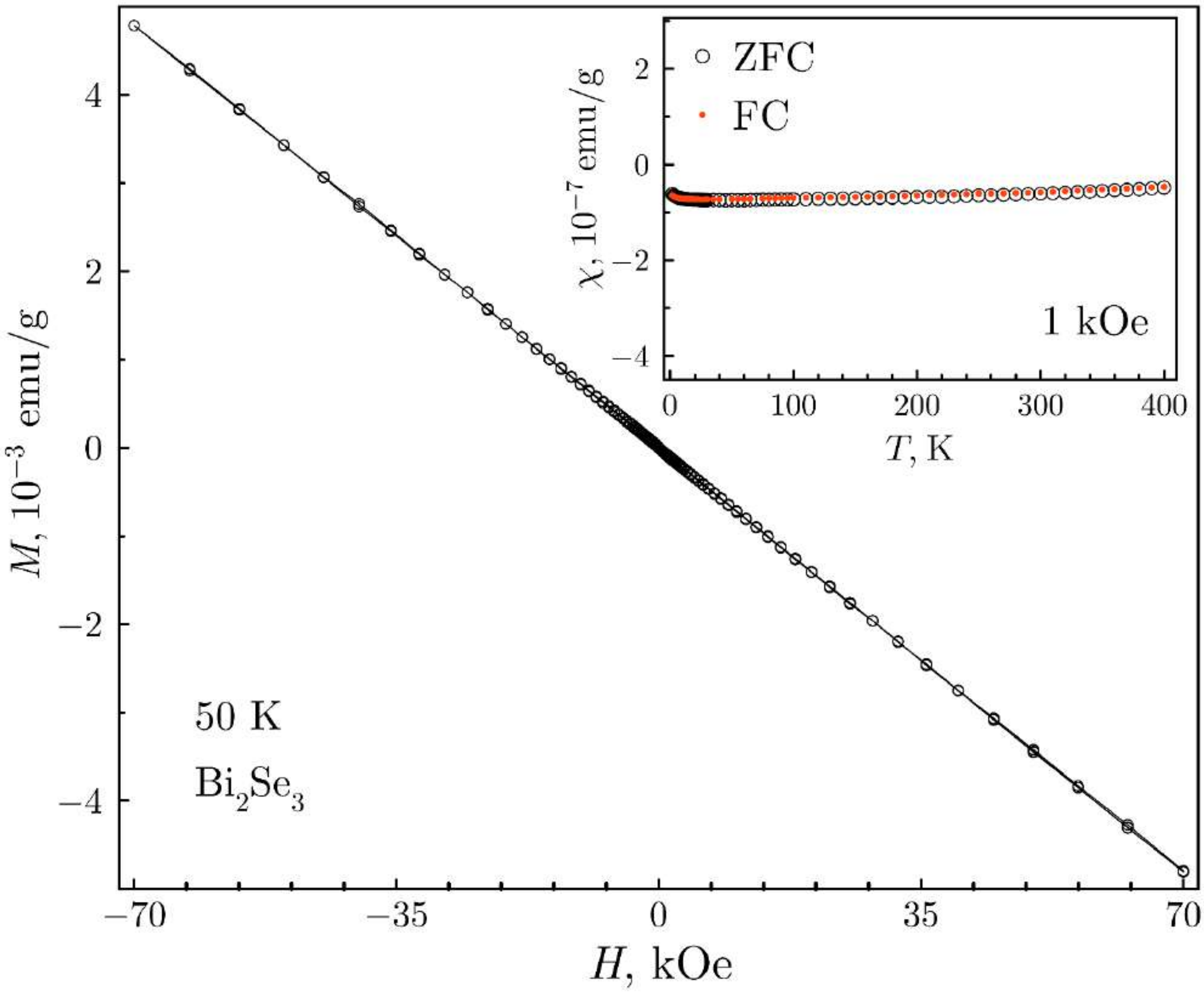


**Fig. 3.1** Magnetic susceptibility and magnetization isotherms of powdered $Bi_2Se_3$.

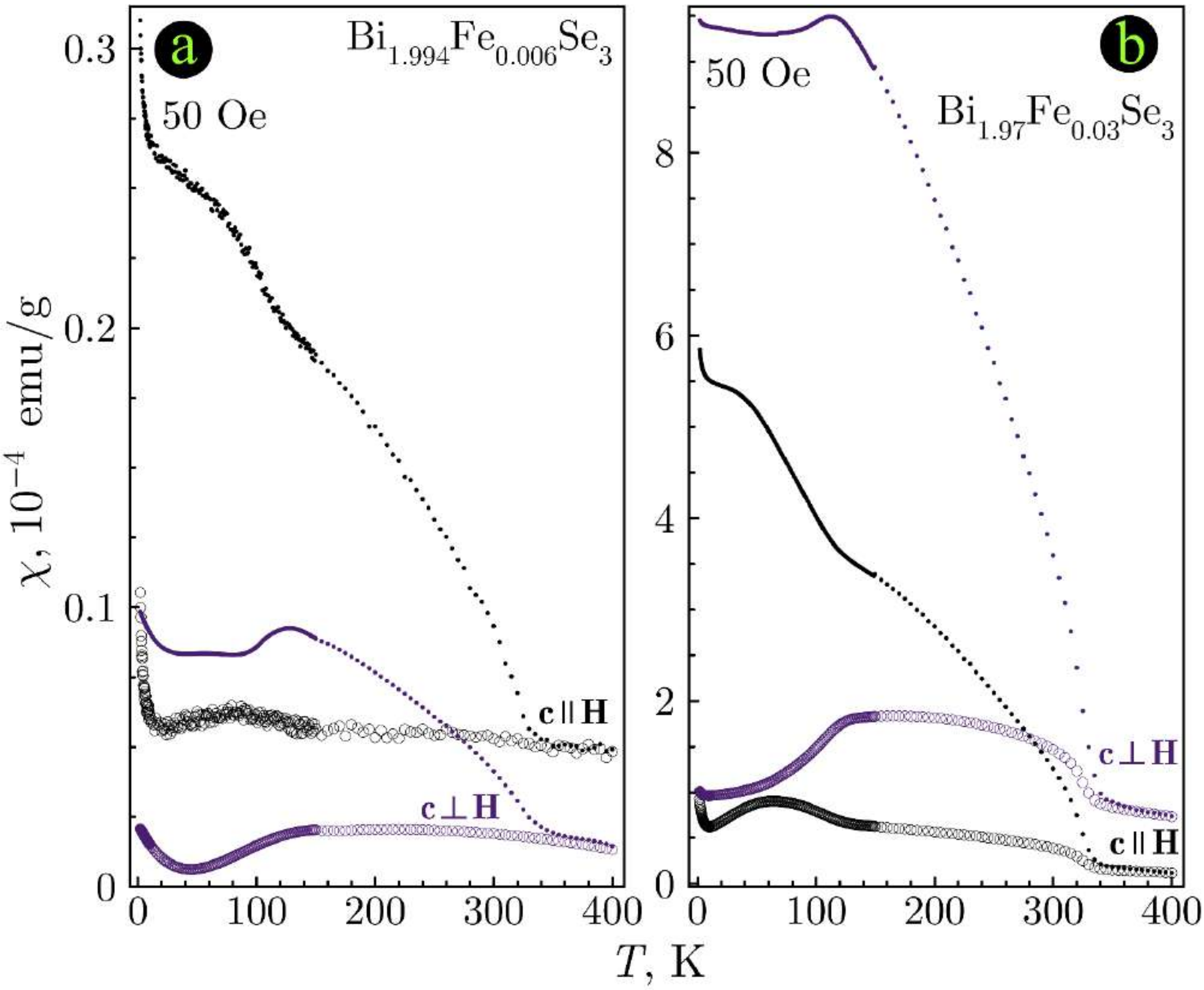


**Fig. 3.2** Temperature dependences of *dc* magnetic susceptibility $\chi$ for $Bi_{1.994}Fe_{0.006}Se_3$ and $Bi_{1.97}Fe_{0.03}Se_3$ samples, obtained in a magnetic field of 50 Oe. Sample orientations are indicated on the graphs. Open symbols – ZFC. Filled symbols – FC.

Meanwhile, the behavior of ZFC curves becomes more complex: the curves show magnetic susceptibility maxima at 80 K for the $Bi_{1.994}Fe_{0.006}Se_3$ sample and at 65 K for the $Bi_{1.97}Fe_{0.03}Se_3$ sample.

For the **c** ⊥ **H** orientation, the ZFC susceptibilities of the samples decrease at temperatures below 112 K. The FC curves also show maxima in the region of the second phase transition, below which the susceptibilities decrease with decreasing temperature and the curves reach a plateau. With further temperature decrease, the magnetic susceptibility of the samples follows the Curie law $\chi \propto 1/T$, which is due to the paramagnetic contribution of iron impurities not participating in exchange interactions.

When stronger magnetic fields are applied, the behavior of magnetic susceptibility curves changes. Fig. 3.3 shows the measurement results for the $Bi_{1.994}Fe_{0.006}Se_3$ sample under applied magnetic fields of 1 kOe, 10 kOe, and 60 kOe.

Under an applied field of 1 kOe, the divergence between ZFC and FC curves decreases. The temperatures at which the phase transition features are observed remain unchanged, indicating that weak magnetic fields have minimal effect on the critical temperatures of phase transitions. When the magnetic field strength is increased to 10 kOe, a shift in the bifurcation temperatures of ZFC and FC curves towards lower values is observed.

Despite the absence of divergence between ZFC and FC magnetic susceptibility curves for $Bi_{1.994}Fe_{0.006}Se_3$ and $Bi_{1.97}Fe_{0.03}Se_3$ samples, distinct features are noticeable at temperatures below 335 K.

For the $Bi_{1.97}Fe_{0.03}Se_3$ sample, unusual features of magnetic susceptibility for dilute magnetics are observed when strong fields up to 70 kOe are applied. In fields of 50 kOe and 70 kOe, the curves do not follow the Curie-Weiss law, and there is no ZFC-FC curve divergence (Fig. 3.4).

Fig. 3.5 shows magnetic susceptibility measurements of the $Bi_{1.94}Fe_{0.06}Se_3$ sample in fields of 1 kOe, 10 kOe, and 50 kOe for both **c**-axis orientations in the magnetic field. Unlike the $Bi_{1.994}Fe_{0.006}Se_3$ and $Bi_{1.97}Fe_{0.03}Se_3$ samples, the $Bi_{1.94}Fe_{0.06}Se_3$ sample does not show a clearly defined phase transition at 335 K

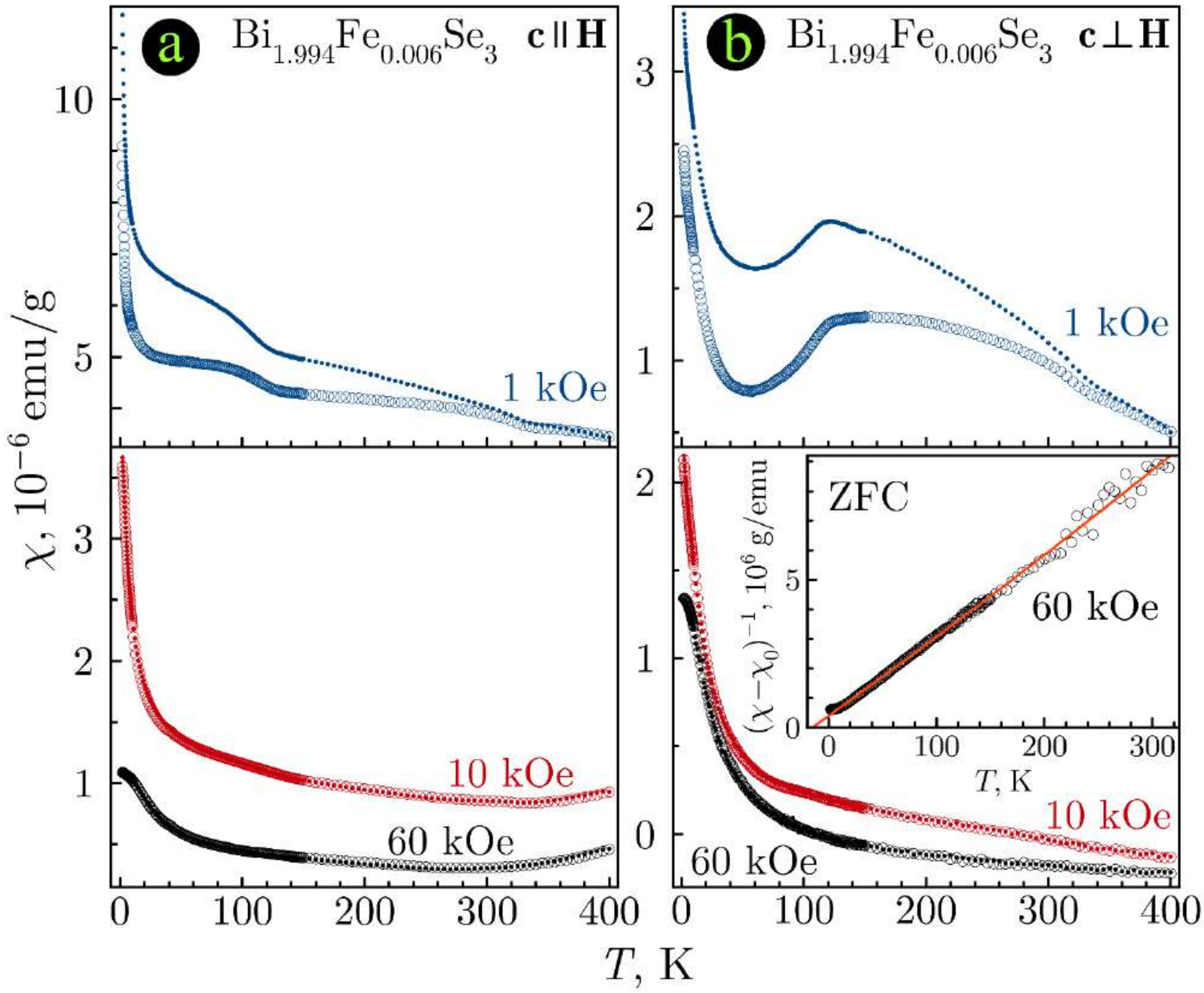


**Fig. 3.3** Temperature dependences of *dc* magnetic susceptibility $\chi$ for the $Bi_{1.994}Fe_{0.006}Se_3$ sample. Sample orientation and magnetic field strength are indicated on the graphs. Open symbols – ZFC. Filled symbols – FC.

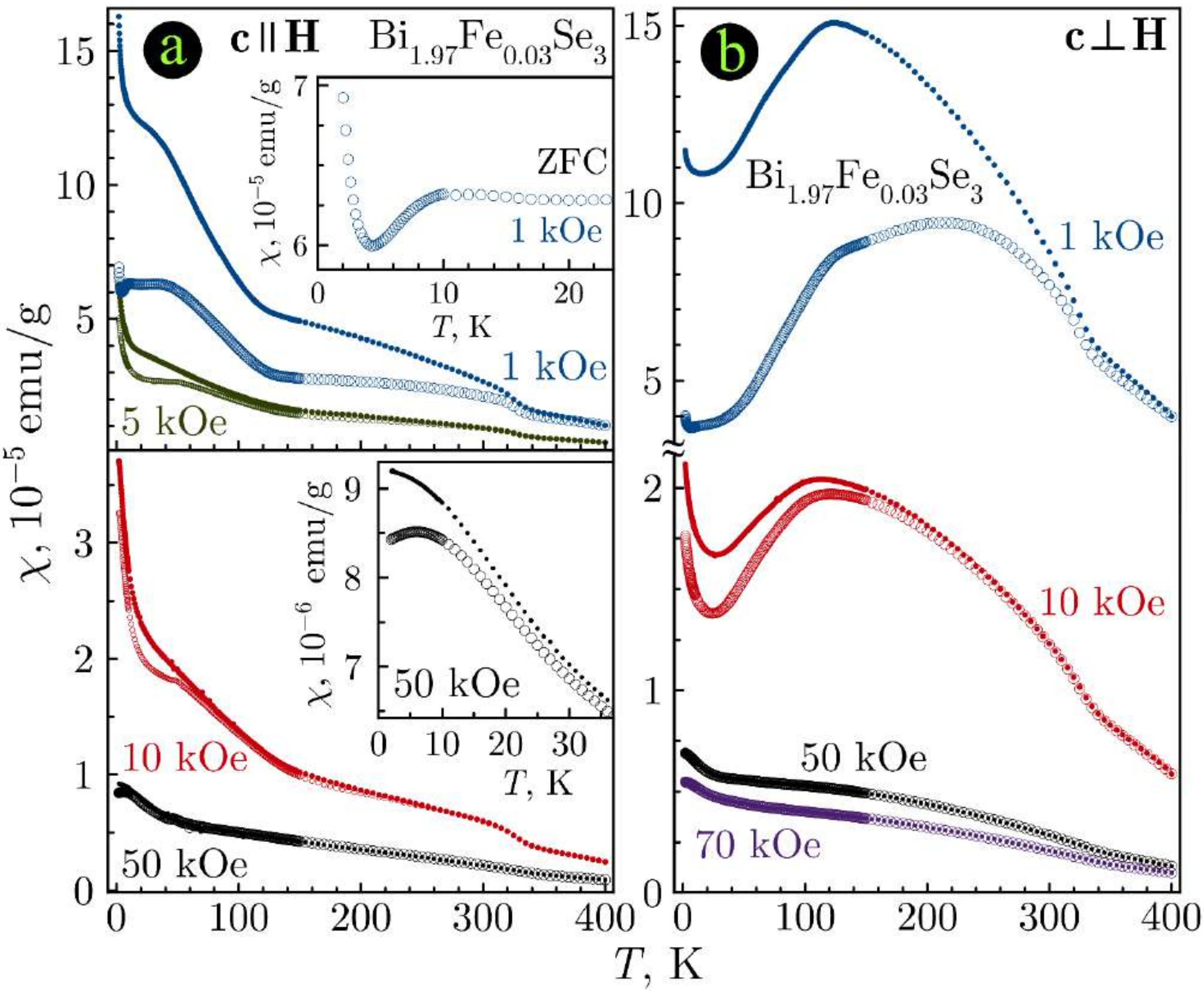


**Fig. 3.4** Temperature dependences of *dc* magnetic susceptibility $\chi$ for the $Bi_{1.97}Fe_{0.03}Se_3$ sample. Sample orientation and magnetic field strength are indicated on the graphs. Open symbols – ZFC. Filled symbols – FC.

in a 1 kOe field. This may indicate differences in the magnetic structure of this sample compared to other compositions. The bifurcation temperature of ZFC and FC curves below 135 K apparently correlates with the second phase transition observed for $Bi_{1.994}Fe_{0.006}Se_3$ and $Bi_{1.97}Fe_{0.03}Se_3$ samples.

According to Figs. 3.2-3.5, analysis of the paramagnetic state in high magnetic fields is only possible for $Bi_{1.994}Fe_{0.006}Se_3$ and $Bi_{1.94}Fe_{0.06}Se_3$ samples. In the temperature range 18−320 K for $Bi_{1.994}Fe_{0.006}Se_3$ and 65−400 K for $Bi_{1.94}Fe_{0.06}Se_3$, in fields of 60 kOe (x=0.006) and 50 kOe (x=0.06), the temperature dependence of magnetic susceptibility for orientations $\mathbf{c} \perp \mathbf{H}$ (x=0.006) and $\mathbf{c} \parallel \mathbf{H}$ (x=0.06) follows the Curie-Weiss law [106]:

$$\chi(T) = \frac{C}{T-\theta} + \chi_0 = \frac{N\mu_{eff}^2}{3k_B(T-\theta)} + \chi_0 \tag{3.1}$$

where $C$ is the Curie constant, $N$ is the concentration of paramagnetic ions, μeff is the effective magnetic moment, $k_B$ is the Boltzmann constant, $T$ is temperature, and $\chi_0$ is the temperature-independent contribution to magnetic susceptibility. The concentration of paramagnetic ions per gram of sample is determined by:

$$N_{ions} = N_A \cdot (x / \mu_{\mathrm{mol}}) \tag{3.2}$$

where $N_A$ is Avogadro's number, $x$ is the concentration of paramagnetic ions in the crystal chemical formula, and M is the molar mass of the studied crystal (Table 3.1).

The insets in Fig. 3.3b and Fig. 3.5a show the inverse ZFC magnetic susceptibility curves $(\chi - \chi_0)^{-1}$. In the TI $Bi_2Se_3$, iron ions substitute trivalent bismuth ions $Bi^{3+}$. However, the obtained values of effective magnetic moments $\mu_{\mathrm{eff}}$ of iron ions may indicate the presence of not only trivalent iron ions $Fe^{3+}$ but also divalent $Fe^{2+}$ ions in the samples [106].

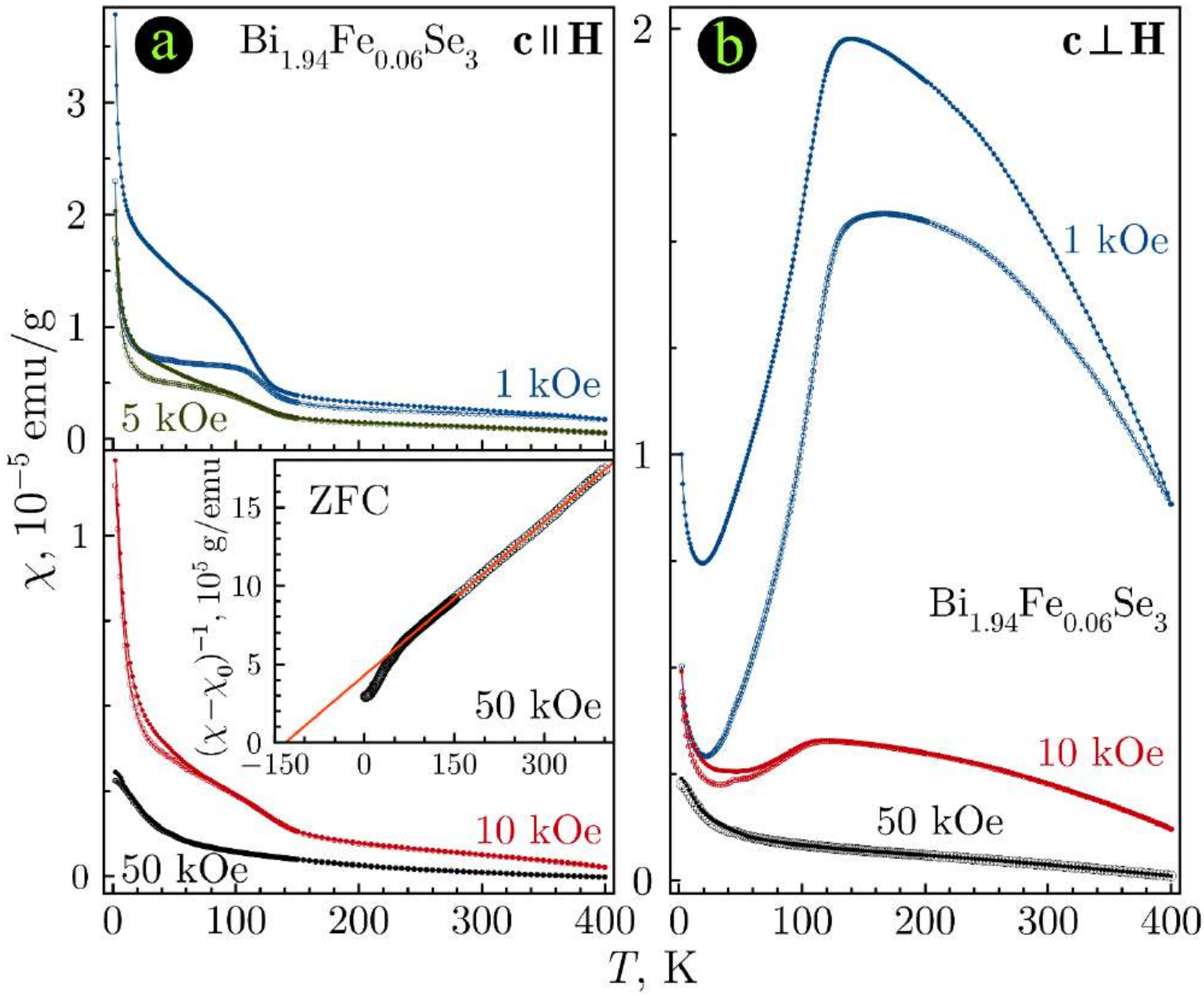


**Fig. 3.5** Temperature dependences of *dc* magnetic susceptibility $\chi$ for the $Bi_{1.94}Fe_{0.06}Se_3$ sample. Sample orientation and magnetic field strength are indicated on the graphs. Open symbols – ZFC. Filled symbols – FC.

Table 3.1. $N$ – number of iron ions per gram of sample, $C$ – Curie constant, $\theta$ – Curie-Weiss temperature, $\chi_0$ – diamagnetic contribution to susceptibility, $\mu_{eff}$ – effective magnetic moment of iron ions.

| Sample / Constants | $Bi_{1.994}Fe_{0.006}Se_3$ | $Bi_{1.94}Fe_{0.06}Se_3$ |
|---|---|---|
| $N$ / g$^{-1}$ | $5.53 \cdot 10^{18}$ | $5.53 \cdot 10^{19}$ |
| $C$ (emu·K / g) | $3.64 \cdot 10^{-5}$ | $3.06 \cdot 10^{-5}$ |
| $\Theta$ / K | –12.7±0.2 | –132 ±1 |
| $\chi_0$ (emu/g) | $-2.94 \cdot 10^{-7}$ | $-6.02 \cdot 10^{-7}$ |
| $\mu_{eff}/\mu_B$ | 5.64±0.02 | 5.14±0.02 |

### 3.3 Magnetization Isotherms and Coercivity of Iron-doped $Bi_2Se_3$ Single Crystals

Magnetization isotherms *M*, measured for both sample orientations in the magnetic field, are shown in Fig. 3.6. Hysteresis loops are visible throughout the temperature range from 2 to 400 K and in the field range of 0±32 kOe. Temperature dependences of the coercivity $H_c$ were determined from the analysis of hysteresis loops and are shown in Fig. 3.7. It can be observed that with decreasing temperature, for both sample orientations in the magnetic field, the coercivity first increases and then anomalously decreases when reaching the low-temperature region (10 – 50 K). The $Bi_{1.94}Fe_{0.06}Se_3$ sample also demonstrates an anomalous minimum of coercivity at 100 K (**c** ‖ **H**).

Fig. 3.8 shows the primary curves of magnetization isotherms in the temperature range from 2 to 400 K and in the field range of 0 – 70 kOe. Complete magnetization saturation is achieved only for $Bi_{1.97}Fe_{0.03}Se_3$ and $Bi_{1.94}Fe_{0.06}Se_3$ samples at 2 K and 10 K and with **c** ‖ **H** orientation, which consequently is the easy magnetization axis. At this orientation, the primary magnetization isotherm curves of $Bi_{1.994}Fe_{0.006}Se_3$ and $Bi_{1.97}Fe_{0.03}Se_3$ samples show anomalous behavior with decreasing temperature: magnetization in the high-field region appears lower than at higher temperatures.

At 2 K and in the saturation field region, there is a significant difference in the magnetic moment per iron ion between the $Bi_{1.994}Fe_{0.006}Se_3$ and $Bi_{1.97}Fe_{0.03}Se_3$ samples (1.5 $\mu_B$) and the $Bi_{1.94}Fe_{0.06}Se_3$ sample (0.3 $\mu_B$). These differences may be due to the substantial variation in iron concentration among the samples and, consequently, are related to changes in magnetic interactions between impurities.

### 3.4 Heat Capacity of $Bi_{1.94}Fe_{0.06}Se_3$ Single Crystal

The heat capacity of a solid is primarily determined by contributions from two main participants: electrons and quantum vibrational states of the crystal lattice – phonons. In this case, the electronic heat capacity and phonon heat capacity based on the Debye model is calculated using the formula:

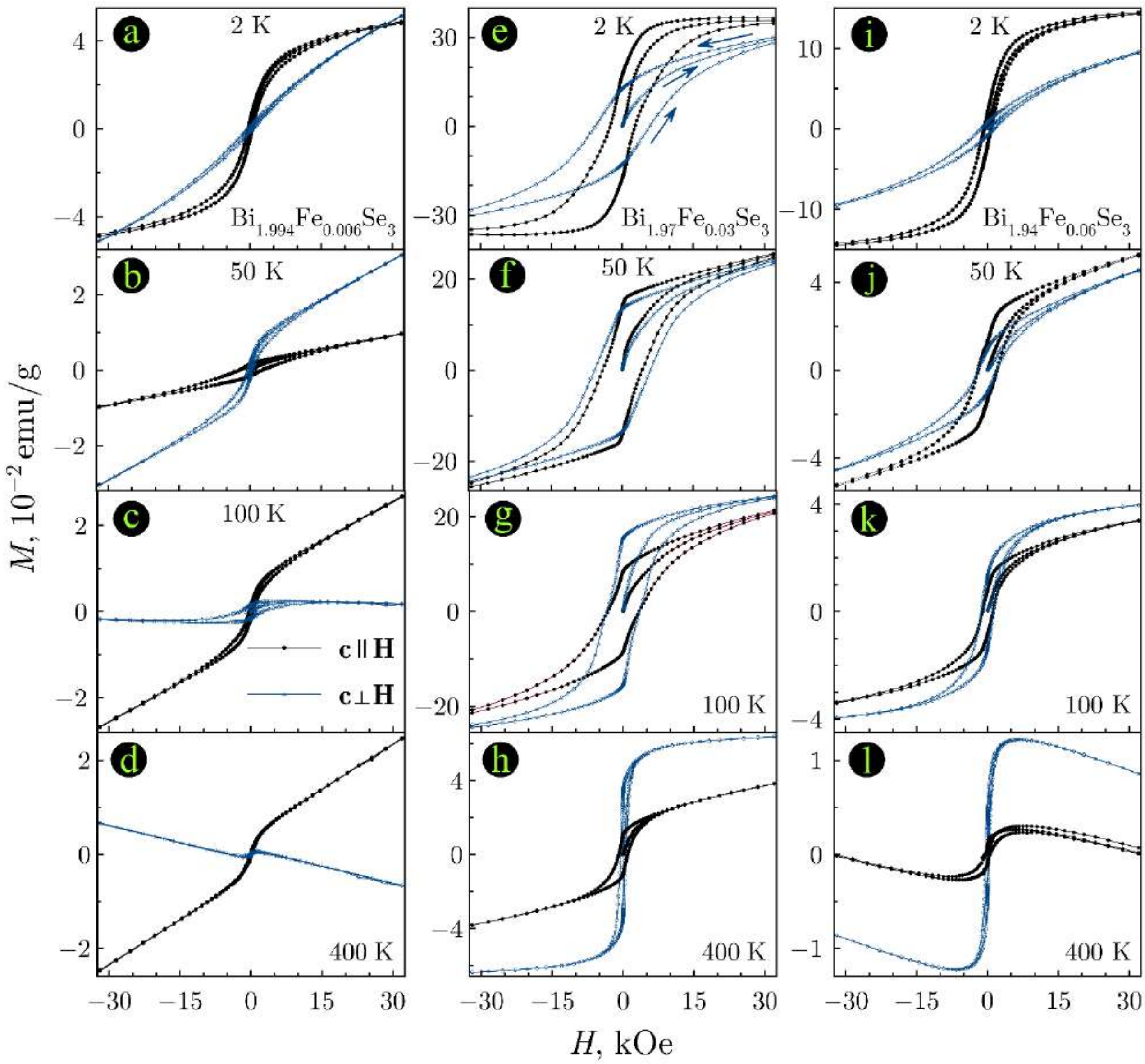


**Fig. 3.6** Central regions of magnetization isotherms $M(H)$. Temperatures in K and sample compositions are indicated on the graphs. Open symbols – **c** ⊥ **H**. Filled symbols – **c** ∥ **H**.

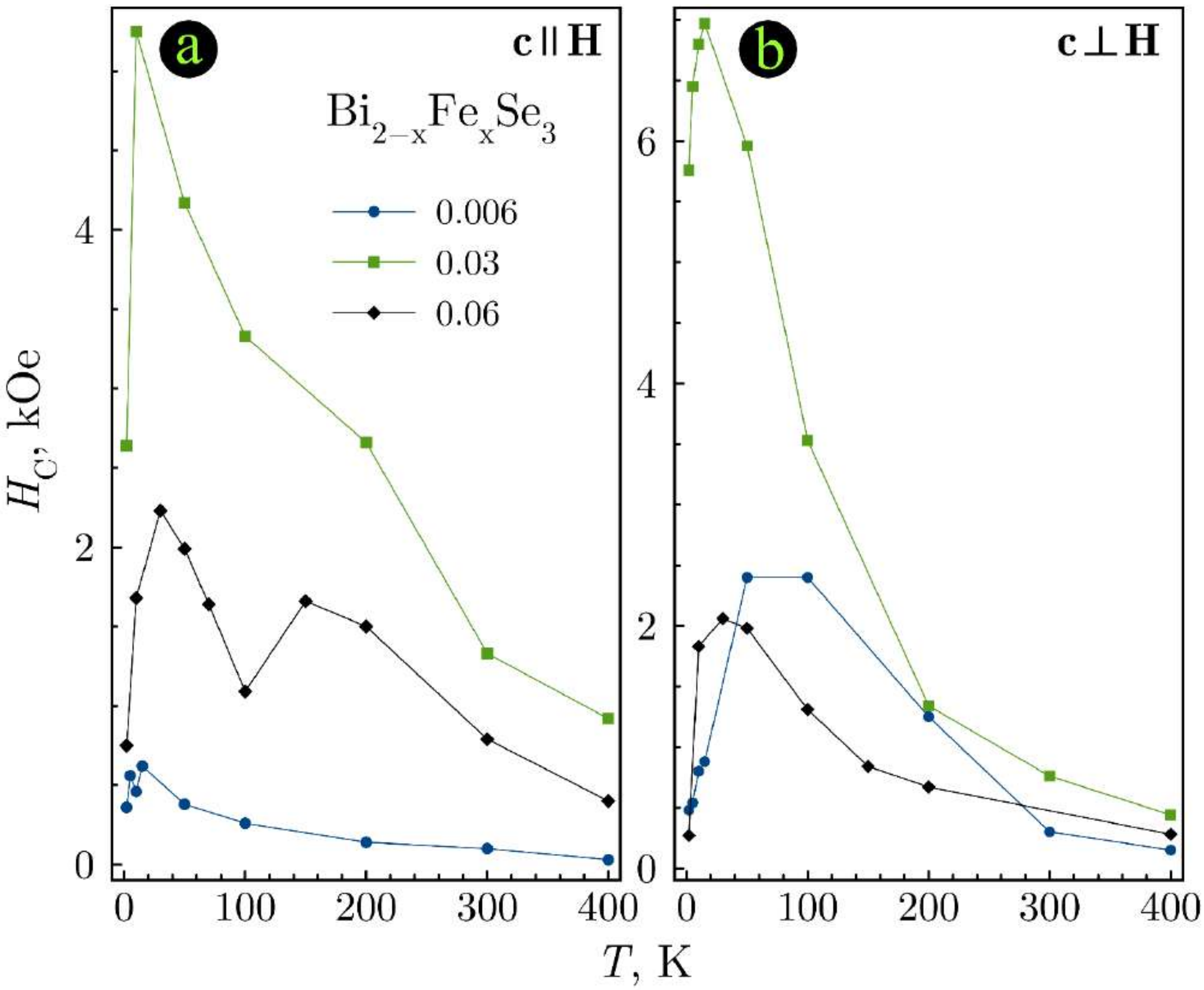


**Fig. 3.7** Temperature dependences of coercivity $H_c(T)$. Orientations in magnetic field and sample compositions are indicated on the graphs.

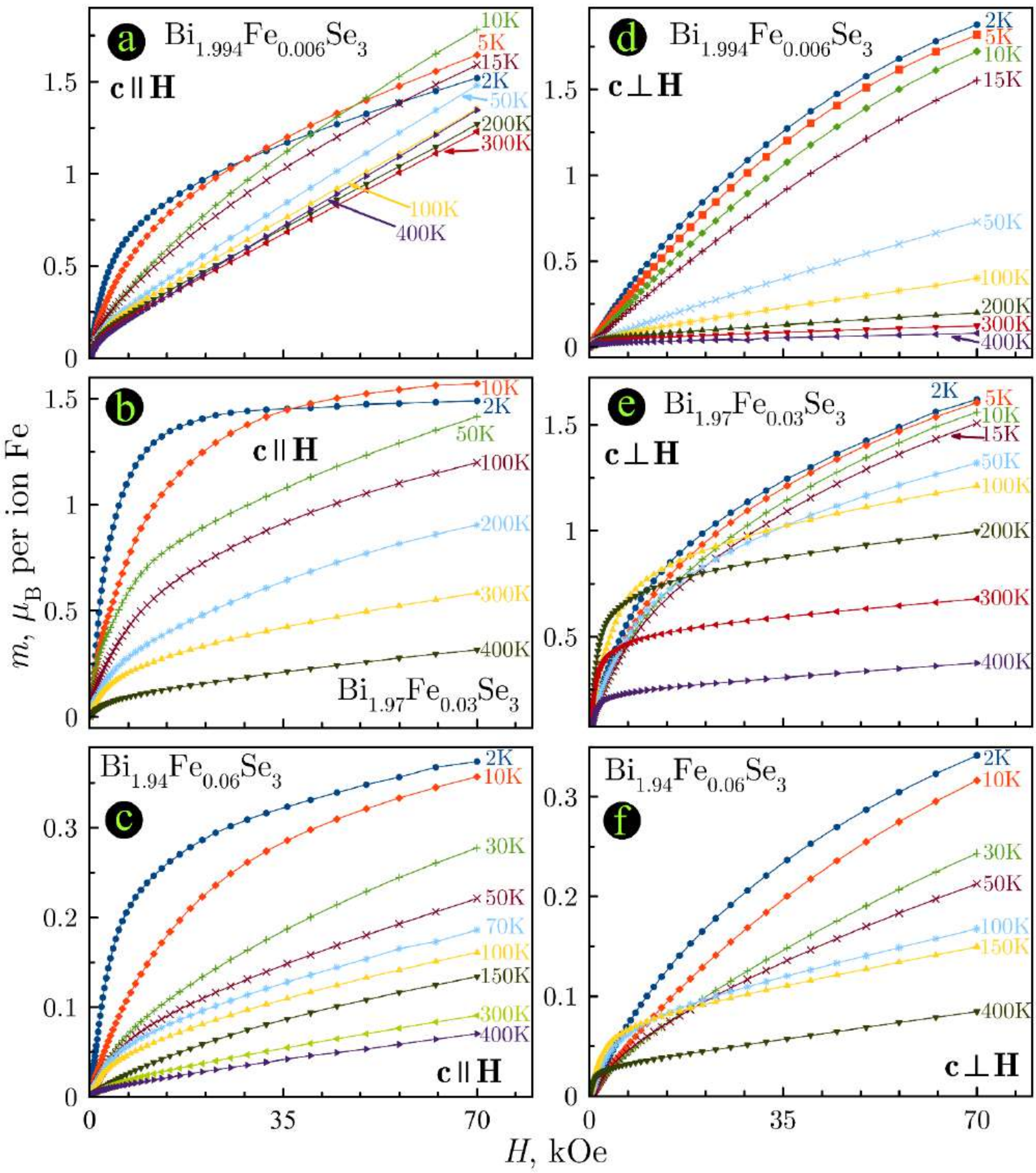


**Fig. 3.8** Primary magnetization isotherms accounting for the diamagnetic contribution to magnetization $\chi_0 H$. Temperatures in K, orientations in magnetic field, and sample compositions are indicated on the graphs.

$$C_V = \gamma T + 3r_D R\left(\frac{T}{\Theta_D}\right)^3 \int_0^{\Theta_D/T} \frac{x^4 e^x}{(e^x-1)^2}\,dx \qquad (3.3)$$

where $r_D$ is the number of vibrational modes, $R$ is the gas constant, $T$ is temperature, $\Theta_D$ is the Debye temperature related to the maximum vibration frequency. The value x is a dimensionless variable equal to the ratio $\hbar\omega/k_B T$, where $\hbar$ is Planck's constant, ω is the phonon frequency, and $k_B$ is the Boltzmann constant [90].

Electrons also contribute to heat capacity, especially at high temperatures. This contribution is typically described by the Fermi electron gas model. The electronic heat capacity is proportional to temperature: $C$e = $\gamma T$. Here $\gamma$ is the Sommerfeld constant, which depends on the density of electron states near the Fermi level [90].

At sufficiently low temperatures ($T \ll \Theta_D$), according to the Debye model, the phonon heat capacity is proportional to the cube of temperature:

$$C_V = \frac{12\pi^4}{5} N k_B \left(\frac{T}{\Theta_D}\right)^3 \qquad (3.4)$$

Thus, the total heat capacity of a solid at sufficiently low temperatures can be described as the sum of phonon heat capacity and electronic heat capacity contributions $C = \gamma T + \beta T_3$, where $\beta$ is the phonon coefficient [90].

During the study, heat capacity measurements of the $Bi_{1.94}Fe_{0.06}Se_3$ single crystal were performed as a function of temperature (Fig. 3.9). For data analysis, an approach based on Debye theory was used, which also included contributions from electrons. Numerical integration for calculating the Debye integral was performed using Simpson's method, which provided an accurate approximation of this integral. As a result of fitting the experimental data to the Debye model (3.3), the following constants were obtained: Debye temperature $\Theta_D$ = 182±2 K, number of vibrational modes $r_D = 4.83 \pm 0.07$, and Sommerfeld constant $\gamma = 0.01 \pm 0.0018\, mJ \cdot mol^{-1} K^{-1}$. The fitting results were in excellent agreement with experimental data for single-crystal $Bi_2Se_3$ [107], confirming the high quality of $Bi_{1.94}Fe_{0.06}Se_3$.

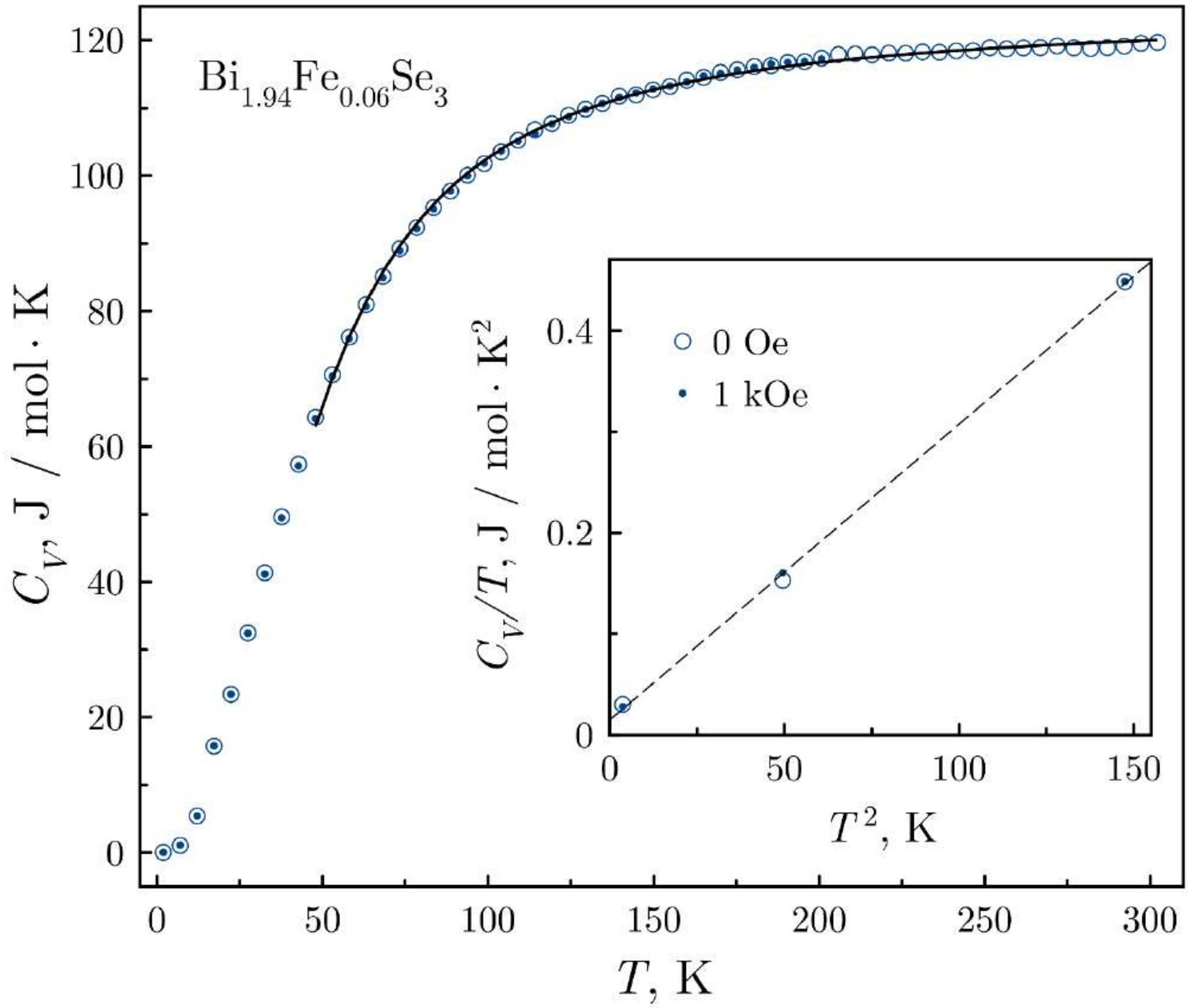


**Fig. 3.9** Temperature dependence of heat capacity $C(T)$ for the $Bi_{1.94}Fe_{0.06}Se_3$ single crystal at zero magnetic field and in a field of 1 kOe. Solid line represents the Debye model fit. Dashed line shows the linear approximation of electronic heat capacity.

### 3.5 Discussion

The bifurcation of ZFC and FC magnetic susceptibility temperature dependence curves (Figs. 3.2-3.5) and hysteresis in $M(H)$ dependencies (Fig. 3.6) unambiguously indicate the ferromagnetic nature of the phase transition. The absence of a paramagnetic phase in high magnetic fields distinguishes the $Bi_{1.97}Fe_{0.03}Se_3$ sample from the others. Negative paramagnetic temperatures $\theta$, obtained from Curie-Weiss dependencies for magnetic susceptibility in the paramagnetic state, indicate a tendency toward antiferromagnetic arrangement of iron magnetic moments and a possible antiferromagnetic component of ordering below the second phase transition. The results of the temperature dependence study of coercivity correlate with this latter assumption.

In layered chalcogenide magnetic semiconductors, ferromagnetic ordering arises due to indirect RKKY exchange interaction between iron ions involving free charge carriers [108]. Theoretical works [17, 18] also predict the possibility of antiferromagnetism in iron-doped $Bi_2Se_3$ crystals, caused by superexchange interaction. A recent inelastic neutron scattering study [109] discussed the possibility of indirect exchange between impurity antiferromagnetic dimers within TI quintets of $(Sb_{1-x}Mn_x)_2Te_3$, and ferromagnetic exchange of impurities between quintets. Thus, in magnetically doped TIs, the coexistence of two magnetic phases is possible in the case of a homogeneous state of the impurity phase in the TI matrix.

The significant decrease in magnetization measured in ZFC and FC modes below 121 K ($Bi_{1.994}Fe_{0.006}Se_3$, $Bi_{1.97}Fe_{0.03}Se_3$) and below 135 K ($Bi_{1.94}Fe_{0.06}Se_3$) for $\mathbf{c} \perp \mathbf{H}$ sample orientation with decreasing temperature is characteristic of both antiferromagnets when magnetic field is applied along the easy magnetization axis and spin glasses. Therefore, one can assume the coexistence of a ferromagnetic phase and either a spin glass state or antiferromagnetic ordering in this temperature range. It should be noted that weak high-temperature phase transitions at $T$>400 K, noticeable in ZFC and FC susceptibility curves at low fields, may be due to the contribution of magnetically ordered inclusions of iron-selenium compounds or other nanoparticles

[110]. In work [111], it was shown that antiferromagnetic clusters form with sufficiently strong iron doping of bismuth selenide (8% Fe per $Bi_2Se_3$). At $T \approx |\theta|$, an antiferromagnetic phase transition is expected. Unlike the ferromagnetic state, in antiferromagnetism, the Curie-Weiss temperature can be several times (in absolute value) larger than the Néel temperature $T_N$ [112].

### 3.6 Chapter 3 Conclusions

The conducted studies revealed three magnetic transitions in $Bi_{2-x}Fe_xSe_3$ topological insulator single crystals with x=0.006, 0.03, and 0.06. Hysteresis loops in *M*(*H*) curves, obtained across the entire investigated temperature range from 2 K to 400 K, demonstrated the presence of ferromagnetic character of magnetic ordering at the bifurcation temperature of ZFC and FC curves around 335 K - the first phase transition. The ordering emerging as a result of the second phase transition below 121 K ($Bi_{1.994}Fe_{0.006}Se_3$, $Bi_{1.97}Fe_{0.03}Se_3$) and below 135 K ($Bi_{1.94}Fe_{0.06}Se_3$) has an antiferromagnetic component. Furthermore, below the temperatures of the second phase transition, ferromagnetic ordering can coexist with spin glass state and antiferromagnetic correlations.

# Chapter 4. Magnetic Studies of Chromium-Doped $Bi_2Se_3$ Topological Insulator

This chapter examines the magnetic properties of three single-crystal samples of $Bi_{2-x}Cr_xSe_3$ with x=0.01, 0.03, and 0.06 in the temperature range from 2 to 300 K. *dc* magnetization measurements demonstrated the coexistence of antiferromagnetic and ferromagnetic ordering along with paramagnetism. Their relative contributions depend on the chromium content. The ferromagnetic phase transition was suppressed by sufficiently high magnetic fields. The antiferromagnetic transition near 80 K does not show significant shift up to 50 kOe. In the Curie-Weiss law approximation, the effective magnetic moment $\mu_{\mathrm{eff}}$ is close to 4.9 $\mu_{\mathrm{B}}$, which corresponds to divalent chromium ions. Metamagnetic phenomena were observed for crystals with x=0.03 and 0.06 [113].

### 4.1 Magnetic Susceptibility of Chromium-Doped $Bi_2Se_3$ Single Crystals

Figs. 4.1 and 4.2 show the temperature dependencies of *dc* magnetic susceptibility $\chi$, measured at magnetic fields of 100 Oe and 1, 5, and 50 kOe for two sample orientations: **c** || **H** and **c** ⊥ **H**. A clear divergence between ZFC and FC curves at 1 kOe is observed only in the $Bi_{1.99}Cr_{0.01}Se_3$ sample with minimal chromium impurity content for both orientations. The bifurcation, confirming the emergence of ferromagnetic order, becomes noticeable below 240 K. The difference between ZFC and FC curves for $Bi_{1.97}Cr_{0.03}Se_3$ and $Bi_{1.94}Cr_{0.06}Se_3$ samples at 1 kOe is barely noticeable. The divergence of ZFC and FC curves in the $Bi_{1.99}Cr_{0.01}Se_3$ sample disappears at higher magnetic fields (inset in Fig. 4.1a and Fig. 4.2). This indicates that the ferromagnetic phase transition temperature has shifted below 2 K. Measurements at 100 Oe demonstrate the presence of weak ferromagnetism in the other two samples, $Bi_{1.97}Cr_{0.03}Se_3$ and $Bi_{1.94}Cr_{0.06}Se_3$, below approximately 200 and 60 K, respectively (inset in Fig. 4.1b). Thus, the ferromagnetic transition temperature decreases with increasing chromium concentration.

In contrast, the magnetic susceptibility curves for $Bi_{1.97}Cr_{0.03}Se_3$ and $Bi_{1.94}Cr_{0.06}Se_3$ crystals show maxima around 80 K, which are visible at all magnetic fields. These features are not accompanied by bifurcation of ZFC and FC curves. Such behavior is characteristic of antiferromagnetic order formation [114]. Measurements show that the antiferromagnetic transition temperature does not shift significantly with increasing magnetic field. However, the ZFC and FC curves noticeably diverge at lower temperatures in a field of 50 kOe. For the $Bi_{1.99}Cr_{0.01}Se_3$ crystal, no clear features associated with antiferromagnetic ordering are observed, but at magnetic fields above 5 kOe, a hint of a maximum becomes noticeable.

At this magnetic field, the ZFC and FC curves for the $Bi_{1.99}Cr_{0.01}Se_3$ sample merge, which facilitates the observation of their behavior. The magnetic susceptibility curves at temperatures above the antiferromagnetic transition in a 50 kOe field demonstrate paramagnetic behavior (see insets in Fig. 4.2).

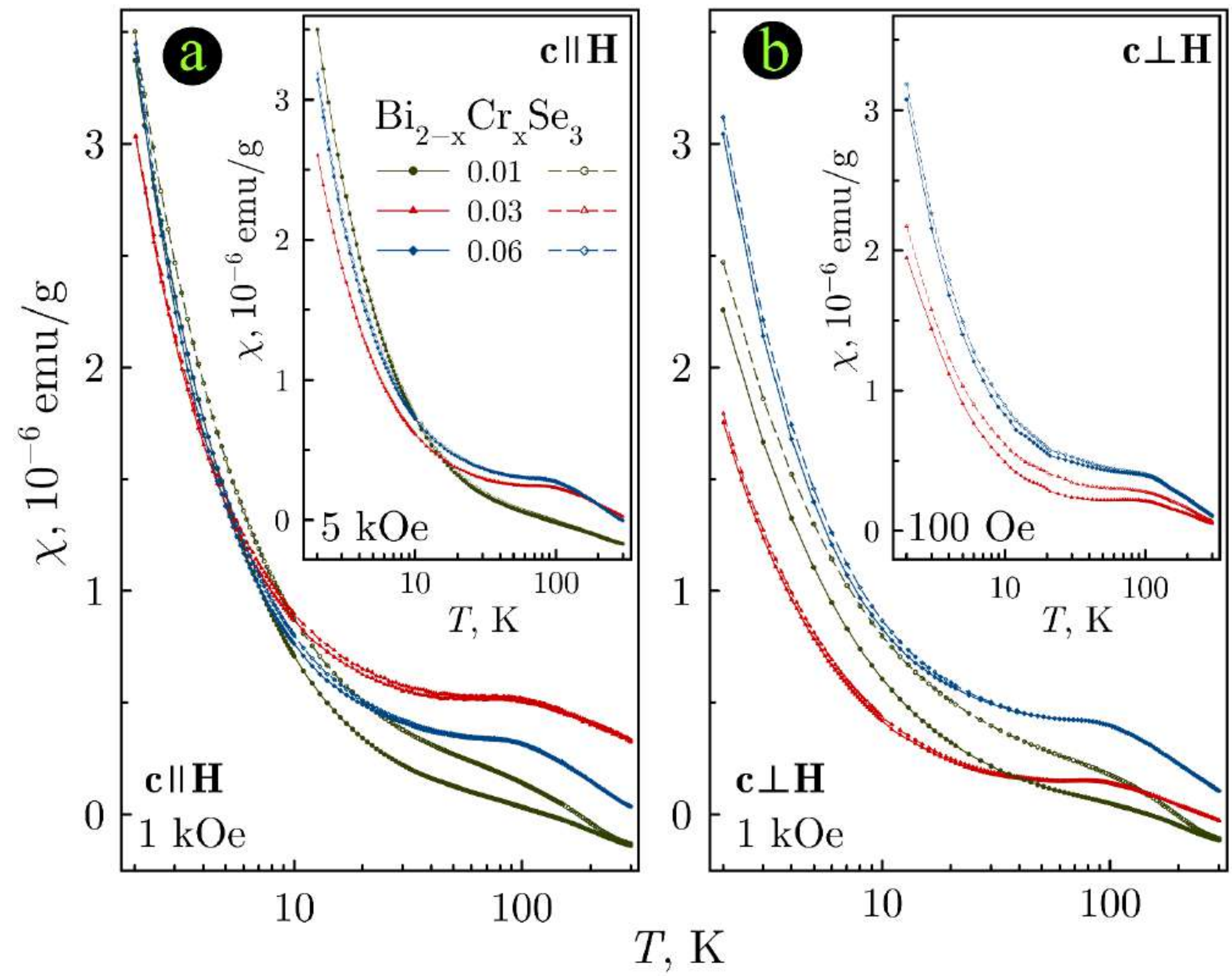


**Fig. 4.1** Temperature dependences of *dc* magnetic susceptibility $\chi$ measured at 1 kOe field for sample orientations **c** || **H** (a) and **c** ⊥ **H** (b). The inset in Fig. (a) shows $\chi$ curves at 5 kOe field for **c** || **H** orientation. The inset in Fig. (b) shows $\chi$ curves at 100 Oe field for **c** ⊥ **H** orientation. Dark symbols represent ZFC data. Light symbols represent FC data.

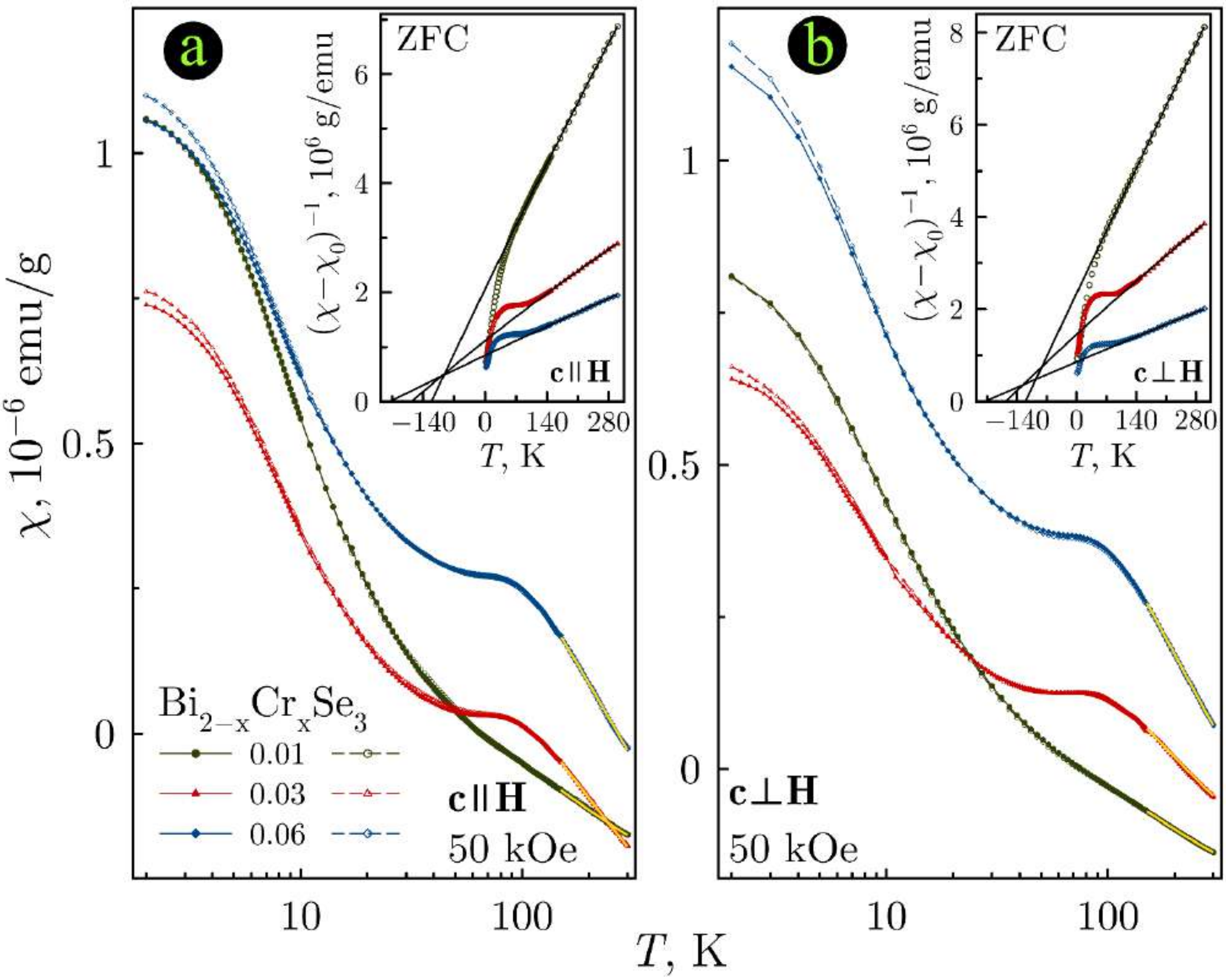


**Fig. 4.2** Temperature dependences of *dc* magnetic susceptibility $\chi$ measured at 50 kOe field for sample orientations **c** || **H** (a) and **c** ⊥ **H** (b). The insets show temperature dependences of inverse *dc* magnetic susceptibility $\chi^{-1}$, calculated from measurements at 50 kOe field. Dark symbols represent ZFC data. Light symbols represent FC data.

and can be approximated by the Curie-Weiss law (3.1) with the addition of a temperature-independent diamagnetic contribution $\chi_0$. The obtained fitting parameters $\mu_{eff}$, $\chi_0$, and $\theta$ are presented in Table 4.1 along with the impurity concentration values $N$, calculated from the crystalline composition using formula (3.2). The effective magnetic moments μeff, calculated using formula (1.4), are similar for all samples in both crystal orientations and close to 4.9 $\mu_B$. Assuming that the orbital moment of chromium is "frozen" by the crystal field of the $Bi_2Se_3$ matrix [106, 76], the spin moment can be written as $\mu_{eff} = g\sqrt{S(S+1)}\mu_B$, where the g-factor of chromium ions equals 2 and $S$ is the total spin. Thus, the spin of the chromium ion is close to 2, which corresponds to the $Cr^{2+}$ valence state.

### 4.2 Magnetization Isotherms of Chromium-Doped $Bi_2Se_3$ Single Crystals

The magnetization isotherms $M(H)$, measured in the temperature range from 2 K to 300 K, reflect the coexistence of different magnetic contributions: antiferromagnetic, ferromagnetic, diamagnetic, and paramagnetic. Fig. 4.3 shows the magnetization isotherms $M(H)$. It is evident that their relative importance and features varied.

The coercivity $H_c$, which determines the width of hysteresis loops, significantly depends on temperature and Cr concentration. The temperature dependence of coercivity for $Bi_{1.99}Cr_{0.01}Se_3$ and $Bi_{1.97}Cr_{0.03}Se_3$ samples is shown in Fig. 4.4a. The coercivity of $Bi_{1.94}Cr_{0.06}Se_3$ sample is significant only at 10 K, while for $Bi_{1.99}Cr_{0.01}Se_3$ it reaches maximum at 50 and 100 K and decreases with temperature reduction. It was noted that a sharp drop in coercivity at low temperatures was also observed in iron-doped $Bi_2Se_3$ (Fig. 3.7). The coercivity in $Bi_{1.97}Cr_{0.03}Se_3$ does not exceed experimental accuracy limits at all temperatures. The hysteresis loops in $Bi_{1.99}Cr_{0.01}Se_3$ at 50 K for both sample orientations in magnetic field are shown in Fig. 4.4b as an example.

Table 4.1 Curie-Weiss temperature $\theta$, effective moment $\mu_{\mathrm{eff}}$ of chromium ions, and diamagnetic contribution to susceptibility $\chi_0$, calculated using the Curie-Weiss law (Fig. 4.2). $N$ represents the number of chromium ions per gram of sample.

| Sample | $N / g^{-1}$ | $\theta / K$ | $\mu_{eff} / \mu_B$ | | $\chi_0 / emu \cdot g^{-1}$ | |
|---|---|---|---|---|---|---|
| | | | $\mu^{\parallel}_{eff}$ | $\mu^{\perp}_{eff}$ | $\chi_0^{\parallel} / K$ | $\chi_0^{\perp} / K$ |
| $Bi_{1.99}Cr_{0.01}Se_3$ | $1.05 \cdot 10^{19}$ | $-120 \pm 5$ | 5.1 | 4.9 | $-0.32 \cdot 10^{-6}$ | $-0.26 \cdot 10^{-6}$ |
| $Bi_{1.97}Cr_{0.03}Se_3$ | $2.8 \cdot 10^{19}$ | $-166 \pm 7$ | 4.9 | 4.6 | $-0.50 \cdot 10^{-6}$ | $-0.28 \cdot 10^{-6}$ |
| $Bi_{1.94}Cr_{0.06}Se_3$ | $5.6 \cdot 10^{19}$ | $-215 \pm 8$ | 4.9 | 4.7 | $-0.55 \cdot 10^{-6}$ | $-0.42 \cdot 10^{-6}$ |

The magnetization $M'$ was determined from experimental data by subtracting diamagnetic, paramagnetic, and antiferromagnetic contributions, which depend linearly on the field at a given temperature.

The ferromagnetic contribution to susceptibility saturates at around 30 kOe. The $M'(H)$ curve at 50 K for $Bi_{1.97}Cr_{0.03}Se_3$ with **c** || **H** is presented in Fig. 4.4c. The S-shaped curve confirms the presence of ferromagnetic order in $Bi_{1.97}Cr_{0.03}Se_3$. Unlike $Bi_{1.99}Cr_{0.01}Se_3$, the $Bi_{1.97}Cr_{0.03}Se_3$ sample shows soft magnetic material properties with a saturation field of about 15 kOe.

The magnetic moment per Cr ion was calculated from the magnetization isotherm curves, taking into account the diamagnetic contribution found from the Curie-Weiss law fitting.

## 4.3 Discussion

*Ab initio* calculations [19, 115, 116] and experimental XANES and XAFS studies [117, 118] have shown that chromium ions substitute trivalent bismuth ions in the $Bi_2Se_3$ lattice. In accordance with this finding, chromium ions were often assumed to have a 3+ oxidation state [73, 77]. In [73], the estimated $S$ value was close to 1.7. The authors interpreted this as the presence of both $Cr^{3+}$ and $Cr^{2+}$ ions: trivalent ions at bismuth host sites and divalent ions between quintuple layers (Fig. 1.4f). However, further X-ray spectroscopy studies revealed the divalent character of Cr ions when substituting Bi, despite the trivalent nature of Bi [117, 118]. Local structural relaxation caused by Cr impurity incorporation reduces the distance between Cr and Se ions, thereby enhancing the covalent nature of the Cr-Se bond. The research results confirm the divalent character of substituted chromium ions.

The Curie-Weiss law fitting yields negative and relatively high paramagnetic temperatures $\theta$, indicating the presence of antiferromagnetic correlations in all doped TIs.

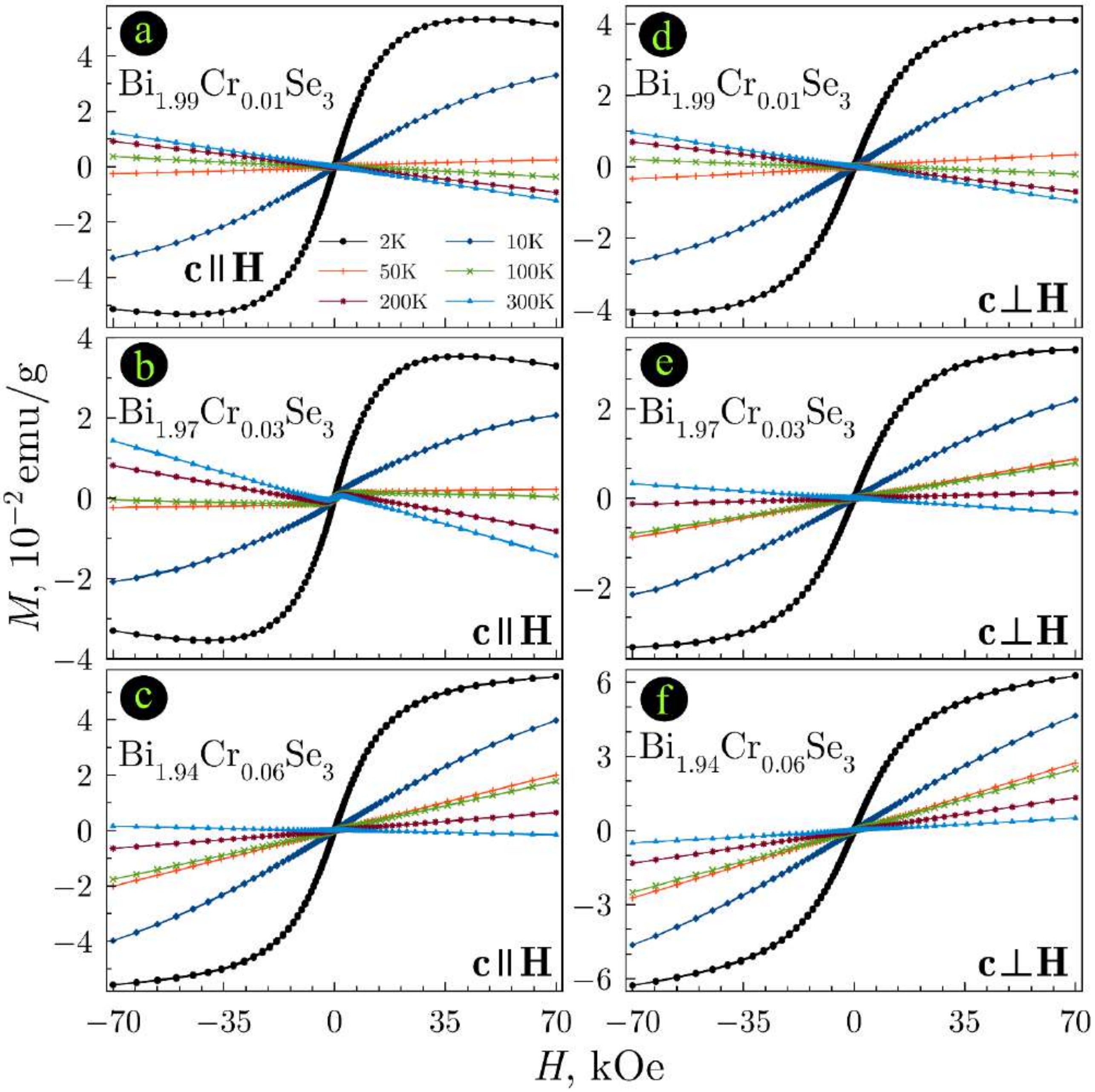


**Fig. 4.3** *dc* magnetization isotherms of $Bi_{2-x}Cr_xSe_3$ single crystals. Sample orientation in magnetic field, temperatures in K, and sample compositions are indicated on the graphs.

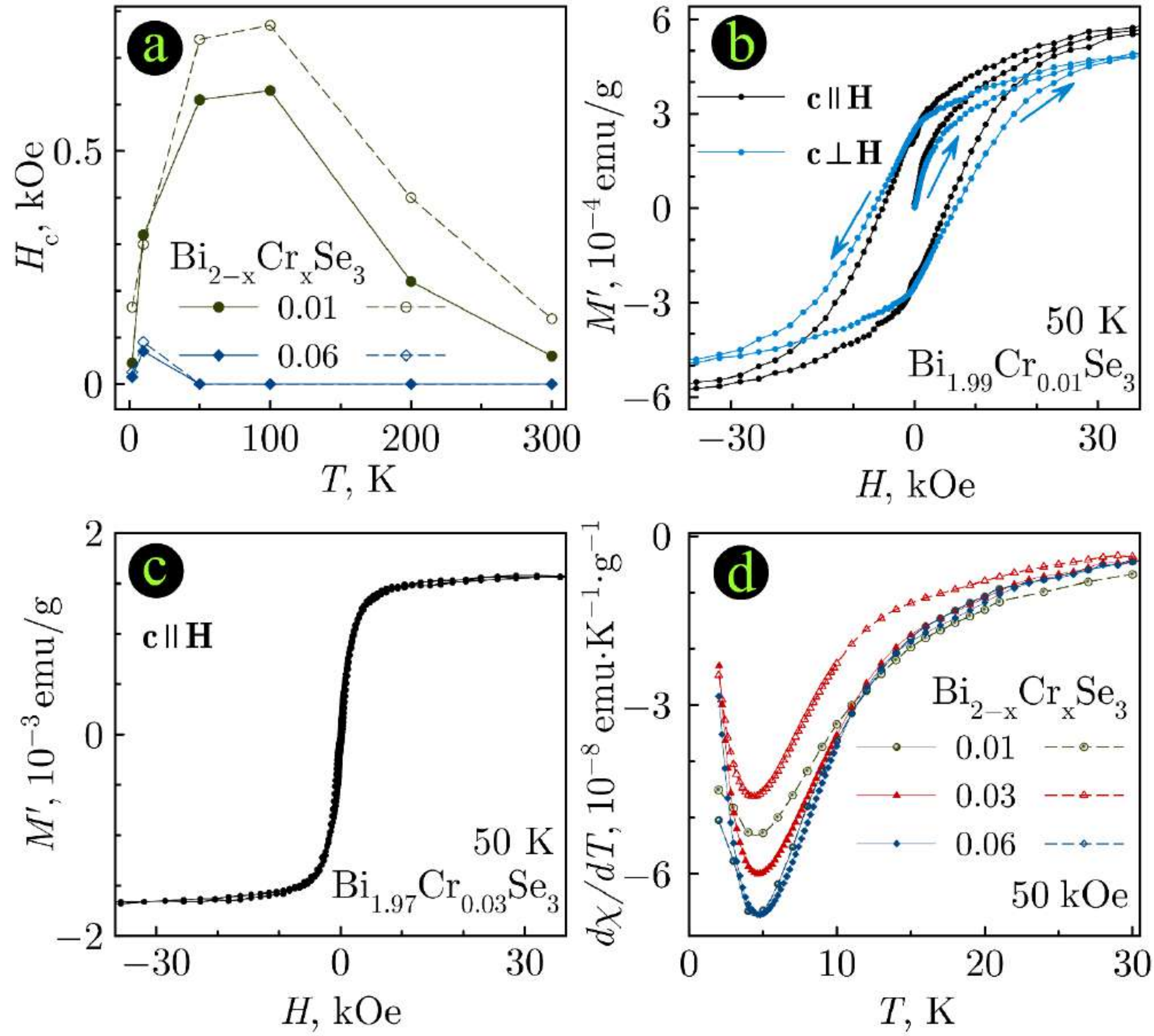


**Fig. 4.4** (**a**) Coercivity $H_c$ of $Bi_{1.99}Cr_{0.01}Se_3$ and $Bi_{1.94}Cr_{0.06}Se_3$ samples. (**b**) *dc* magnetization isotherms *M′* of $Bi_{1.99}Cr_{0.01}Se_3$ sample. (**c**) *dc* magnetization isotherms M′ of $Bi_{1.97}Cr_{0.03}Se_3$ sample at 50 K for c ∥ H orientation. (**d**) First derivatives *dχ*/*dT* of ZFC *dc* magnetic susceptibility curves measured at 50 kOe. Dark symbols represent **c** ∥ **H**. Light symbols represent **c** ⊥ **H**.

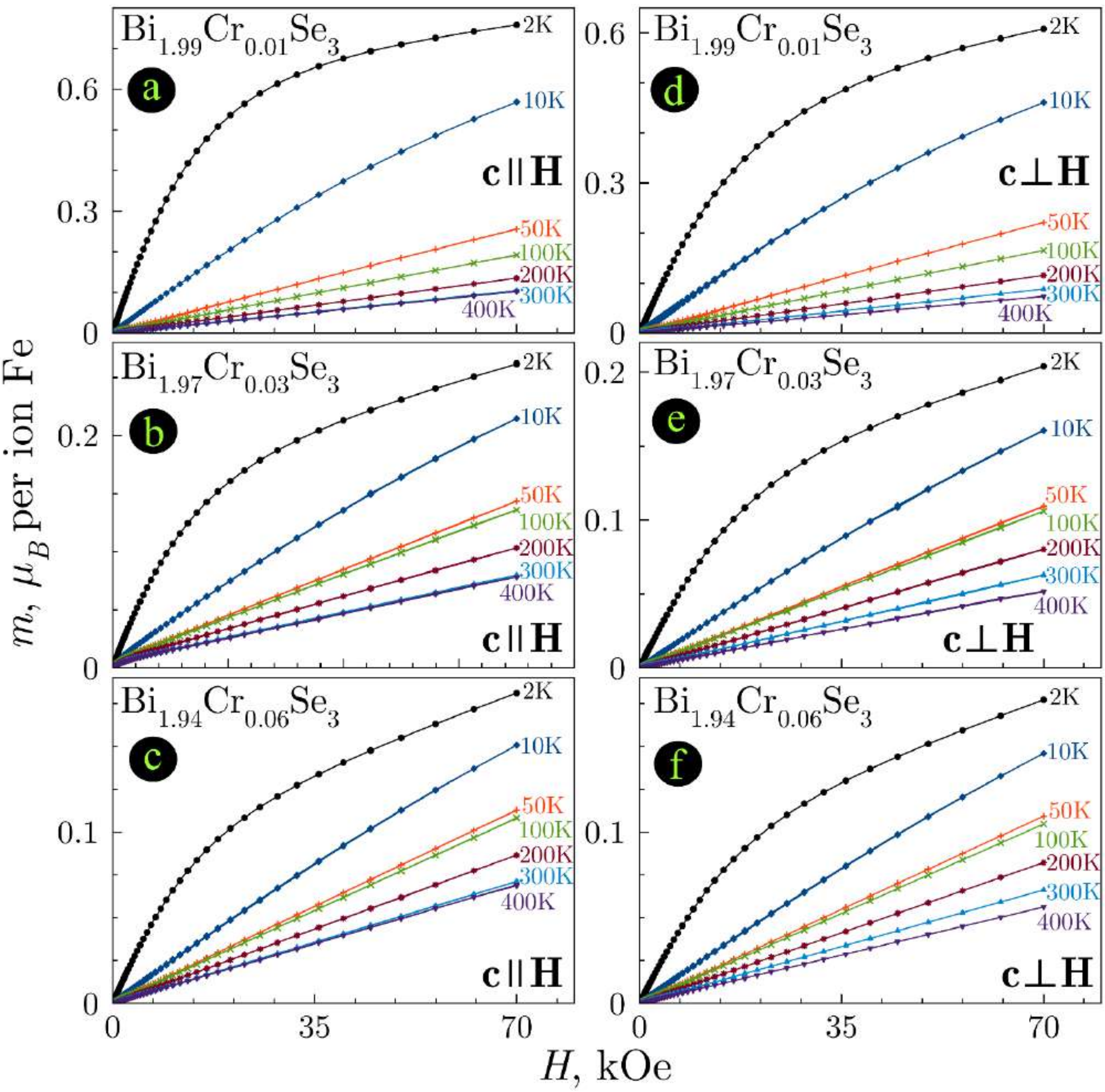


**Fig. 4.5** Primary *dc* magnetization isotherms accounting for the diamagnetic contribution to magnetization *M′*. Temperatures in K, magnetic field orientations, and sample compositions are indicated on the graphs.

The Néel temperature $T_N$, marked by features in the $\chi(T)$ curves, is significantly lower than the absolute values of $\theta$, especially for $Bi_{1.97}Cr_{0.03}Se_3$ and $Bi_{1.94}Cr_{0.06}Se_3$, which is a characteristic feature of antiferromagnets with indirect long-range exchange interaction [106]. The sharp decrease in magnetic moment per Cr ion (with increasing Cr concentration) (Fig. 4.5) apparently also results from enhanced antiferromagnetic correlations in $Bi_{1.97}Cr_{0.03}Se_3$ and $Bi_{1.94}Cr_{0.06}Se_3$ samples.

The diamagnetic contribution to magnetic susceptibility is due to atomic shells and localized valence band electrons. Additionally, there may be a contribution from mobile charge carriers. Undoped $Bi_2Se_3$ and $Bi_2Te_3$ crystals possess diamagnetic susceptibility on the order of $10^{-7}$ emu/g [119]. The possible anisotropy of the diamagnetic term is related to the anisotropy of charge carrier effective mass, which affects Landau diamagnetism [106]. Doping with transition metals can lead to changes in anisotropy, as observed for $Bi_{2-x}Fe_xTe_3$ [119]. As shown in Table 1, the diamagnetic contribution in the samples is anisotropic, with susceptibility being higher for **c** || **H** orientation. For each orientation, susceptibility $\chi_0$ increases (in absolute value) with increasing Cr content. This indirectly indicates an increased role of mobile charge carriers resulting from Cr doping.

Figures 4.1 and 4.2 show that the paramagnetic contribution likely dominates the magnetic susceptibility behavior below 20 K. To confirm this interpretation, the first derivatives of ZFC susceptibility as a function of temperature were plotted for all samples at 50 kOe field in Fig. 4.4d. When studying paramagnetic magnetization at high magnetic fields and low temperatures, for the quantum case, it is customary to use the Brillouin function $B_S(x)$:

$$M = NgS\mu_B\left[B_S(x)\right] = NgS\mu_B\left[\frac{2S+1}{2S}\coth\frac{(2S+1)x}{2S} - \frac{1}{2S}\coth\frac{x}{2S}\right] \qquad (1.3)$$

where $x \equiv gS\mu_B H / k_B T$.

First derivatives show minima at temperatures ranging from 4.5 to 4.9 K. The paramagnetic susceptibility is proportional to the Brillouin function. Numerical analysis of the Brillouin function for $g = 2$ and $H = 50$ kOe shows minima in the first derivative of susceptibility, whose positions on the temperature axis depend on $S$. Specifically, the temperature of the first derivative minimum is 5.0 K and 4.3 K for $S = 2$ and 3/2, respectively. The S values estimated from Fig. 4.3(d) lie in the range from 1.7 to 1.9. These are slightly lower than $S = 2$, which were determined from the Curie-Weiss law at high temperatures and correspond to $Cr^{2+}$. The difference may be due to other temperature-dependent contributions to magnetic susceptibility associated with magnetic ordering. Alternative explanations are also possible. The paramagnetic contribution to susceptibility at low temperatures evidently comes from chromium magnetic ions that do not participate in magnetic ordering. These ions may enter the interquintuple space instead of host bismuth atom positions and have a different degree of covalent bonding.

$Bi_{1.97}Cr_{0.03}Se_3$ and $Bi_{1.94}Cr_{0.06}Se_3$ samples exhibit metamagnetism, as shown in Fig. 4.6. The $M(H)$ magnetization curves were obtained by subtracting the diamagnetic contribution. A significant metamagnetic effect was observed in $Bi_{1.94}Cr_{0.06}Se_3$ at high temperatures above 50 K. $Bi_{1.97}Cr_{0.03}Se_3$ shows the metamagnetic effect across the entire range from 2 to 300 K. The primary, secondary, and tertiary magnetization curves coincide with each other at low fields $|H|<40$ Oe. Then the hysteresis loops open with increasing field and collapse at higher fields. Metamagnetism is observed both above and below antiferromagnetic phase transitions in $Bi_{1.97}Cr_{0.03}Se_3$ and $Bi_{1.94}Cr_{0.06}Se_3$. Thus, this phenomenon cannot be caused by field-induced spin-flop effects in the antiferromagnetic fraction. It can be assumed that this is a transition occurring in the paramagnetic fraction to a ferromagnetic state. The field-induced transition to the magnetic phase is completely irreversible, similar to what was observed, for example, for the transition from paramagnetic to ferromagnetic state in a magnetic field in [120]. The divergence of hysteresis loops indicates a first-order phase transition. Metamagnetic transitions from paramagnetic states are relatively rare.

In magnets exhibiting magnetic instability, field-induced phase transitions can transform the system from paramagnetic to ferromagnetic phases.

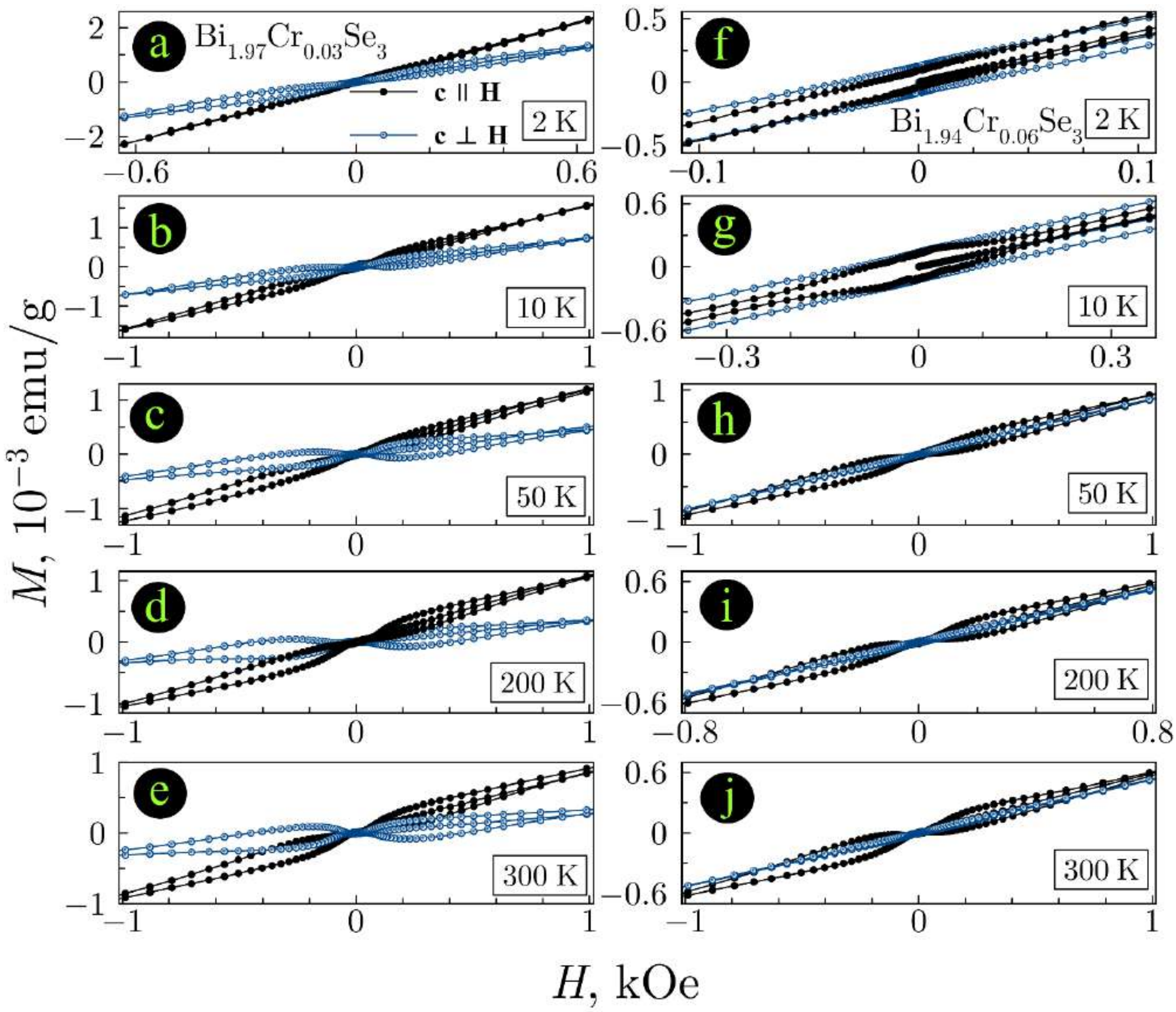


**Fig. 4.6** Central *dc* magnetization isotherm curves for $Bi_{1.97}Cr_{0.03}Se_3$ (a-e) and $Bi_{1.94}Cr_{0.06}Se_3$ (f-j) samples. Temperatures in K, magnetic field orientations, and sample compositions are indicated on the graphs.

This phenomenon, known as itinerant electron metamagnetism or band metamagnetism, was first observed in some intermetallic compounds $YCo_2$ and $LuCo_2$ at very strong magnetic fields of about 500 - 800 kOe. The basis of these transitions is the threshold nature of ferromagnetism in itinerant electron systems. As a result, if the itinerant electron system is in a paramagnetic state at zero field, then upon reaching a certain field $H_M$, a metamagnetic transition of the itinerant electron system occurs from paramagnetic to ferromagnetic state.

It is worth noting that the observation of itinerant metamagnetism currently does not require enormous magnetic fields. In the $ErCo_2$ intermetallic compound, itinerant metamagnetism is observed in fields around 9 kOe and higher (Fig. 1.3e) [121], while in dichalcogenide metamagnets $Co(S_{1-x}Se_x)_2$, it occurs in the range of 2 kOe and above [122].

As an example, one can cite the metamagnetic transition caused by itinerant electrons [123], however, magnetic transformations with increasing field in $Bi_2Se_3$ require additional research to understand their physical nature.

## 4.4 Chapter 4 Conclusions

The complex magnetic behavior of chromium-doped $Bi_2Se_3$ topological insulator crystals indicates that some chromium ions are magnetically ordered, while other chromium ions remain in a paramagnetic state. The magnetic ordering can be either ferromagnetic or antiferromagnetic. The coexistence of ferromagnetism and antiferromagnetism was observed in all studied samples. The relative significance of ferromagnetism decreases with increasing chromium content. Coercivity was substantial only in the $Bi_{1.99}Cr_{0.01}Se_3$ sample. Fitting the temperature dependence of magnetic susceptibility in the fully paramagnetic phase at a field of 50 kOe showed that the spin of chromium ions equals 2, corresponding to the $Cr^{2+}$ charge state. Metamagnetism was discovered in samples with higher impurity concentrations. The metamagnetic transition likely occurs in the paramagnetic fraction. The appearance of hysteresis indicates metamagnetism caused by a first-order phase transition.

# Chapter 5. Magnetic Studies of Iron-Doped $WTe_2$ Weyl Semimetal

This chapter examines the magnetic properties of doped $Fe_{0.03}W_{0.97}Te_2$ single crystals, both annealed and unannealed, in comparison with undoped $WTe_2$. *dc* magnetization measurements were conducted from 1.8 to 400 K. Pronounced ferromagnetic ordering was discovered, which was affected by annealing. Anomalies associated with antiferromagnetism and paramagnetism were also detected. The magnetic ordering was suppressed by a field of 60 kOe. An increase in magnetic susceptibility with rising temperature was observed at high temperatures in all samples and was analyzed using a model developed for Weyl semimetals. Curie-Weiss law fitting at 60 kOe showed that the effective magnetic moment is close to that of $Fe^{2+}$. Metamagnetism was demonstrated for the unannealed doped $WTe_2$ crystal. Heat capacity data for the iron-doped sample are consistent with the results for undoped $WTe_2$ [124].

## 5.1 Magnetic Susceptibility and Magnetization Isotherms of Undoped $WTe_2$ Weyl Semimetal

Fig. 5.1 shows the temperature dependencies of ZFC and FC magnetic *dc* susceptibility $\chi$ of $WTe_2$ single crystal, obtained under applied magnetic fields of 1 kOe and 60 kOe, as well as magnetization isotherms at 10 K. The ZFC and FC curves coincide across the entire temperature range and are consistent with the non-magnetic nature of this Weyl semimetal.

The magnetic susceptibility curves are notably smaller than the corresponding values in unannealed $Fe_{0.03}W_{0.97}Te_2$ and are negative, confirming its diamagnetic properties [125]. Weak paramagnetism below 60 K may be caused by a small amount of magnetic impurities or defects. It should be noted that the increase in magnetic susceptibility above 60 K is similar to the magnetic susceptibility behavior observed for the unannealed $Fe_{0.03}W_{0.97}Te_2$ sample (see below). The linear dependence of magnetization isotherms (Fig. 5.1b) clearly indicates the dominance of the diamagnetic contribution in the sample.

## 5.2 Magnetic Susceptibility of Iron-Doped $WTe_2$ Single Crystal

Fig. 5.2 shows the temperature dependencies of susceptibility $\chi$ for the unannealed $Fe_{0.03}W_{0.97}Te_2$ sample at a magnetic field of 100 Oe in two sample orientations: **c** || **H** and **c** ⊥ **H**. Pronounced bifurcations of ZFC and FC curves are visible below 300 K, indicating the emergence of ferromagnetic ordering. The ferromagnetic phase transition temperature decreases to approximately 170 and 20 K when the magnetic field is increased to 1 and 10 kOe, respectively (Fig. 5.2a). For comparison, the ferromagnetic transitions in Cr-doped $WTe_2$ [89], in contrast, did not show significant shifts and remained below room temperature when the magnetic field was increased from 0 to 1 kOe. In a 60 kOe field, the ferromagnetic transition shifts below our measurement limit, as the ZFC and FC susceptibility curves become close to each other. At magnetic field of 100 Oe and 1 kOe, maxima are observed in the ZFC

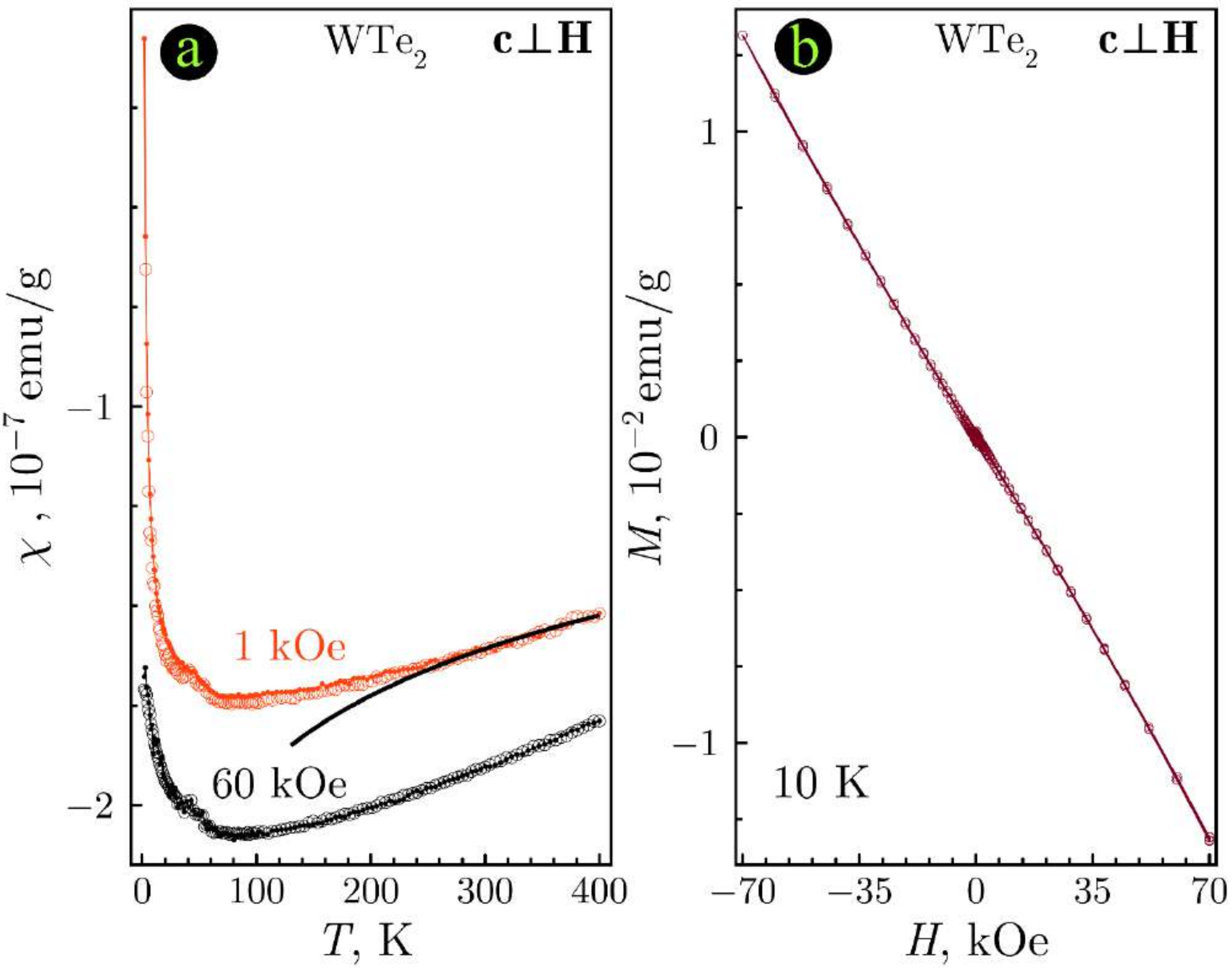


**Fig. 5.1 a**) *dc* magnetic susceptibility curves of $WTe_2$ measured in fields of 1 kOe and 60 kOe. **b**) *dc* magnetization isotherms of $WTe_2$ measured at 10 K with **c** ⊥ **H** orientation.

curves for the **c** ⊥ **H** orientation (Fig. 5.2b), demonstrating a second, low-temperature ferromagnetic transition. This transition shifts to lower temperatures as the magnetic field increases from 100 Oe to 1 kOe. Similar features are not observed for the other sample orientation. Instead, a ZFC susceptibility maximum appears near 10 K. Magnetic anomalies associated with the second ferromagnetic transition are not observed at fields of 10 and 60 kOe (Fig. 5.3) due to the decrease in transition temperature. Fig. 5.2 shows a notable increase in both ZFC and FC susceptibility with decreasing temperature below 10 K. This behavior likely corresponds to a paramagnetic contribution that becomes noticeable at low temperatures against the background of ferromagnetism. The magnetic susceptibility at 60 kOe anomalously increases from approximately 250 to 400 K. This increase is weaker for the **c** ⊥ **H** orientation. For the **c** || **H** orientation, a similar increase in susceptibility is observed at lower fields (Fig. 5.2a). Note that Fig. 5.2b shows no susceptibility increase for unannealed $Fe_{0.03}W_{0.97}Te_2$ up to 400 K. It can be assumed that for this specific case, the susceptibility minimum and subsequent increase shift above the upper temperature limit of our measurements.

The temperature dependencies of susceptibility for the annealed $Fe_{0.03}W_{0.97}Te_2$ single crystal are shown in Fig. 5.4 for the **c** || **H** orientation. Ferromagnetic ordering with a phase transition above 400 K at 100 Oe is evidenced by strong divergence of ZFC and FC curves. This ordering is not observed throughout the entire temperature range of our experiments at a magnetic field of 60 kOe. Other magnetization anomalies related to phase transitions appear on the temperature dependencies at fields of 100 Oe and at 1 and 10 kOe below room temperature; however, they are completely smoothed out at 60 kOe. It is worth noting the pronounced increase in susceptibility at low temperatures. At 60 kOe, the susceptibility behavior follows the Curie law in a limited temperature range from 125 to 265 K (see inset to Fig. 5.4b). In this range, the susceptibility follows the Curie-Weiss law (3.1), with a Weiss temperature $\theta$=123 K, Curie-Weiss constant $C$=1.93×10$^{-4}$ emu/g, temperature-independent diamagnetic contribution $\chi_0$ = 1.03×10$^{-8}$ emu/g, and effective magnetic moment $\mu_{\mathrm{eff}}$ = 4.7 $\mu_{\mathrm{B}}$, which is close to the effective moment of $Fe^{2+}$ [106].

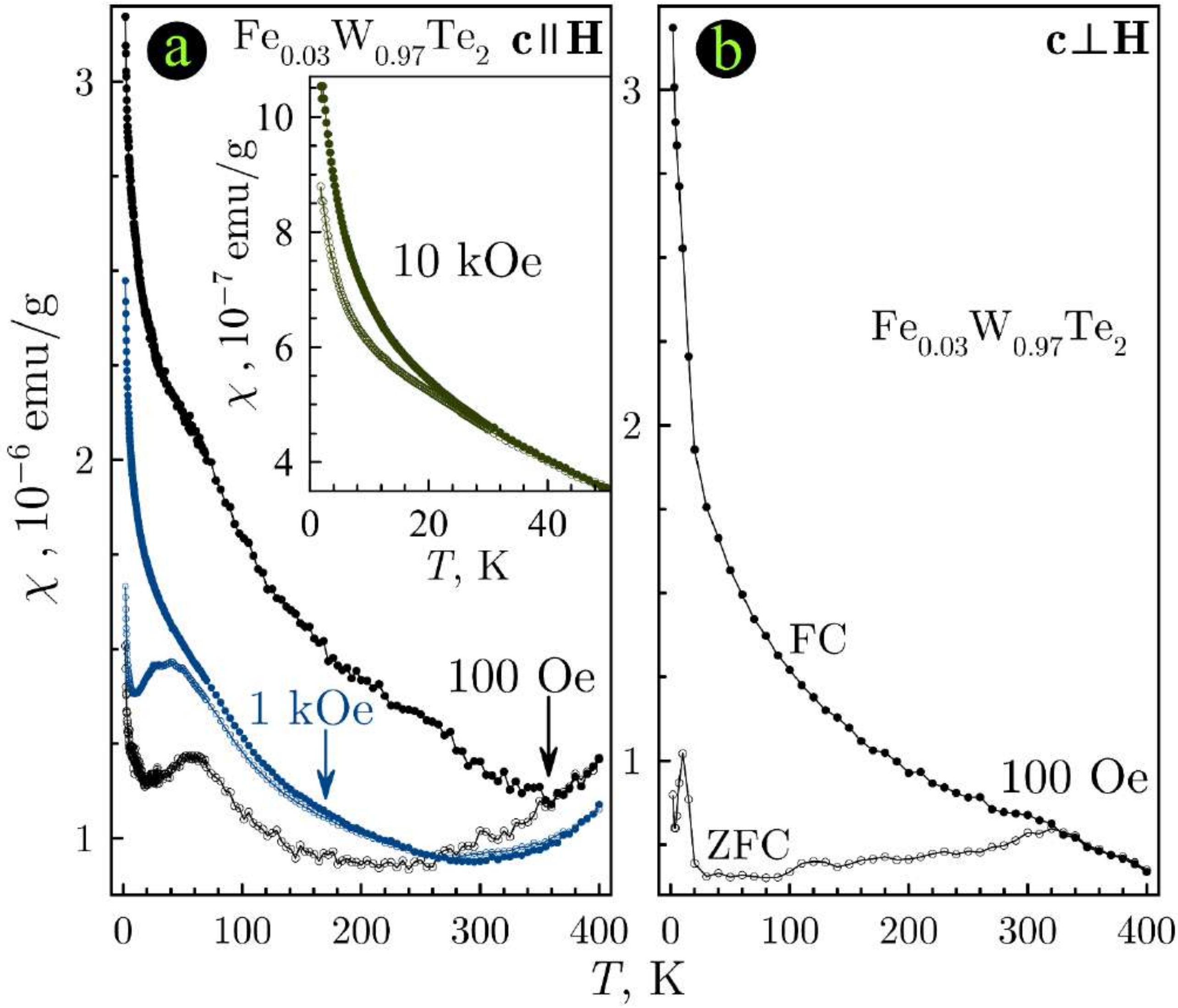


**Fig. 5.2** Temperature dependencies of *dc* magnetic susceptibility for unannealed $Fe_{0.03}W_{0.97}Te_2$. Sample orientations and magnetic field strengths are indicated on the graphs. Open symbols – ZFC. Filled symbols – FC.

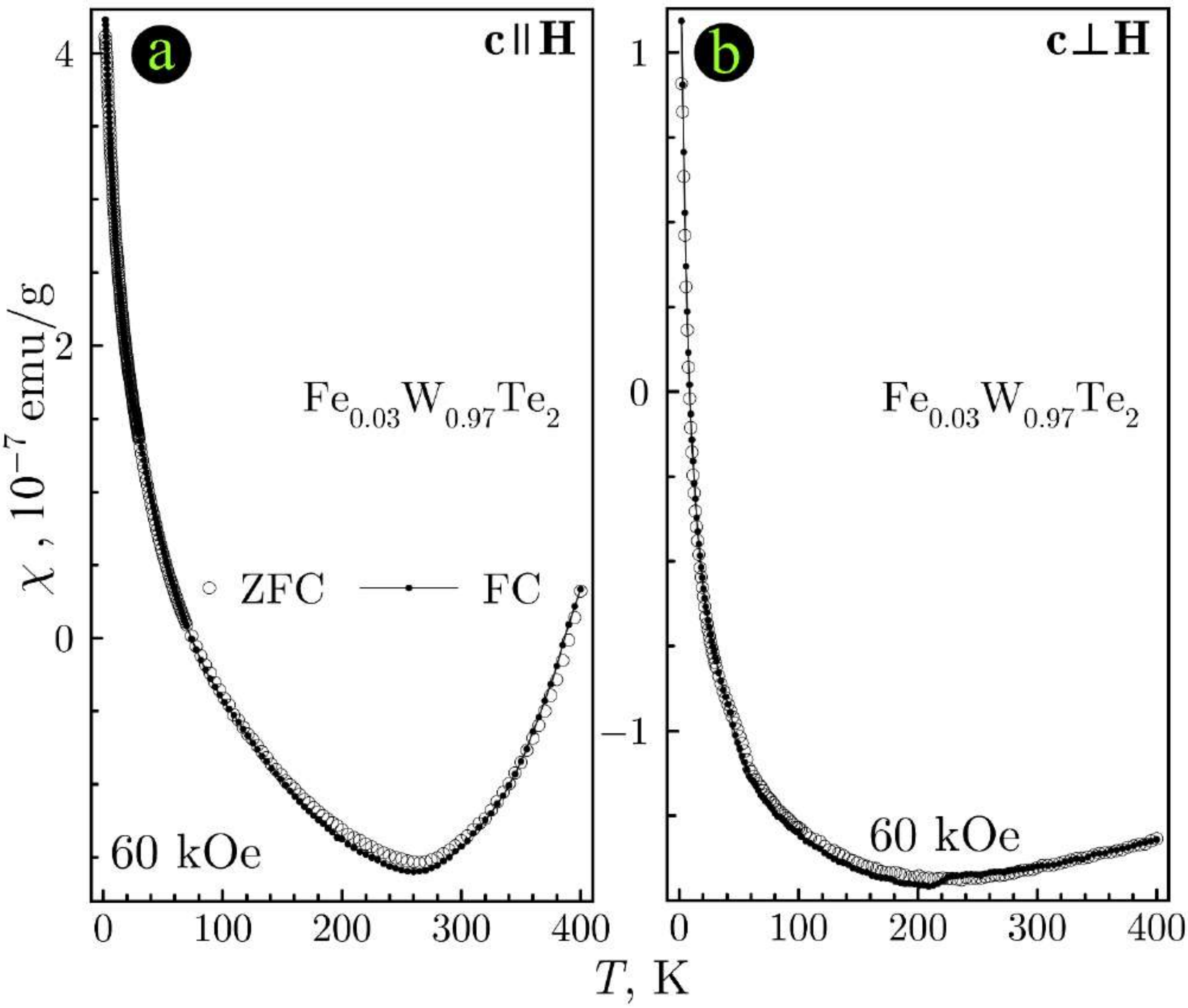


**Fig. 5.3** Temperature dependencies of *dc* magnetic susceptibility for unannealed $Fe_{0.03}W_{0.97}Te_2$. Sample orientations and magnetic field strengths are indicated on the graphs. Open symbols – ZFC. Filled symbols – FC.

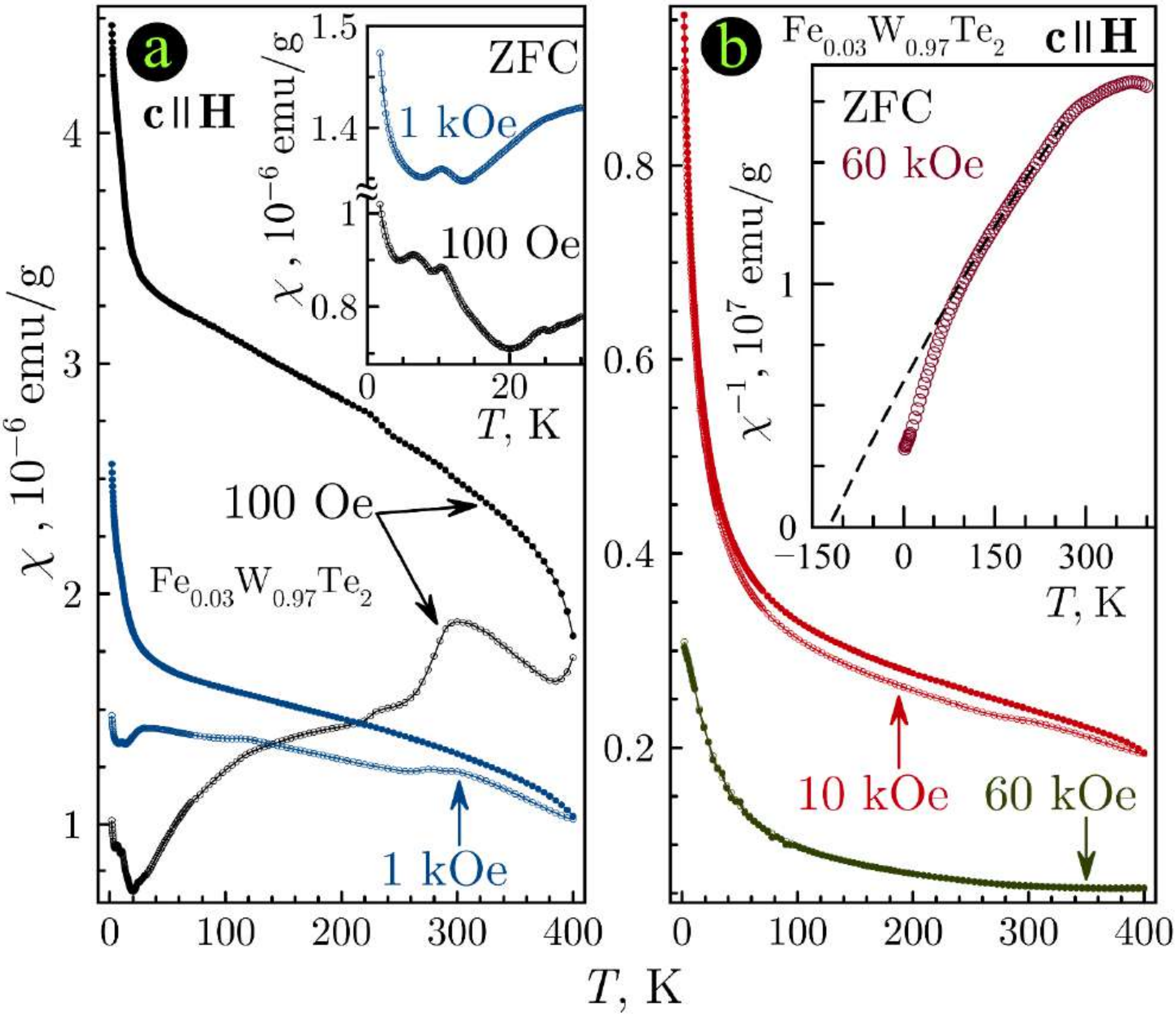


**Fig. 5.4** Temperature dependencies of *dc* magnetic susceptibility for annealed $Fe_{0.03}W_{0.97}Te_2$, measured with **c** || **H** orientation at different fields as indicated on the graphs. The inset to graph (**a**) shows magnetic susceptibility at low temperatures. The inset to graph (**b**) shows inverse magnetic susceptibility $(\chi - \chi_0)^{-1}(T)$. Open symbols – ZFC. Filled symbols – FC.

## 5.3 Magnetization Isotherms of Iron-Doped $WTe_2$ Single Crystals

Magnetization isotherms $M(H)$ for unannealed $Fe_{0.03}W_{0.97}Te_2$ in both **c** || **H** and **c** ⊥ **H** orientations at several temperatures are shown in Fig. 5.5a and b, respectively. The hysteresis loop obtained at 5 K in the **c** || **H** orientation is typical for metamagnetism [129]. The primary and secondary magnetization curves of the hysteresis loop merge with the initial magnetization and with each other at the origin $H = 0$, $M = 0$. The hysteresis loops obtained at 15 K in the **c** || **H** orientation (Fig. 5.5a) and at 2 K in the **c** ⊥ **H** orientation (Fig. 5.5b) exhibit both ferromagnetic and metamagnetic properties. The magnetization isotherms in Fig. 5a and 5b are far from saturation even at a field of 70 kOe. In Fig. 5.5b, the right scale shows that the magnetic moment per iron ion at $T = 2$ K and field strength of 70 kOe is very small, equal to 0.06 $\mu_B$. A similar situation is observed with the annealed $Fe_{0.03}W_{0.97}Te_2$ sample: the magnetic moment under the same conditions equals 0.05 $\mu_B$.

Magnetization isotherms $M(H)$ for the annealed $Fe_{0.03}W_{0.97}Te_2$ sample with **c** || **H** orientation are shown in Fig. 5.6. Hysteresis loops are observed from 2 to 320 K (see lower inset in Fig. 5.6). Unlike the unannealed sample, the annealed $Fe_{0.03}W_{0.97}Te_2$ sample does not show a metamagnetic transition. Thus, magnetic annealing significantly affects the magnetic properties of the sample. The temperature dependence of the coercivity $H_C$, calculated from the loops, is presented in the upper inset of Fig. 5.6. As the temperature decreases, the coercivity of the sample increases, which is typical for ferromagnets.

## 5.4 Heat Capacity of $Fe_{0.03}W_{0.97}Te_2$ Single Crystal

Heat capacity measurements of the unannealed $Fe_{0.03}W_{0.97}Te_2$ single crystal were performed as a function of temperature. The molar heat capacity $C_V$ of the $Fe_{0.03}W_{0.97}Te_2$ single crystal in zero magnetic field is shown in Fig. 5.7. Measurements were also conducted at 0.5 and 1 kOe. The $C/T$ curves as a function of $T^2$, obtained in various magnetic fields, are shown in the inset to Fig. 5.7.

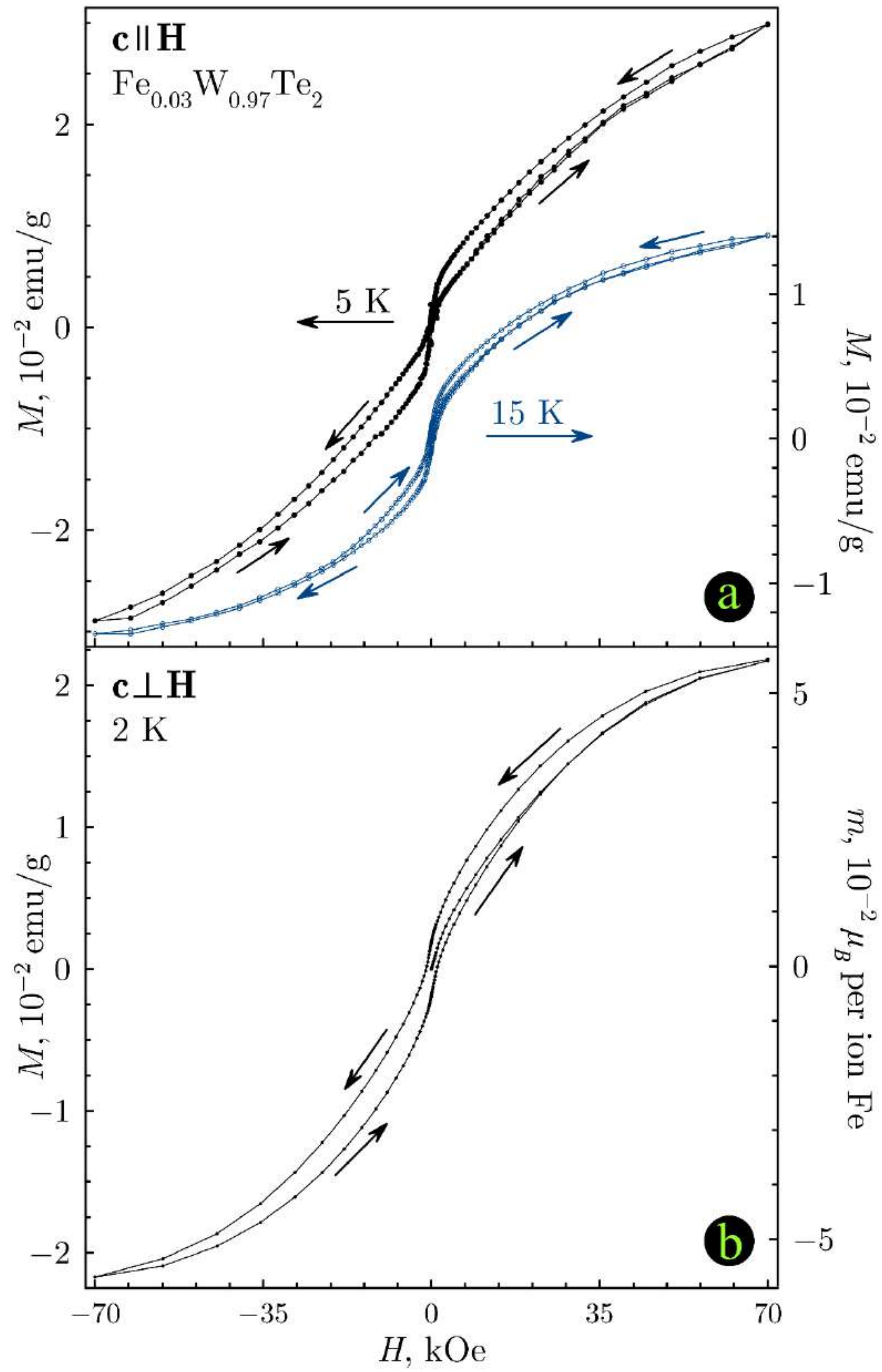


**Fig. 5.5** (**a**) *dc* magnetization isotherms of unannealed $Fe_{0.03}W_{0.97}Te_2$ measured with **c** || **H** orientation. Temperatures are indicated on the graph. (**b**) Magnetization isotherms of unannealed $Fe_{0.03}W_{0.97}Te_2$ in **c** ⊥ **H** orientation at 2 K. Arrows indicate the directions of field change.

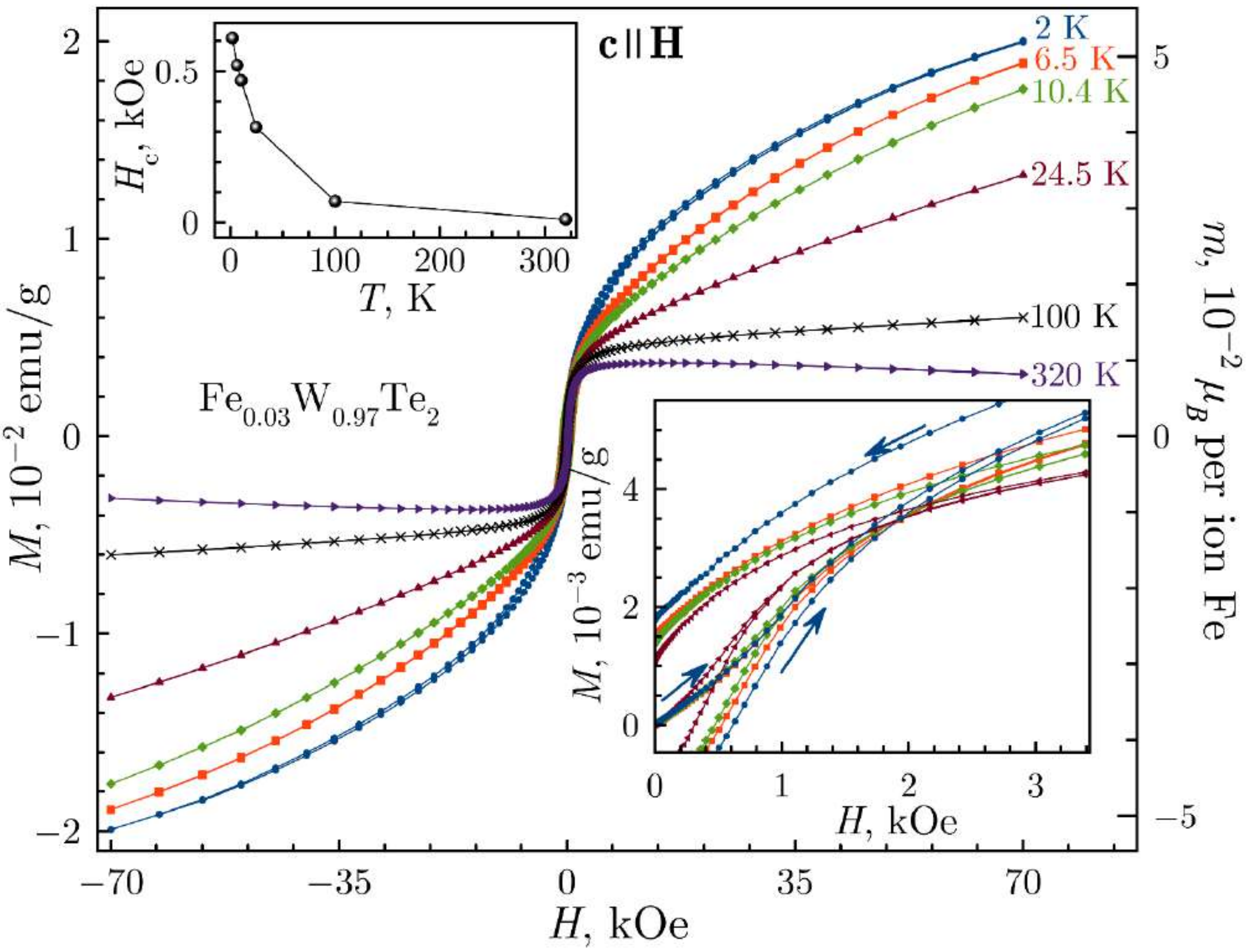


**Fig. 5.6** *dc* magnetization isotherms of annealed $Fe_{0.03}W_{0.97}Te_2$ measured with **c** || **H** orientation at temperatures indicated on the graph. The upper inset shows the temperature dependence of coercivity $H_c(T)$. The lower inset shows the central parts of the isotherms. Arrows indicate the directions of field change.

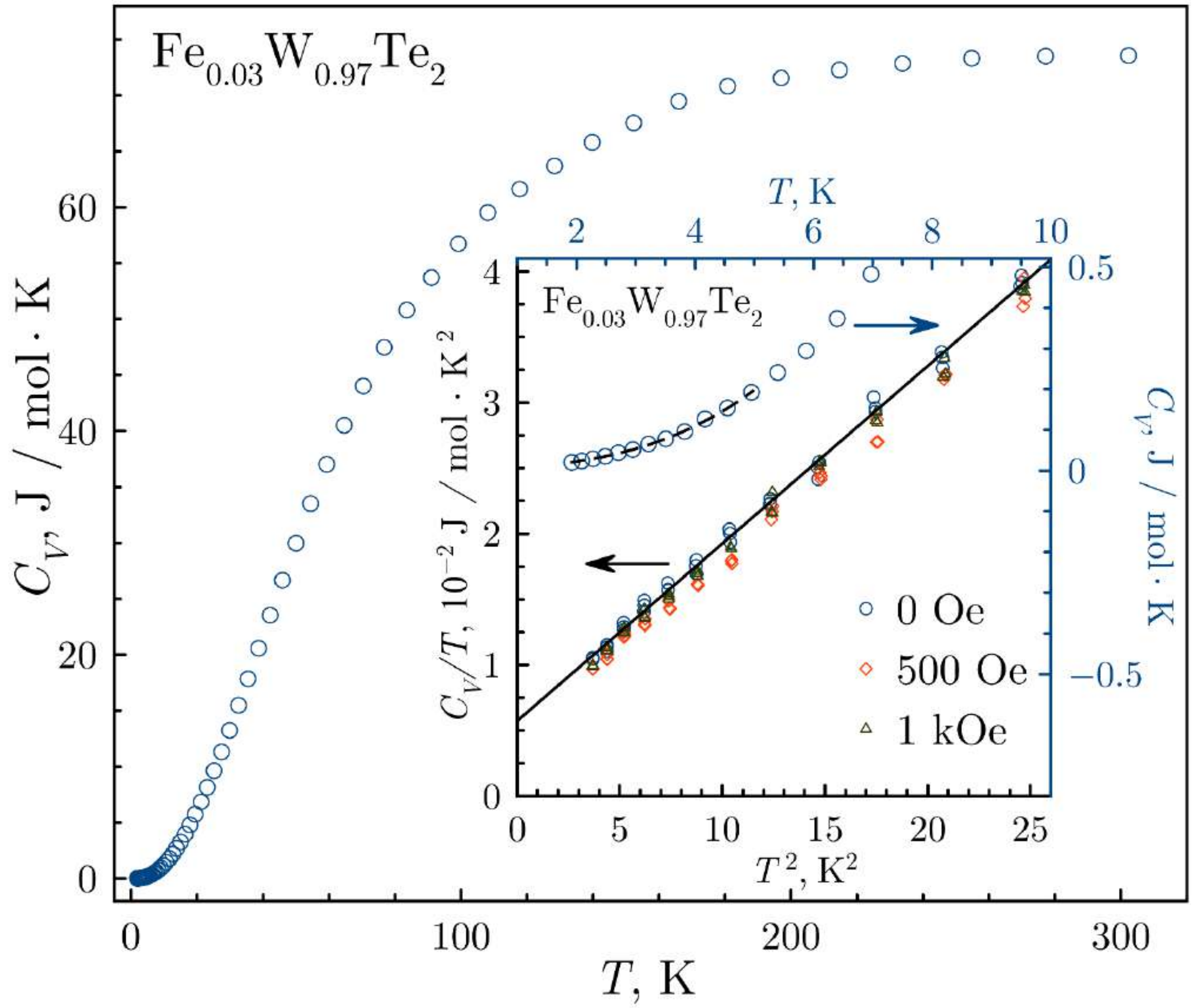


**Fig. 5.7** Temperature dependence of heat capacity $C_V(T)$ for unannealed $Fe_{0.03}W_{0.97}Te_2$, measured in zero magnetic field. The inset shows the $C_V/T(T^2)$ plot and $C_V(T)$ (at low temperatures) with curves measured in zero magnetic field, as well as in fields of 500 Oe and 1 kOe.

The inset graph demonstrates the validity of the dependence $C = \gamma T + \beta T^3$ at low temperatures (in the range 1.9-5 K), which describes the electronic and phonon contributions to heat capacity (dotted line) [90]. The obtained values for the Sommerfeld constant $\gamma$ = 5.7 mJ mol$^{-1}$ K$^{-1}$ and phonon coefficient $\beta$=1.4 mJ mol$^{-1}$ K$^{-4}$ were determined. The Debye temperature θ can be calculated from the coefficient $\beta$: $\theta$ = 161 K. The calculated values of the Sommerfeld constant and Debye temperature are in good agreement with studies of single-crystalline $WTe_2$ reported in [130]. It should be noted that the application of a magnetic field does not have a noticeable effect on the heat capacity in the iron-doped sample.

## 5.5 Discussion

The magnetic properties of undoped $WTe_2$ crystals were studied long before the discovery of their non-trivial topology. It is known that the magnetic susceptibility of $WTe_2$ at room temperature is negative and equals $-1.5 \cdot 10^{-7}$ emu/g [125]. Contributions to magnetic susceptibility come from Pauli paramagnetism (~ 2.2·10–7 emu/g) and large Langevin diamagnetism of $W^{+4}$ and $Te^{-2}$ ionic cores. The total susceptibility found in [125] agrees well with our results obtained at 1 kOe near room temperature (Fig. 5.1a).

The continuous increase in magnetic susceptibility above the minimum around 85 K with increasing temperature, unrelated to magnetic ordering, is likely similar to the behavior of susceptibility curves in some other topological materials.

Minima in temperature dependencies of magnetic susceptibility were observed in type-I Weyl semimetal single crystals of TaAs [127], NbP and TaP [128], as well as in graphene [126]. However, neither undoped nor chromium-doped $WTe_2$ showed similar behavior in zero magnetic field and at 1 kOe [89].

While diamagnetic magnetization is known to be negative and linearly dependent on magnetic field (i.e., magnetic susceptibility $\chi$ = const), some topological materials such as Dirac [126], Luttinger, and Weyl semimetals [127, 128] can exhibit temperature-dependent negative (diamagnetic) susceptibility due to the topological features of electronic bands - linear electron dispersion $E(\mathbf{k})$ near the Fermi level. A characteristic feature of diamagnetism in some Weyl semimetals is the presence of a magnetic susceptibility minimum that depends on the energy of the Weyl point near the Fermi level. The theoretical interpretation developed in [128] predicts, for the specific case of Weyl semimetals, a logarithmic dependence of magnetic susceptibility $\chi = \alpha ln(T) + \chi_0$ at weak fields and sufficiently high temperatures. Here $\alpha$ is a temperature-independent coefficient, and $\chi_0$ is a weak temperature-independent contribution [128]. The fitting of this relationship for $WTe_2$ at 1 kOe is shown in Fig. 5.1a. The agreement between theory and experiment above 250 K is excellent: $\alpha = (2.91 \pm 0.07) \cdot 10^{-8}$ emu/g · K and $\chi_0 = -(3.27 \pm 0.04) \cdot 10^{-7}$ emu/g. A similar model can be used to consider the anomalous increase in magnetic susceptibility at high temperatures in iron-doped $WTe_2$ crystals.

The $Fe_{0.03}W_{0.97}Te_2$ crystals, both unannealed and annealed, demonstrate ferromagnetic ordering, as evidenced by pronounced bifurcations of ZFC and FC curves, unlike undoped $WTe_2$. Annealing of doped crystals enhances ferromagnetism and shifts the phase transition to higher temperatures (Fig. 5.2 and 5.4). Weak magnetic anomalies below room temperature, which became more pronounced after annealing, may arise from antiferromagnetic correlations or charge density waves. Similar multiple magnetization maxima were observed in studies [131, 132] investigating magnetic and transport properties of metallic antiferromagnet $GdTe_3$ with van der Waals structure and frustrated antiferromagnets with spin glass phases [133, 134]. The emergence of the Kondo effect, coexisting with the Weyl semimetal phase, was discovered in transport studies of manganese-doped $VAl_3$ [82]. The Kondo effect may also influence low-temperature magnetism in the studied $Fe_{0.03}W_{0.97}Te_2$ samples. Additional low-temperature anomalies in temperature dependencies of magnetic susceptibility were not observed in Cr-doped $WTe_2$ [89].

The nature of magnetic ordering in doped Weyl semimetals is related to RKKY interaction and Dzyaloshinskii-Moriya interaction [135-137]. A metamagnetic phenomenon of particular interest was observed for the unannealed $Fe_{0.03}W_{0.97}Te_2$ crystal at 5 K with $\mathbf{c} \parallel \mathbf{H}$ orientation. Metamagnetism manifests as a pronounced increase in magnetization in applied magnetic fields. Conventional metamagnetic phenomena occur due to field-induced spin reorientation in antiferromagnets [129] and are associated with the opening of hysteresis loops at threshold fields (spin-flop effect). Recent studies report this type of metamagnetism in topological antiferromagnets [138, 139], as mentioned in the introduction. Itinerant metamagnetism occurs in conductors and is caused by free charge carriers [140, 141]. The hysteresis loops shown in Fig. 5.5 are similar to isotherms exhibited in itinerant metamagnets. Notably, itinerant metamagnetism can be associated with changes in Fermi surface topology [142, 143].

Metamagnetism in the unannealed $Fe_{0.03}W_{0.97}Te_2$ doped sample weakens with increasing temperature (Fig. 5.5a) and in different crystal orientations in the magnetic field (Fig. 5.5b). Annealing completely suppresses metamagnetism in the $Fe_{0.03}W_{0.97}Te_2$ sample (Fig. 5.6). A notable increase in magnetic susceptibility at low temperatures was observed in all three samples ($WTe_2$, unannealed $Fe_{0.03}W_{0.97}Te_2$, and annealed $Fe_{0.03}W_{0.97}Te_2$) (Fig. 5.1-5.4). This might be due to paramagnetism associated with structural defects in the studied samples.

## 5.6 Chapter 5 Conclusions

Studies of magnetic properties of undoped $WTe_2$ single crystal revealed an increase in susceptibility with temperature above 80 K, which was interpreted within the framework of a model developed for type-I Weyl semimetals. Anomalous rises in susceptibility were discovered for iron-doped samples, both annealed and unannealed, at sufficiently high temperatures.

A paramagnetic contribution to magnetic susceptibility, likely caused by growth defects, was observed at low temperatures in both undoped and iron-doped $WTe_2$ crystals. *dc* magnetization measurements demonstrated strong bifurcation of ZFC and FC curves in doped samples, indicating ferromagnetic ordering that was affected by annealing. Anomalies associated with antiferromagnetism were also detected. The magnetic order was suppressed by a magnetic field of 60 kOe.

Anisotropy of magnetic behavior was observed in the doped samples. For the unannealed $Fe_{0.03}W_{0.97}Te_2$ doped crystal, itinerant metamagnetism was discovered at low temperatures for the **c** || **H** orientation. At higher temperatures and different crystal orientation, the metamagnetism weakened and was masked by ferromagnetic ordering.

The magnetic field did not affect the heat capacity of the iron-doped sample, which coincided with the heat capacity of undoped $WTe_2$.

# Chapter 6. Density Functional Theory Study of Structural Stability in $WTe_2$ Systems Doped with Chromium and Iron

In the past decade, the formation energies of transition metals in topological insulator hosts $Bi_2Se_3$ and $Bi_2Te_3$ have been extensively calculated, advancing our understanding of crystal phase stability. However, studies investigating the formation energies of transition metal dopants in the Weyl semimetal $WTe_2$ remain limited. This chapter presents density functional theory (DFT) calculations focused on the structural optimization of $Cr_{0.03}W_{0.97}Te_2$ and $Fe_{0.03}W_{0.97}Te_2$ supercells and the determination of their corresponding dopant formation energies.

## 6.1 Calculation Methodology

*Ab initio* calculations using plane-wave basis sets were carried out with the Quantum ESPRESSO package [144]. To ensure accurate treatment of van der Waals forces, we employed the non-local vdW-DF3-opt2 exchange-correlation functional [145]. The calculations utilized the Projector Augmented Wave (PAW) method [146, 147] and were performed within the Scalar Relativistic Approximation (SRA) framework [148].

The $WTe_2$ unit cell (Fig. 2.3) was optimized using the Broyden-Fletcher-Goldfarb-Shanno (BFGS) algorithm [149, 150]. We set the Hellmann-Feynman force convergence criterion to 0.002 eV/Å [149]. During the optimization process, both ionic positions and cell volumes were allowed to relax. Our calculated lattice parameters for $WTe_2$ (a=3.51 Å, b=6.28 Å, and c=14.07 Å) demonstrate excellent agreement with experimental measurements on $WTe_2$ single crystals (a=3.44 Å, b=6.31 Å, c=14.07 Å) [94, 125].

We applied the same convergence criteria when optimizing 4×2×1 supercells derived from the optimized $WTe_2$ unit cell. Each supercell contained a single dopant atom - either iron (Fe) or chromium (Cr) - substituting one host tungsten (W) atom. This configuration yields approximately 1% magnetic impurity concentration in $TM_{0.03}W_{0.97}Te_2$ (where TM=Cr, Fe). For Brillouin zone integration, we used Γ-centered Monkhorst-Pack grids [151]: 14×9×5 k-points for the $WTe_2$ unit cell and 3×4×3 k-points for the 4×2×1 supercells (96 atoms).

Throughout all calculations, we maintained a plane-wave kinetic energy cutoff $E_{\mathrm{cutwfc}}$ of 50 Ry for electron wave functions. The charge density cutoff $E_{\mathrm{cutrho}}$ was set to 250 Ry.

For electronic state occupancy smearing near the Fermi level, we implemented the Marzari-Vanderbilt scheme, commonly referred to as "cold smearing" [152]. The smearing parameter σ was set to 0.15 eV.

## 6.2 Optimization of Supercells and Formation Energy of Magnetic Ions in $Fe_{0.03}W_{0.97}Te_2$ and $Cr_{0.03}W_{0.97}Te_2$

Figure 6.1 shows the 4×2×1 supercells for $TM_{0.03}W_{0.97}Te_2$ (TM=Cr, Fe), constructed from the optimized $WTe_2$ unit cell. The lattice optimization using the BFGS method results in minor distortion of the crystal structure. The calculated interatomic distances for Cr-Te and Fe-Te are shown in Fig. 6.1 (right).

To verify the thermodynamic stability of the crystal phase, calculations of the impurity formation energy $\Delta H_{\mathrm{f}}$ were performed. $\Delta H_{\mathrm{f}}$ is calculated as the difference between the total energy of the system with defect $E_{\mathrm{tot}}$(TM) and the total energy of the ideal crystal $E_{\mathrm{tot}}$(bulk), corrected for the sum of the products of the number of atoms of each type $n_i$ and their corresponding chemical potentials $\mu_i$:

$$\Delta H_f(\mathrm{TM}) = E_{tot}(\mathrm{TM}) - E_{tot}(\mathrm{bulk}) - \sum_i n_i \mu_i \tag{6.1}$$

The value $n_i$ indicates the number of atoms of type $i$ that were added (positive value) or removed (negative value) during defect formation [90].

Chemical potentials $\mu_{\mathrm{i}}$ for W and Fe elements were calculated based on total energy $E_i$(bulk) calculations, which corresponded to stable crystalline phases. For both mentioned elements, body-centered cubic (BCC) lattices possessing maximum thermodynamic stability were used as reference structures.

The results of calculations of formation energies for Fe and Cr impurities in the $WTe_2$ lattice are presented in Table 6.1. According to these data, the substitution of a tungsten atom with a transition metal atom (Fe or Cr) in a 4×2×1 supercell leads to negative values of impurity formation energies, which corresponds to an energetically favorable state. Thus, it can be concluded that the introduction of small concentrations of Fe and Cr into the tungsten telluride structure does not cause structural instability. On the contrary, the formation of such structures should promote uniform distribution of impurities within the crystal and significantly reduce the probability of undesirable secondary phases formation.

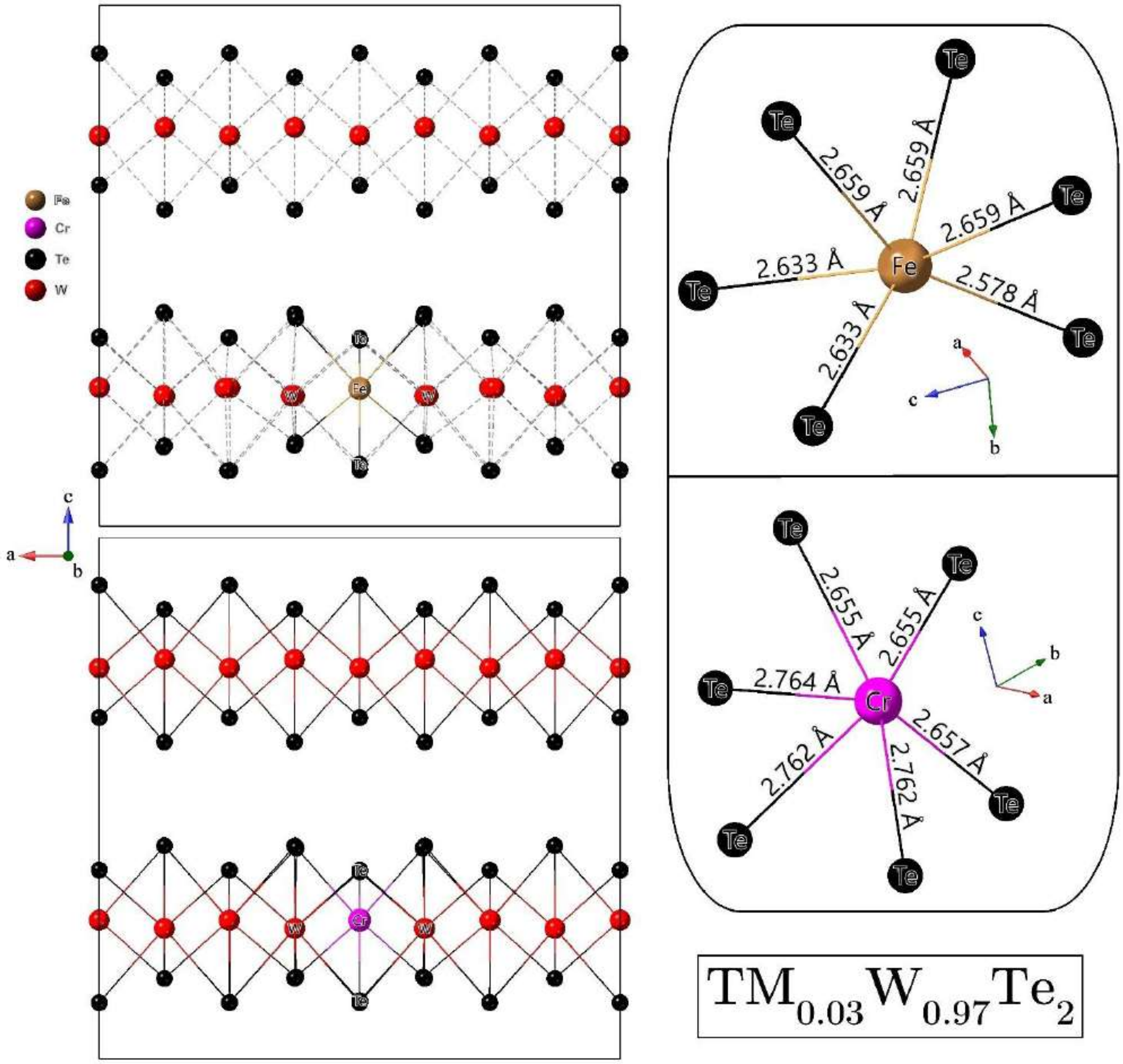


**Fig. 6.1** The 4×2×1 supercells of $TM_{0.03}W_{0.97}Te_2$ (TM=Cr, Fe) are shown on the left. The Fe-Te and Cr-Te distances calculated using the BFGS method are shown on the right.

Table 6.1 Lattice constants $a$, $b$, $c$ of tungsten telluride after structure relaxation, and the calculated formation energy $\Delta H_f$ (TM) of transition metal (TM) impurities substituting a W atom.

| | $WTe_2$ [experiment] | $WTe_2$ [DFT] | $Fe_{0.03}W_{0.97}Te_2$ [DFT] | $Cr_{0.03}W_{0.97}Te_2$ [DFT] |
|---|---|---|---|---|
| $a$, Å | 3.44 Å | 3.51 Å | 3.52 Å | 3.52 Å |
| $b$, Å | 6.31 Å | 6.28 Å | 6.28 Å | 6.28 Å |
| $c$, Å | 14.07 Å | 14.07 Å | 14.07 Å | 14.06 Å |
| $\Delta H_f$ (TM) | – | – | – 1.10 eV | – 0.93 eV |

## 6.3 Chapter 6 Conclusions

Calculations of lattice optimization for $WTe_2$, $Cr_{0.03}W_{0.97}Te_2$, and $Fe_{0.03}W_{0.97}Te_2$ were carried out using the density functional theory method. The calculations showed that chromium and iron doping maintains the stability of $Cr_{0.03}W_{0.97}Te_2$ and $Fe_{0.03}W_{0.97}Te_2$ lattices and should lead to a uniform distribution of impurities. These findings indicate the possibility of precisely tuning magnetic phase states through doping, which opens up prospects for utilizing these systems in spintronics and quantum devices.

# Conclusion

In the present dissertation, the following main results were obtained:

1. As a result of the conducted research, temperature dependencies of magnetic susceptibility and magnetization isotherms were obtained for $\mathbf{Bi_{2-x}Fe_xSe_3}$ (**x = 0.006, 0.03, 0.06**), $\mathbf{Bi_{2-x}Cr_xSe_3}$ (**x = 0.01, 0.03, 0.06**) and $\mathbf{Fe_{0.03}W_{0.97}Te_2}$ single crystals in a wide range of temperatures (1.8–400 K) and magnetic fields up to ±70 kOe. Significant anisotropy of magnetic properties was established for different directions of the magnetic field relative to the crystallographic **c**-axis.

2. Data on coercive forces of the investigated compounds were obtained and analyzed for the first time, revealing a number of anomalies in the behavior of coercive force for $\mathbf{Bi_{2-x}Fe_xSe_3}$ (**x = 0.006, 0.03, 0.06**) and $\mathbf{Bi_{2-x}Cr_xSe_3}$ (**x = 0.01, 0.06**) single crystals. It was shown that competition between ferromagnetic and antiferromagnetic interactions plays an important role in the $\mathbf{Bi_{2-x}Fe_xSe_3}$ system.

3. In $\mathbf{Bi_{2-x}Cr_xSe_3}$ (**x=0.01, 0.03**) and non-annealed $\mathbf{Fe_{0.03}W_{0.97}Te_2}$ single crystals, metamagnetism was discovered, characterized by the opening of magnetization hysteresis loops with increasing external magnetic field. The nature of the field-dependent magnetization corresponded to the phenomenon of itinerant metamagnetism, which is caused by the presence of charge carriers.

4. A sequence of several magnetic phase transitions in $\mathbf{Fe_{0.03}W_{0.97}Te_2}$ single crystal at temperatures below 40 K was revealed for the first time, indicating a complex nature of magnetic ordering.

5. It was established that the temperature dependence of magnetic susceptibility of undoped $WTe_2$ exhibits a minimum at a temperature of about 80 K, which may be related to topological features of the electronic structure.

6. Analysis of effective magnetic moments of impurity atoms showed the presence of mixed valence states $\mathbf{Fe^{3+}}$ and $\mathbf{Fe^{2+}}$ in $\mathbf{Bi_{2-x}Fe_xSe_3}$ single crystals and annealed $\mathbf{Fe_{0.03}W_{0.97}Te_2}$, as well as the presence of chromium ions with $\mathbf{Cr^{2+}}$ valence in $\mathbf{Bi_{2-x}Cr_xSe_3}$ single crystals.

7. Based on heat capacity measurements in magnetic fields for $\mathbf{Bi_{1.94}Fe_{0.06}Se_3}$ and $\mathbf{Fe_{0.03}W_{0.97}Te_2}$ single crystals, it was established that heat capacity curves are described by the Debye model accounting for the electronic contribution. The obtained Debye temperatures and Sommerfeld constants are consistent with literature data for undoped samples. It was shown that the applied magnetic field does not significantly affect the heat capacity of the samples.

The author expresses gratitude to E.V. Charnaya for support, assistance, and discussion of results. The author also thanks E.V. Shevchenko, M.V. Likholetova, I.E. Lezova and A.S. Sakhatsky, through collaboration with whom part of the results was obtained.

## Main Publications on the Dissertation Topic

I. E. V. Shevchenko, A. Sh. Khachatryan, A. O. Antonenko, E. V. Charnaya, S. V. Naumov, V. V. Marchenkov, V. V. Chistyakov, M. K. Lee, L.-J. Chang, "Magnetic Properties of Iron-Doped $Bi_2Se_3$, a Topological Insulator," Physics of the Solid State **61**, 1037 (2019). DOI: [10.1134/S1063783419060234].

II. A. S. Khachatryan, E. V. Charnaya, E. V. Shevchenko, M. V. Likholetova, M. K. Lee, L. J. Chang, S. V. Naumov, A. N. Domozhirova, V. V. Marchenkov, "Coexistence of Magnetic States and Metamagnetism in the $Bi_{2-x}Cr_xSe_3$ Topological Insulators", Europhysics Letters **134**, 47002 (2021). DOI: [10.1209/0295-5075/134/47002].

III. A. S. Khachatryan, E. V. Charnaya, M. V. Likholetova, E. V. Shevchenko, M. K. Lee, L.-J. Chang, S. V. Naumov, A. N. Perevalova, E. B. Marchenkova, V. V. Marchenkov, "Magnetic Studies of Iron-Doped Probable Weyl Semimetal $WTe_2$", Condensed Matter **8**, 6 (2023). DOI: [10.3390/condmat8010006].

IV. A. Sh. Khachatryan, E. V. Charnaya, V. V. Marchenkov, "Investigation of Magnetic Phase Transitions in Transition Metal-Doped $Bi_2Se_3$ Topological Insulators", XXIII All-Russian Youth Conference on Semiconductor Physics and Nanostructures, Semiconductor Opto- and Nanoelectronics, Saint Petersburg, Russia, November 22-26, 2021, Abstract Book, p. 20 (2021).

V. A. Sh. Khachatryan, E. V. Charnaya, V. V. Marchenkov, "Magnetic Phase Transitions in Topological Insulators $Bi_{2-x}T_xSe_3$ (T=Fe, Cr)", XXIV Ural International Winter School on Semiconductor Physics, Yekaterinburg, Russia, February 14-19, 2022, Abstract Book, p. 183 (2022).

VI. A. Sh. Khachatryan, E. V. Charnaya, V. V. Marchenkov, "Magnetic Properties of $Bi_{2-x}Cr_xSe_3$ Topological Insulators with x=0.1, 0.3, and 0.6", IX International Youth Scientific Conference Dedicated to the 100th Anniversary of Professor S. P. Raspopin, Yekaterinburg, Russia, February 14-19, 2022, Abstract Book, p. 210 (2022).

VII. A. Sh. Khachatryan, E. V. Charnaya, V. V. Marchenkov, "Magnetic Phase Transitions in Iron-Doped Weyl Semimetal $WTe_2$", XIX Conference "Strongly Correlated Electronic Systems and Quantum Critical Phenomena", Moscow, Russia, May 26, 2022, Abstract Book, p. 60 (2022).

VIII. A. Sh. Khachatryan, E. V. Charnaya, V. V. Marchenkov, "Magnetic Properties of Iron-Doped Weyl Semimetal $WTe_2$", Proceedings of the VII Euro-Asian Symposium "Trends in MAGnetism", Kazan, Russia, August 22-26, 2022, Abstract Book, p. 225 (2022).

# References


1. Hasan, M. Z. Colloquium: Topological insulators / M. Z. Hasan, C. L. Kane // Rev. Mod. Phys. — 2010. – Vol. 82. - № 4. – P. 3045-3067.
2. Armitage, N. P. Weyl and Dirac semimetals in three-dimensional solids / N. P. Armitage, E. J. Mele, A. Vishwanath // Rev. Mod. Phys. – 2018. – Vol. 90. - № 1. – P. 015001.
3. Lv, B. Q. Experimental perspective on three-dimensional topological semimetals / B. Q. Lv, T. Qian, H. Ding // Rev. Mod. Phys. – 2021. – Vol. 93. - № 2. – P. 025002.
4. Shi, W.-J. Converting normal insulators into topological insulators via tuning orbital levels / W.-J. Shi, J. Liu, Y. Xu, S.-J. Xiong, J. Wu, W. Duan // Phys. Rev. B. – 2015. – Vol. 92 - № 20. – P. 205118.
5. Ando, Y. Topological insulator materials // J. Phys. Soc. Jpn. – 2013. – Vol. 82. - № 10. – P. 102001.
6. Pariari, A. K. Atoms to topological electronic materials: A bedtime story for beginners // Indian J. Phys. – 2021. – Vol. 95. - № 12. – P. 2639-2660.
7. Kawamura, M. Topological quantum phase transition in magnetic topological insulator upon magnetization rotation / M. Kawamura, M. Mogi, R. Yoshimi, A. Tsukazaki, Y. Kozuka, K. S. Takahashi, M. Kawasaki, Y. Tokura // Phys. Rev. B. – 2018. – Vol. 98. - № 14. – P. 140404.
8. Chang, C.-Z. Experimental observation of the quantum anomalous hall effect in a magnetic topological insulator / C.-Z. Chang, J. Zhang, X. Feng, J. Shen, Z. Zhang, M. Guo, K. Li, Y. Ou, P. Wei, L.-L. Wang, Z.-Q. Ji, Y. Feng, S. Ji, X. Chen, J. Jia, X. Dai, Z. Fang, S.-C. Zhang, K. He, Y. Wang, L. Lu, X.-C. Ma, Q.-K. Xue // Science. – 2013. – Vol. 340. - № 6129. – P. 167-170.
9. Yu, R. Quantized anomalous hall effect in magnetic topological insulators / R. Yu, W. Zhang, H.-J. Zhang, S.-C. Zhang, X. Dai, Z. Fang // Science. – 2010. – Vol. 329. - № 5987. – P. 61-64.

10. Chang, C.-Z. Colloquium: Quantum anomalous Hall effect / C.-Z. Chang, C.-X. Liu, A. H. MacDonald // Rev. Mod. Phys. – 2023. – Vol. 95. - № 1. – P. 011002.
11. Chen, Y. L. Experimental realization of a three-dimensional topological insulator, $Bi_2Te_3$ / Y. L. Chen, J. G. Analytis, J.-H. Chu, Z. K. Liu, S.-K. Mo, X. L. Qi, H. J. Zhang, D. H. Lu, X. Dai, Z. Fang, S. C. Zhang, I. R. Fisher, Z. Hussain, Z.-X. Shen // Science. – 2009. – Vol. 325. - № 5937. – P. 178-181.
12. Desvignes, L. Tunable high speed atomic rotor in $Bi_2Se_3$ revealed by current noise / L. Desvignes, V. S. Stolyarov, M. Aprili, F. Massee // ACS Nano. – 2021. – Vol. 15. - № 1. – P. 1421-1425.
13. Qi, X.-L. Topological field theory of time-reversal invariant insulators / X.-L. Qi, T. L. Hughes, S.-C. Zhang // Phys. Rev. B. – 2008. – Vol. 78. - № 19. – P. 195424.
14. Xia, Y. Observation of a large-gap topological-insulator class with a single Dirac cone on the surface / Y. Xia, D. Qian, D. Hsieh, L. Wray, A. Pal, H. Lin, A. Bansil, D. Grauer, Y. S. Hor, R. J. Cava, M. Z. Hasan // Nature Phys. – 2009. – Vol. 5. - № 6. – P. 398-402.
15. Zhang, H. Topological insulators in $Bi_2Se_3$, $Bi_2Te_3$ and $Sb_2Te_3$ with a single Dirac cone on the surface / H. Zhang, C.-X. Liu, X.-L. Qi, X. Dai, Z. Fang, S.-C. Zhang // Nature Phys. – 2009. – Vol. 5. - № 6. – P. 438-442.
16. Chotorlishvili, L. Magnetic fluctuations in topological insulators with ordered magnetic adatoms: Cr on $Bi_2Se_3$ from first principles / L. Chotorlishvili, A. Ernst, V. K. Dugaev, A. Komnik, M. G. Vergniory, E. V. Chulkov, J. Berakdar // Phys. Rev. B. – 2014. – Vol. 89. - № 7. – P. 075103.
17. Kim, J. Magnetic phase transition in Fe-doped topological insulator $Bi_2Se_3$ / J. Kim, S.-H. Jhi // Phys. Rev. B. – 2015. – Vol. 92. - № 10. – P. 104405.
18. Zhang, J.-M. Tailoring Magnetic doping in the topological insulator $Bi_2Se_3$ / J.-M. Zhang, W. Zhu, Y. Zhang, D. Xiao, Y. Yao // Phys. Rev. Lett. – 2012. – Vol. 109. - № 26. – P. 266405.
19. Zhang, J.-M. Stability, electronic, and magnetic properties of the magnetically doped topological insulators $Bi_2Se_3$, $Bi_2Te_3$, and $Sb_2Te_3$ / J.-M. Zhang, W. Ming,

Z. Huang, G.-B. Liu, X. Kou, Y. Fan, K. L. Wang, Y. Yao // Phys. Rev. B. – 2013. – Vol. 88. - № 23. – P. 235131.

20. Zhu, J.-J. Electrically Controllable Surface Magnetism on the surface of topological insulators / J.-J. Zhu, D.-X. Yao, S.-C. Zhang, K. Chang // Phys. Rev. Lett. – 2011. – Vol. 106. - № 9. – P. 097201.
21. Zhang, X. Carrier free long-range magnetism in Mo doped one quintuple layer $Bi_2Te_3$ and $Sb_2Te_3$ / X. Zhang, J. Zhu // J. Phys.: Condens. Matter. – 2020. – Vol. 32. - № 6. – P. 065801.
22. Liu, Q. Magnetic impurities on the surface of a topological insulator / Q. Liu, C.-X. Liu, C. Xu, X.-L. Qi, S.-C. Zhang // Phys. Rev. Lett. – 2009. – Vol. 102. - №15. – P. 156603.
23. Wang, D. First-principles study of electronic, magnetic and optical properties of N doping topological insulator $Bi_2Se_3$ / D. Wang, M. Zhang, L. Liu, X. An, X. Ma, Y. Luo, T. Song // Superlattices Microstruct. – 2019. – Vol. 132. - № 8. – P. 106161.
24. Qi, S. Nonmagnetic doping induced quantum anomalous Hall effect in topological insulators / S. Qi, R. Gao, M. Chang, T. Hou, Y. Han, Z. Qiao // Phys. Rev. B. – 2020. – Vol. 102. - № 8. – P. 085419.
25. Zhao, W. Berry phase in quantum oscillations of topological materials / W. Zhao, X. Wang // Adv. Phys.: X. – 2022. – Vol. 7. - № 1. – P. 2064230.
26. Soluyanov, A. A. Type-II Weyl semimetals / A. A. Soluyanov, D. Gresch, Z. Wang, Q. Wu, M. Troyer, X. Dai, B. A. Bernevig // Nature. – 2015. – Vol. 527. - № 7579. – P. 495-498.
27. Lv, B. Q. Observation of Fermi-arc spin texture in TaAs / B. Q. Lv, S. Muff, T. Qian, Z.D. Song, S. M. Nie, N. Xu, P. Richard, C.E. Matt, N. C. Plumb, L. X. Zhao, G. F. Chen, Z. Fang, X. Dai, J. H. Dil, J. Mesot, M. Shi, H. M. Weng, H. Ding // Phys. Rev. Lett. – 2015. – Vol. 115. - № 21. – P. 217601.
28. Wan, X. Topological semimetal and Fermi-arc surface states in the electronic structure of pyrochlore iridates / X. Wan, A. M. Turner, A. Vishwanath, S. Y. Savrasov // Phys. Rev. B. – 2011. – Vol. 83. - № 20. – P. 205101.

29. Xu, G. Chern semimetal and the quantized anomalous hall effect in $HgCr_2Se_4$ / G. Xu, H. Weng, Z. Wang, X. Dai, Z. Fang // Phys. Rev. Lett. – 2011. – Vol. 107. - № 18. – P. 186806.

30. Wang, Z. Time-reversal-breaking Weyl fermions in magnetic Heusler alloys / Z. Wang, M. G. Vergniory, S. Kushwaha, M. Hirschberger, E. V. Chulkov, A. Ernst, N. P. Ong, R.J. Cava, B. A. Bernevig // Phys. Rev. Lett. – 2016. – Vol. 117. - № 23. – P. 236401.

31. Xu, S.-Y. Discovery of a Weyl fermion semimetal and topological Fermi arcs / S.-Y. Xu, I. Belopolski, N. Alidoust, M. Neupane, G. Bian, C. Zhang, R. Sankar, G. Chang, Z. Yuan, C.-C. Lee, S.-M. Huang, H. Zheng, J. Ma, D. S. Sanchez, B. Wang, A. Bansil, F. Chou, P. P. Shibayev, H. Lin, S. Jia, M. Z. Hasan // Science. – 2015. – Vol. 349. - № 6248. – P. 613-617.

32. Lv, B. Q. Experimental discovery of Weyl semimetal TaAs / B. Q. Lv, H. M. Weng, B. B. Fu, X. P. Wang, H. Miao, J. Ma, P. Richard, X. C. Huang, L. X. Zhao, G. F. Chen, Z. Fang, X. Dai, T. Qian, H. Ding // Phys. Rev. X. – 2015. – Vol. 5. - № 3. – P. 031013.

33. Weng, H. Weyl semimetal phase in noncentrosymmetric transition-metal monophosphides / H. Weng, C. Fang, Z. Fang, B.A. Bernevig, X. Dai // Phys. Rev. X. – 2015. – Vol. 5. - № 1. – P. 011029.

34. Huang, S.-M. A Weyl Fermion semimetal with surface Fermi arcs in the transition metal monopnictide TaAs class / S.-M. Huang, S.-Y. Xu, I. Belopolski, C.-C. Lee, G. Chang, B. Wang, N. Alidoust, G. Bian, M. Neupane, C. Zhang, S. Jia, A. Bansil, H. Lin, M.Z. Hasan // Nat. Commun. – 2015. – Vol. 6 - № 1. – P. 7373.

35. Deng, K. Experimental observation of topological Fermi arcs in type-II Weyl semimetal $MoTe_2$ / K. Deng, G. Wan, P. Deng, K. Zhang, S. Ding, E. Wang, M. Yan, H. Huang, H. Zhang, Z. Xu, J. Denlinger, A. Fedorov, H. Yang, W. Duan, H. Yao, Y. Wu, S. Fan, H. Zhang, X. Chen, S. Zhou // Nature Phys. – 2016. – Vol. 12. - № 12. – P. 1105-1110.

36. Huang, L. Spectroscopic evidence for a type II Weyl semimetallic state in $MoTe_2$ / L. Huang, T. M. McCormick, M. Ochi, Z. Zhao, M.-T. Suzuki, R. Arita, Y. Wu,

D. Mou, H. Cao, J. Yan, N. Trivedi, A. Kaminski // Nature Mater. – 2016. – Vol. 15. - № 11. – P. 1155-1160.

37. Liang, A. Electronic evidence for Type II Weyl semimetal state in $MoTe_2$ / A. Liang, J. Huang, S. Nie, Y. Ding, Q. Gao, C. Hu, S. He, Y. Zhang, C. Wang, B. Shen, J. Liu, P. Ai, L. Yu, X. Sun, W. Zhao, S. Lv, D. Liu, C. Li, Y. Zhang, Y. Hu, Y. Xu, L. Zhao, G. Liu, Z. Mao, X. Jia, F. Zhang, S. Zhang, F. Yang, Z. Wang, Q. Peng, H. Weng, X. Dai, Z. Fang, Z. Xu, C. Chen, X. J. Zhou // arXiv. – 2016. – arXiv: 1604.01706.
38. Tamai, A. Fermi arcs and their topological character in the candidate type-II Weyl semimetal $MoTe_2$ / A. Tamai, Q. S. Wu, I. Cucchi, F. Y. Bruno, S. Riccò, T. K. Kim, M. Hoesch, C. Barreteau, E. Giannini, C. Besnard, A. A. Soluyanov, F. Baumberger // Phys. Rev. X. – 2016. – Vol. 6. - № 3. – P. 031021.
39. Jiang, J. Signature of type-II Weyl semimetal phase in $MoTe_2$ / J. Jiang, Z. K. Liu, Y. Sun, H. F. Yang, C. R. Rajamathi, Y. P. Qi, L. X. Yang, C. Chen, H. Peng, C.-C. Hwang, S. Z. Sun, S.-K. Mo, I. Vobornik, J. Fujii, S. S. P. Parkin, C. Felser, B. H. Yan, Y. L. Chen // Nat. Commun. – 2017. – Vol. 8. - № 1. – P. 13973.
40. Wang, C. Observation of Fermi arc and its connection with bulk states in the candidate type-II Weyl semimetal $WTe_2$ / C. Wang, Y. Zhang, J. Huang, S. Nie, G. Liu, A. Liang, Y. Zhang, B. Shen, J. Liu, C. Hu, Y. Ding, D. Liu, Y. Hu, S. He, L. Zhao, L. Yu, J. Hu, J. Wei, Z. Mao, Y. Shi, X. Jia, F. Zhang, S. Zhang, F. Yang, Z. Wang, Q. Peng, H. Weng, X. Dai, Z. Fang, Z. Xu, C. Chen, X.J. Zhou // Phys. Rev. B. – 2016. – Vol. 94. - № 24. – P. 241119.
41. Lin, C.-L. Scanning tunneling spectroscopy studies of topological materials / C.-L. Lin, N. Kawakami, R. Arafune, E. Minamitani, N. Takagi // J. Phys.: Condens. Matter. – 2020. – Vol. 32. - № 24. – P. 243001.
42. Belopolski, I. Discovery of a new type of topological Weyl fermion semimetal state in $Mo_xW_{1-x}Te_2$ / I. Belopolski, D. S. Sanchez, Y. Ishida, X. Pan, P. Yu, S.-Y. Xu, G. Chang, T.-R. Chang, H. Zheng, N. Alidoust, G. Bian, M. Neupane, S.-M. Huang, C.-C. Lee, Y. Song, H. Bu, G. Wang, S. Li, G. Eda, H.-T. Jeng, T.

Kondo, H. Lin, Z. Liu, F. Song, S. Shin, M. Z. Hasan // Nat. Commun. – 2016. – Vol. 7. - № 1. – P. 13643.

43. Belopolski, I. Fermi arc electronic structure and Chern numbers in the type-II Weyl semimetal candidate $Mo_xW_{1-x}Te_2$ / I. Belopolski, S.-Y. Xu, Y. Ishida, X. Pan, P. Yu, D. S. Sanchez, H. Zheng, M. Neupane, N. Alidoust, G. Chang, T.-R. Chang, Y. Wu, G. Bian, S.-M. Huang, C.-C. Lee, D. Mou, L. Huang, Y. Song, B. Wang, G. Wang, Y.-W. Yeh, N. Yao, J. E. Rault, P. Le Fèvre, F. Bertran, H.-T. Jeng, T. Kondo, A. Kaminski, H. Lin, Z. Liu, F. Song, S. Shin, M. Z. Hasan // Phys. Rev. B. – 2016. – Vol. 94. - № 8. – P. 085127.
44. Xu, S.-Y. Discovery of Lorentz-violating type II Weyl fermions in LaAlGe / S.-Y. Xu, N. Alidoust, G. Chang, H. Lu, B. Singh, I. Belopolski, D. S. Sanchez, X. Zhang, G. Bian, H. Zheng, M.-A. Husanu, Y. Bian, S.-M. Huang, C.-H. Hsu, T.-R. Chang, H.-T. Jeng, A. Bansil, T. Neupert, V. N. Strocov, H. Lin, S. Jia, M. Z. Hasan // Sci. Adv. – 2017. – Vol. 3. - № 6. – P. e1603266.
45. Bruno, F.Y. Observation of large topologically trivial Fermi arcs in the candidate type-II Weyl semimetal $WTe_2$ / F.Y. Bruno, A. Tamai, Q.S. Wu, I. Cucchi, C. Barreteau, A. de la Torre, S. McKeown Walker, S. Riccò, Z. Wang, T.K. Kim, M. Hoesch, M. Shi, N.C. Plumb, E. Giannini, A.A. Soluyanov, F. Baumberger // Phys. Rev. B. – 2016. – Vol. 94. - № 12. – P. 121112.
46. Li, P. Evidence for topological type-II Weyl semimetal WTe2 / P. Li, Y. Wen, X. He, Q. Zhang, C. Xia, Z.-M. Yu, S.A. Yang, Z. Zhu, H.N. Alshareef, X.-X. Zhang // Nat. Commun. – 2017. – Vol. 8. - № 1. – P. 2150.
47. Wang, Y. J. Planar Hall effect in type-II Weyl semimetal $WTe_2$ / Y. J. Wang, J. X. Gong, D. D. Liang, M. Ge, J. R. Wang, W. K. Zhu. – 2018. – arXiv:1801.05929.
48. Antonenko, A. O. $^{125}$Te spin-lattice relaxation in a candidate to Weyl semimetals $WTe_2$ / A. O. Antonenko, E. V. Charnaya, A. L. Pirozerskii, D. Yu. Nefedov, M. K. Lee, L. J. Chang, J. Haase, S. V. Naumov, A. N. Domozhirova, V. V. Marchenkov // Results in Phys. – 2021. – Vol. 21. - № 2. – P. 103793.

49. Kabashima, S. Electrical properties of tungsten-ditelluride $WTe_2$ // J. Phys. Soc. Jpn. – 1966. – Vol. 21. - № 5. – P. 945-948.
50. Wu, Y. Temperature-induced Lifshitz transition in $WTe_2$ / Y. Wu, N.H. Jo, M. Ochi, L. Huang, D. Mou, S.L. Bud’ko, P.C. Canfield, N. Trivedi, R. Arita, A. Kaminski // Phys. Rev. Lett. – 2015. – Vol. 115. - № 16. – P. 166602.
51. Ali, M. N. Large, non-saturating magnetoresistance in $WTe_2$ / M. N. Ali, J. Xiong, S. Flynn, J. Tao, Q. D. Gibson, L. M. Schoop, T. Liang, N. Haldolaarachchige, M. Hirschberger, N. P. Ong, R. J. Cava // Nature. – 2014. – Vol. 514. - № 7521. – P. 205-208.
52. Pirozerskii, A. L. Magnetoresistance and quantum oscillations in $WTe_2$ semimetal / A. L. Pirozerskii, E. V. Charnaya, M. K. Lee, L.-J. Chang, S. V. Naumov, A. N. Domozhirova, V. V. Marchenkov // Phys. Solid State. – 2022. – Vol.64. - №2. – P. 80-84.
53. He, P. Nonlinear magnetotransport shaped by Fermi surface topology and convexity / P. He, C.-H. Hsu, S. Shi, K. Cai, J. Wang, Q. Wang, G. Eda, H. Lin, V.M. Pereira, H. Yang // Nat. Commun. – 2019. – Vol.10. - №1. – P. 1290.
54. Fei, Z. Ferroelectric switching of a two-dimensional metal / Z. Fei, W. Zhao, T. A. Palomaki, B. Sun, M. K. Miller, Z. Zhao, J. Yan, X. Xu, D. H. Cobden // Nature. – 2018. – Vol. 560. - № 7718. – P. 336-339.
55. Ji, S. Manipulation of stacking order in *Td*-$WTe_2$ by ultrafast optical excitation / S. Ji, O. Grånäs, J. Weissenrieder // ACS Nano. – 2021. – Vol. 15. - № 5. – P. 8826-8835.
56. Zhao, C. Strain tunable semimetal–topological-insulator transition in monolayer *1T′*-$WTe_2$ / C. Zhao, M. Hu, J. Qin, B. Xia, C. Liu, S. Wang, D. Guan, Y. Li, H. Zheng, J. Liu, J. Jia // Phys. Rev. Lett. – 2020. – Vol. 125. - № 4. – P. 046801.
57. Jia, Y. Evidence for a monolayer excitonic insulator / Y. Jia, P. Wang, C.-L. Chiu, Z. Song, G. Yu, B. Jäck, S. Lei, S. Klemenz, F. A. Cevallos, M. Onyszczak, N. Fishchenko, X. Liu, G. Farahi, F. Xie, Y. Xu, K. Watanabe, T. Taniguchi, B. A. Bernevig, R. J. Cava, L. M. Schoop, A. Yazdani, S. Wu // Nat. Phys. – 2022. – Vol. 18. - № 1. – P. 87-93.

58. Li, J. Proximity-magnetized quantum spin Hall insulator: monolayer 1*T′* $WTe_2/Cr_2Ge_2Te_6$ / J. Li, M. Rashetnia, M. Lohmann, J. Koo, Y. Xu, X. Zhang, K. Watanabe, T. Taniguchi, S. Jia, X. Chen, B. Yan, Y.-T. Cui, J. Shi // Nat. Commun. – 2022. – Vol. 13. - № 1. – P. 5134.
59. Kohno, H. Spintronics with Weyl semimetal // JPSJ News Comments. – 2021. - № 18. – P. 13.
60. Yang, S. A. Dirac and Weyl materials: Fundamental aspects and some spintronics applications // SPIN. – 2016. – Vol. 6. - № 2. – P. 1640003.
61. Rubel, M. H. K. Crystal structures and properties of nanomagnetic materials. in fundamentals of low dimensional magnets / M. H. K. Rubel, M. K. Hossain. – 1st ed. – Boca Raton: CRC Press, 2022. – P. 183-205.
62. Pesin, D. Spintronics and pseudospintronics in graphene and topological insulators / D. Pesin, A. H. MacDonald // Nature Mater. – 2012. – Vol. 11. - № 5. – P. 409-416.
63. Choi, J. Magnetic and transport properties of Mn-doped $Bi_2Se_3$ and $Sb_2Se_3$ / J. Choi, H.-W. Lee, B.-S. Kim, H. Park, S. Choi, S. C. Hong, S. Cho // J. Magn. & Magn. Mat. – 2006. – Vol. 304. - № 1. – P. e164.
64. Maurya, V. K. High spin state driven magnetism and thermoelectricity in Mn doped topological insulator $Bi_2Se_3$ / V. K. Maurya, C. L. Dong, C. L. Chen, K. Asokan, S. Patnaik // J. Magn. & Magn. Mat. – 2018. – Vol. 456. - № 10. – P. 1-5.
65. Hor, Y. S. Development of ferromagnetism in the doped topological insulator $Bi_{2-x}Mn_xTe_3$ / Y. S. Hor, P. Roushan, H. Beidenkopf, J. Seo, D. Qu, J.G. Checkelsky, L.A. Wray, D. Hsieh, Y. Xia, S.-Y. Xu, D. Qian, M. Z. Hasan, N. P. Ong, A. Yazdani, R. J. Cava // Phys. Rev. B. – 2010. – Vol. 81. - № 19. – P. 195203.
66. Yang, H. Growth and magnetic properties of Ni-doped $Bi_2Se_3$ topological insulator crystals / H. Yang, L.G. Liu, M. Zhang, X.S. Yang // Solid State Commun. – 2016. – Vol. 241. - № 5. – P. 26.

67. Zhang, M. Anomalous second ferromagnetic phase transition in $Co_{0.08}Bi_{1.92}Se_3$ topological insulator / M. Zhang, L. Liu, H. Yang // J. Alloys Compd. – 2016. – Vol. 678. - № 12. – P. 463.
68. Li, H. Carrier density dependence of the magnetic properties in iron-doped $Bi_2Se_3$ topological insulator / H. Li, Y. R. Song, M.-Y. Yao, F. Zhu, C. Liu, C. L. Gao, J.-F. Jia, D. Qian, X. Yao, Y. J. Shi, D. Wu // J. Appl. Phys. – 2013. – Vol. 113. - № 4. – P. 043926.
69. Choi, Y. H. Transport and magnetic properties of Cr-, Fe-, Cu-doped topological insulators / Y. H. Choi, N. H. Jo, K. J. Lee, J. B. Yoon, C. Y. You, M. H. Jung // J. Appl. Phys. – 2011. – Vol. 109. - № 7. – P. 07E312.
70. Yee, M.M. Spin-polarized quantum well states on $Bi_{2-x}Fe_xSe_3$ / M.M. Yee, Z.-H. Zhu, A. Soumyanarayanan, Y. He, C.-L. Song, E. Pomjakushina, Z. Salman, A. Kanigel, K. Segawa, Y. Ando, J.E. Hoffman // Phys. Rev. B. – 2015. – Vol. 91. - № 16. – P. 161306.
71. Haazen, P. P. J. Ferromagnetism in thin-film Cr-doped topological insulator $Bi_2Se_3$ / P. P. J. Haazen, J.-B. Laloë, T. J. Nummy, H. J. M. Swagten, P. Jarillo-Herrero, D. Heiman, J. S. Moodera // Appl. Phys. Lett. – 2012. – Vol. 100. - № 8. – P. 082404.
72. Collins-McIntyre, L. J. Magnetic ordering in Cr-doped $Bi_2Se_3$ thin films / L. J. Collins-McIntyre, S. E. Harrison, P. Schönherr, N.-J. Steinke, C. J. Kinane, T. R. Charlton, D. Alba-Veneroa, A. Pushp, A. J. Kellock, S. S. P. Parkin, J. S. Harris, S. Langridge, G. van der Laan, T. Hesjedal // EPL. – 2014. – Vol. 107. - № 5. – P. 57009.
73. Cermak, P. Thermoelectric and magnetic properties of Cr-doped single crystal $Bi_2Se_3$ – Search for energy filtering / P. Cermak, P. Ruleova, V. Holy, J. Prokleska, V. Kucek, K. Palka, L. Benes, C. Drasar // Journal of Solid State Chemistry. – 2018. – Vol. 258. - № 10. – P. 768-775.
74. Baker, A. A. Magnetic proximity-enhanced Curie temperature of Cr-doped $Bi_2Se_3$ thin films / A. A. Baker, A. I. Figueroa, K. Kummer, L. J. Collins-McIntyre, T. Hesjedal, G. van der Laan // Phys. Rev. B. – 2015. – Vol. 92. - № 9. – P. 094420.

75. Ptok, A. Electronic properties of $Bi_2Se_3$ dopped by 3d transition metal (Mn, Fe, Co, or Ni) ions / A. Ptok, K.J. Kapcia, A. Ciechan // J. Phys.: Condens. Matter. – 2021. – Vol. 33. - № 6. – P. 065501.
76. Salman, Z. The nature of magnetic ordering in magnetically doped topological insulator $Bi_{2-x}Fe_xSe_3$ / Z. Salman, E. Pomjakushina, V. Pomjakushin, A. Kanigel, K. Chashka, K. Conder, E. Morenzoni, T. Prokscha, K. Sedlak, A. Suter // arXiv:1203.4850 [Cond-Mat]. – 2012.
77. Dyck, J. S. Low-temperature ferromagnetic properties of the diluted magnetic semiconductor $Sb_{2-x}Cr_xTe_3$ / J. S. Dyck, Č. Drašar, P. Lošt'ák, C. Uher // Phys. Rev. B. – 2005. – Vol. 71. - № 11. – P. 115214.
78. Maurya, V. K. Magnetotransport and Berry phase in magnetically doped $Bi_{0.97-x}Sb_{0.03}$ single crystals / V. K. Maurya, M. M. Patidar, A. Dhaka, R. Rawat, V. Ganesan, R. S. Dhaka // Phys. Rev. B. – 2020. – Vol. 102. - № 14. – P. 144412.
79. Chen, F. C. Superconductivity enhancement in the S-doped Weyl semimetal candidate $MoTe_2$ / F. C. Chen, X. Luo, R. C. Xiao, W. J. Lu, B. Zhang, H. X. Yang, J. Q. Li, Q. L. Pei, D. F. Shao, R. R. Zhang, L. S. Ling, C. Y. Xi, W. H. Song, Y. P. Sun // Appl. Phys. Lett. – 2016. – Vol. 108. - № 16. – P. 162601.
80. Mandal, M. Superconductivity in doped Weyl semimetal $Mo_{0.9}Ir_{0.1}Te_2$ with broken inversion symmetry / M. Mandal, C. Patra, A. Kataria, S. Paul, S. Saha, R. P. Singh // Supercond. Sci. Technol. – 2022. – Vol. 35. - № 2. – P. 025011.
81. Deng, M.-X. Weyl semimetal induced from a Dirac semimetal by magnetic doping / M.-X. Deng, W. Luo, R.-Q. Wang, L. Sheng, D. Y. Xing // Phys. Rev. B. – 2017. – Vol. 96. - № 15. – P. 155141.
82. Lee, K.-Y. Coexistence of Kondo effect and Weyl semimetallic states in Mn-doped $Mn_xVAl_3$ compounds / K.-Y. Lee, J.-H. Yun, J. H. Kim, Y. A. Salawu, H.-J. Kim, J. J. Lee, H. Lee, J.-S. Rhyee // Mater. Today Phys. – 2022. – Vol. 26. - № 9. – P. 100732.
83. Singh, A. Evolution of extremely large magnetoresistance in a Weyl semimetal, $WTe_2$ with Ni-doping / A. Singh, S. Sasmal, K. K. Iyer, A. Thamizhavel, K. Maiti // Phys. Rev. Materials. – 2022. – Vol. 6. - № 12. – P. 124202.

84. Kumar, N. Topological quantum materials from the viewpoint of chemistry / N. Kumar, S. N. Guin, K. Manna, C. Shekhar, C. Felser // Chem. Rev. – 2021. – Vol. 121. - № 5. – P. 2780.
85. Lin, E.-C. Enhanced magnetoresistance of doped $WTe_2$ Single Crystals / E.-C. Lin, Y.-T. Lin, C.-T. Chou, C.-A. Chen, Y.-J. Wu, P.-H. Chen, S.-F. Lee, C.-S. Chang, Y.-F. Chen, Y.-H. Lee // ACS Appl. Electron. Mater. – 2022. – Vol. 4. - № 8. – P. 4540.
86. Zhu, L. Superconductivity in potassium-intercalated *Td*-$WTe_2$ / L. Zhu, Q.-Y. Li, Y. Lv, S. Li, X.-Y. Zhu, Z.-Y. Jia, Y.B. Chen, J. Wen, S.-C. Li // Nano Lett. – 2018. – Vol. 18. - № 9. – P. 6585.
87. Basnet, R. Transport properties of Fe-doped type-II Weyl semimetal $WTe_2$ / R. Basnet, K. Pandey, G. Acharya, M.R.U. Nabi, A. Wegner, J. Hu // Bull. Am. Phys. Soc. – 2021. – Vol. 66. - № 1.
88. Basnet, R. Metal-insulator transition in Fe-doped type-II Weyl semimetal $WTe_2$ / R. Basnet, K. Pandey, G. Acharya, M.R.U. Nabi, A. Wegner, C.B. Stephenson, S. Bishop, J. Hu // Bull. Am. Phys. Soc. – 2022. – Vol. 67. - № 3.
89. Yang, L. Highly Tunable near-room temperature ferromagnetism in Cr-Doped Layered *Td*-$WTe_2$ / L. Yang, H. Wu, L. Zhang, W. Zhang, L. Li, K. Sugawara, T. Sato, G. Zhang, P. Gao, Y. Muhammad, X. Wen, B. Tao, F. Guo, H. Chang // Adv. Funct. Mater. – 2021. – Vol. 31. - № 13. – P. 2008116.
90. Quinn, J. J., Yi, K.-S. Solid State Physics: Principles and Modern Applications / J. J. Quinn, K.-S. Yi. – Springer. – 2009. – 527 p.
91. Bridgman, P.W. Certain physical properties of single crystal of tungsten, antimony, bismuth, tellurium, cadmium, zinc and tin // Proc. Amer. Acad. Arts and Sci. – 1925. – Vol. 60. – P. 305.
92. Stockbarger, D. C. The production of large single crystals of lithium fluoride / D.C. Stockbarger // Rev. of Sc. Instr. – 1936. – Vol. 7. – P. 133.
93. Lévy, F. Single-crystal growth of layered crystals // Il Nuovo Cimento B. – 1977. – Vol. 38. – P. 359.

94. Perevalova, A. N. Electronic Transport in a Topological Semimetal $WTe_2$ Single Crystal / A. N. Perevalova, S. V. Naumov, S. M. Podgornykh, V. V. Chistyakov, E. B. Marchenkova, B. M. Fominykh, V. V. Marchenkov // Physics of Metals and Metallography. – 2023. – Vol. 123. – № 11. – C. 1061.

95. Lewis, L. H. A sample holder design and calibration technique for the quantum design magnetic properties measurement system superconducting quantum interference device magnetometer / L. H. Lewis, K. M. Bussmann // Rev. Sci. Instrum. – 1996. – Vol. 67. - № 10. – P. 3537.

96. Hwang, J. S. Measurement of heat capacity by fitting the whole temperature response of a heat-pulse calorimeter / J. S. Hwang, K. J. Lin, C. Tien // Rev. Sci. Instrum. – 1997. – Vol. 68. - № 1. – P. 94.

97. Lashley, J. C. Critical examination of heat capacity measurements made on a quantum design physical property measurement system / J. C. Lashley, M.F. Hundley, A. Migliori, J. L. Sarrao, P. G. Pagliuso, T. W. Darling, M. Jaime, J. C. Cooley, W. L. Hults, L. Morales, D. J. Thoma, J. L. Smith, J. Boerio-Goates, B. F. Woodfield, G. R. Stewart, R. A. Fisher, N. E. Phillips // Cryogenics. – 2003. – Vol. 43. - № 6. – P. 369.

98. Wang, G. Electronic structure of the thermoelectric materials $Bi_2Te_3$ and $Sb_2Te_3$ from first-principles calculations / G. Wang, T. Cagin // Phys. Rev. B. – 2007. – Vol. 76. - № 7. – P. 075201.

99. Brown, B. E. The crystal structures of $WTe_2$ and high-temperature $MoTe_2$ / B. E. Brown // Acta Cryst. – 1966. – Vol. 20. - № 2. – P. 268.

100. Kang, D. Superconductivity emerging from a suppressed large magnetoresistant state in tungsten ditelluride / D. Kang, Y. Zhou, W. Yi, C. Yang, J. Guo, Y. Shi, S. Zhang, Z. Wang, C. Zhang, S. Jiang, A. Li, K. Yang, Q. Wu, G. Zhang, L. Sun, Z. Zhao // Nat. Commun. – 2015. – Vol. 6. - № 1. – P. 7804.

101. Pan, X.-C. Pressure-driven dome-shaped superconductivity and electronic structural evolution in tungsten ditelluride / X.-C. Pan, X. Chen, H. Liu, Y. Feng, Z. Wei, Y. Zhou, Z. Chi, L. Pi, F. Yen, F. Song, X. Wan, Z. Yang, B. Wang, G. Wang, Y. Zhang // Nat. Commun. – 2015. – Vol. 6. - № 1. – P. 7805.

102. Mugiraneza, S. Tutorial: A beginner's guide to interpreting magnetic susceptibility data with the Curie-Weiss law / S. Mugiraneza, A. M. Hallas // Commun. Phys. – 2022. – Vol. 5. - № 1. – P. 95.

103. Shevchenko, E. V. Magnetic Properties of Iron-Doped $Bi_2Se_3$, a Topological Insulator / E. V. Shevchenko, A. Sh. Khachatryan, A. O. Antonenko, E. V. Charnaya, S. V. Naumov, V. V. Marchenkov, V. V. Chistyakov, M. K. Lee, L.-J. Chang // Phys. Solid State – 2019. – Vol. 61. - № 6. – P. 1037 – 1042.

104. Tichý, L. Nonparabolicity of the conduction band and anisotropy of the electron effective mass in *n*-$Bi_2Se_3$ single crystals / L. Tichý, J. Horák // Phys. Rev. B. – 1979. – Vol. 19. - № 2. – P. 1126-1131.

105. Hyde, G. R. Electronic properties of $Bi_2Se_3$ crystals / G. R. Hyde, H. A. Beale, I. L. Spain // J. Phys. Chem. Solids. – 1974. – Vol. 35. - № 4. – P. 1719.

106. R. M. White. Quantum Theory of Magnetism / Robert M. White. – Springer Nature, 2007. - 365 c.

107. Shoemake, G. E. Specific heat of *n*- and *p*-Type $Bi_2Te_3$ from 1.4 to 90°K / G. E. Shoemake, J. A. Rayne // Phys. Rev. – 1969. – Vol. 185. - № 3. – P. 1046.

108. Story, T. Carrier-concentration – induced ferromagnetism in PbSnMnTe / T. Story, R.R. Gałązka, R.B. Frankel, P.A. Wolff // Phys. Rev. Lett. – 1986. – Vol. 56. - № 7. – P. 777–779.

109. Islam, F. Role of Magnetic defects in tuning ground states of magnetic topological insulators / F. Islam, Y. Lee, D. M. Pajerowski, J. Oh, W. Tian, L. Zhou, J. Yan, L. Ke, R. J. McQueeney, D. Vaknin // Adv. Mater. – 2023. – Vol. 35. - № 21. – P. 2209951.

110. Lv, L. Observation of nano-scaled defects in Fe doped $Bi_2Se_3$ topological insulator crystal / L. Lv, D. Zhou, M. Zhang, L. Yang, X. Yang, Y. Zhao // Mater. Lett. – 2013. – Vol. 99. - № 5. – P. 118-121.

111. Kander, N. S. The effect of Fe-doping on structural, elemental, magnetic, and weak anti-localization properties of $Bi_2Se_3$ topological insulator / N. S. Kander, S. Islam, S. Guchhait, A. K. Das // Appl. Phys. A. – 2023. – Vol. 129. - № 3. – P. 253.

112. Vonsovsky, S.V. Magnetism / S.V. Vonsovsky. – M.: Nauka, 1984. – 1032 p.

113. Khachatryan, A. Sh. Coexistence of magnetic states and metamagnetism in the $Bi_{2-x}Cr_xSe_3$ topological insulators / A. Sh. Khachatryan, E. V. Charnaya, E. V. Shevchenko, M. V. Likholetova, M. K. Lee, L. J. Chang, S. V. Naumov, A. N. Domozhirova, V. V. Marchenkov // EPL. – 2021. – Vol. 134. - № 4. – P. 47002.

114. R. White, Long Rage Order in Solids / Robert M. White, Theodore H. Geballe – Academic Press, 1979. - 414 c.

115. Larson, P. Electronic structure and magnetism in $Bi_2Te_3$, $Bi_2Se_3$, and $Sb_2Te_3$ doped with transition metals (Ti–Zn) / P. Larson, W. R. L. Lambrecht // Phys. Rev. B. – 2008. – Vol. 78. - № 19. – P. 195207.

116. Abdalla, L. B. Topological insulator $Bi_2Se_3$ (111) surface doped with transition metals: An ab initio investigation / L. B. Abdalla, L. Seixas, T. M. Schmidt, R. H. Miwa, A. Fazzio // Phys. Rev. B. – 2013. – Vol. 88. - № 4. – P. 045312.

117. Figueroa, A. I. Magnetic Cr doping of $Bi_2Se_3$: Evidence for divalent Cr from x-ray spectroscopy / A. I. Figueroa, G. van der Laan, L. J. Collins-McIntyre, S.-L. Zhang, A. A. Baker, S. E. Harrison, P. Schönherr, G. Cibin, T. Hesjedal. // Phys. Rev. B. – 2014. – Vol. 90. - № 13. – P. 134402.

118. Figueroa, A. I. Local Structure and bonding of transition metal dopants in $Bi_2Se_3$ topological insulator thin films / A. I. Figueroa, G. van der Laan, L. J. Collins-McIntyre, G. Cibin, A. J. Dent, T. Hesjedal // J. Phys. Chem. C. – 2015. – Vol. 119. - № 30. – P. 17344-17351.

119. Kul’bachinskii, V. A. Low-temperature ferromagnetism in a new diluted magnetic semiconductor $Bi_{2-x}Fe_xTe_3$ / V. A. Kul’bachinskii, A. Yu. Kaminskii, K. Kindo, Y. Narumi, K. Suga, P. Lostak, P. Svanda // JETP Lett. – 2001. – Vol. 73. - № 7. – P. 352-356.

120. Diop, L. V. B. Multiple magnetization steps and plateaus across the antiferromagnetic to ferromagnetic transition in $La_{1-x}Ce_xFe_{12}B_6$: Time delay of the metamagnetic transitions / L. V. B. Diop, O. Isnard // Phys. Rev. B. – 2018. – Vol. 97. - № 1. – P. 014436.

121. Singh, N.K. Itinerant electron metamagnetism and magnetocaloric effect in $RCo_2$-based Laves phase compounds / N.K. Singh, K.G. Suresh, A.K. Nigam, S.K. Malik, A.A. Coelho, S. Gama // J. Magn. & Magn. Mater. – 2007. – Vol. 317. - № 1. – P. 68.

122. Wada, H. High-field transport properties of itinerant electron metamagnetic $Co(S_{1-x}Se_x)_2$ / H. Wada, Y. Maekawa, D. Kawasaki // J. Sci-Adv. Mater. Dev. – 2016. – Vol. 1. - № 2. – P. 179.

123. Fujita, A. Itinerant electron metamagnetic transition in $La(Fe_xSi_{1-x})_{13}$ intermetallic compounds / A. Fujita, Y. Akamatsu, K. Fukamichi // J. Appl. Phys. – 1999. – Vol. 85. - № 8. – P. 4756.

124. Khachatryan, A. S. Magnetic Studies of Iron-Doped Probable Weyl Semimetal $WTe_2$ / A. S. Khachatryan, E. V. Charnaya, M. V. Likholetova, E. V. Shevchenko, M. K. Lee, L.-J. Chang, S. V. Naumov, A. N. Perevalova, E. B. Marchenkova, V. V. Marchenkov // Condensed Matter – 2023. – Vol. 8. - № 1. – P. 6.

125. Mar, A. Metal-metal vs tellurium-tellurium bonding in $WTe_2$ and its ternary variants $TaIrTe_4$ and $NbIrTe_4$ / A. Mar, S. Jobic, J.A. Ibers // J. Am. Chem. Soc. – 1992. – Vol. 114. - № 23. – P. 8963.

126. Li, Z. Field and temperature dependence of intrinsic diamagnetism in graphene: Theory and experiment / Z. Li, L. Chen, S. Meng, L. Guo, J. Huang, Y. Liu, W. Wang, X. Chen // Phys. Rev. B. – 2015. – Vol. 91. - № 9. – P. 094429.

127. Liu, Y. Intrinsic diamagnetism in the Weyl semimetal TaAs / Y. Liu, Z. Li, L. Guo, X. Chen, Y. Yuan, F. Liu, S. Prucnal, M. Helm, S. Zhou // J. Magn. & Magn. Mat. – 2016. – Vol. 408. - № 6. – P. 73.

128. Leahy, I. A. Nonsaturating large magnetoresistance in semimetals / I. A. Leahy, Y.-P. Lin, P. E. Siegfried, A. C. Treglia, J. C. W. Song, R. M. Nandkishore, M. Lee // Proc. Natl. Acad. Sci. U.S.A. – 2018. – Vol. 115. - № 42. – P. 10570.

129. Stryjewski, E. Metamagnetism / E. Stryjewski, N. Giordano // Adv. Phys. – 1977. – Vol. 26. - № 5. – P. 487.

130. Callanan, J. E. Thermodynamic properties of tungsten ditelluride ($WTe_2$) I. The preparation and low temperature heat capacity at temperatures from 6 K to 326 K

/ J. E. Callanan, G. A. Hope, R. D. Weir, E. F. Westrum // J. Chem. Thermodyn. – 1992. – Vol. 24. - № 6. – P. 627.

131. Lei, S. High mobility in a van der Waals layered antiferromagnetic metal / S. Lei, J. Lin, Y. Jia, M. Gray, A. Topp, G. Farahi, S. Klemenz, T. Gao, F. Rodolakis, J. L. McChesney, C. R. Ast, A. Yazdani, K. S. Burch, S. Wu, N. P. Ong, L. M. Schoop // Sci. Adv. – 2020. – Vol. 6. - № 6. – P. eaay6407.
132. Guo, Q. Novel magnetic behavior of antiferromagnetic $GdTe_3$ induced by magnetic field / Q. Guo, D. Bao, L. J. Zhao, S. Ebisu // Physica B: Condensed Matter. – 2021. – Vol. 617. - № 9. – P. 413153.
133. Pakhira, S. Large magnetic cooling power involving frustrated antiferromagnetic spin-glass state in $R_2NiSi_3$ (R=Gd, Er) / S. Pakhira, C. Mazumdar, R. Ranganathan, S. Giri, M. Avdeev // Phys. Rev. B. – 2016. – Vol. 94. - № 10. – P. 104414.
134. Pal, S. Memorylike response of the magnetic glass / S. Pal, K. Kumar, A. Banerjee // Phys. Rev. B. – 2021. – Vol. 103. - № 14. – P. 144434.
135. Wang, S.-X. RKKY interaction in three-dimensional electron gases with linear spin-orbit coupling / S.-X. Wang, H.-R. Chang, J. Zhou // Phys. Rev. B. – 2017. – Vol. 96. - № 11. – P. 115204.
136. Araki, Y. Spin textures and spin-wave excitations in doped Dirac-Weyl semimetals / Y. Araki, K. Nomura // Phys. Rev. B. – 2016. – Vol. 93. - № 9. – P. 094438.
137. Hosseini, M. V. Ruderman-Kittel-Kasuya-Yosida interaction in Weyl semimetals / M. V. Hosseini, M. Askari // Phys. Rev. B. – 2015. – Vol. 92. - № 22. – P. 224435.
138. Tan, A. Metamagnetism of weakly coupled antiferromagnetic topological insulators / A. Tan, V. Labracherie, N. Kunchur, A. U. B. Wolter, J. Cornejo, J. Dufouleur, B. Büchner, A. Isaeva, R. Giraud // Phys. Rev. Lett. – 2020. – Vol. 124. - № 19. – P. 197201.

139. Lei, C. Metamagnetism of few-layer topological antiferromagnets / C. Lei, O. Heinonen, A. H. MacDonald, R. J. McQueeney // Phys. Rev. Materials. – 2021. – Vol. 5. - № 6. – P. 064201.

140. Levitin, R. Z. Itinerant metamagnetism / R. Z. Levitin, A. S. Markosyan // Soviet Physics Uspekhi. – 1988. – Vol. 31. – №. 4. – P. 730.

141. Leithe-Jasper, A. Weak itinerant ferromagnetism and electronic and crystal structures of alkali-metal iron antimonides: $NaFe_4Sb_{12}$ and $KFe_4Sb_{12}$ / A. Leithe-Jasper, W. Schnelle, H. Rosner, M. Baenitz, A. Rabis, A. A. Gippius, E. N. Morozova, H. Borrmann, U. Burkhardt, R. Ramlau, U. Schwarz, J. A. Mydosh, Y. Grin, V. Ksenofontov, S. Reiman // Phys. Rev. B. – 2004. – Vol. 70. - № 21. – P. 214418.

142. Yamaji, Y. Quantum metamagnetic transitions induced by changes in fermi-surface topology: Applications to a weak itinerant-electron ferromagnet $ZrZn_2$ / Y. Yamaji, T. Misawa, M. Imada // J. Phys. Soc. Jpn. – 2007. – Vol. 76. - № 6. – P. 063702.

143. Chen, W. Local electron correlation effects on the fermiology of the weak itinerant ferromagnet $ZrZn_2$ / W. Chen, A. D. N. James, S. B. Dugdale // Electron. Struct. – 2022. – Vol. 4. - № 4. – P. 045002.

144. Giannozzi, P. QUANTUM ESPRESSO: A modular and open-source software project for quantum simulations of materials / P. Giannozzi, S. Baroni, N. Bonini, M. Calandra, R. Car, C. Cavazzoni, D. Ceresoli, G. L. Chiarotti, M. Cococcioni, I. Dabo, A. Dal Corso, S. De Gironcoli, S. Fabris, G. Fratesi, R. Gebauer, U. Gerstmann, C. Gougoussis, A. Kokalj, M. Lazzeri, L. Martin-Samos, N. Marzari, F. Mauri, R. Mazzarello, S. Paolini, A. Pasquarello, L. Paulatto, C. Sbraccia, S. Scandolo, G. Sclauzero, A. P. Seitsonen, A. Smogunov, P. Umari, R. M. Wentzcovitch // J. Phys.: Condens. Matter. – 2009. – Vol. 21. - № 39. – P. 395502.

145. Lee K. Higher-accuracy van der Waals density functional / É.D. Murray, L. Kong, B.I. Lundqvist, D.C. Langreth // Phys. Rev. B – 2010. Vol. 82, - № 8, – P. 081101.

146. Blöchl, P. E. Projector augmented-wave method // Phys. Rev. B. – 1994. – Vol. 50. - № 24. – P. 17953.

147. Jollet F. Generation of Projector Augmented-Wave atomic data: A 71 element validated table in the XML format / F. Jollet, M. Torrent, N. Holzwarth // Comput. Phys. Commun. – 2014. – Vol. 185. - № 4. – P. 1246.
148. Takeda, T. The scalar relativistic approximation // Z Physik B. – 1978. – Vol. 32. - № 1. – P. 43.
149. Hung, N. T. Quantum ESPRESSO course for solid-state physics / N. T. Hung, A. R. T. Nugraha, R. Saito. – Jenny Stanford Publishing. – 2023. – 361 p.
150. Yuan Y. A modified BFGS algorithm for unconstrained optimization / Y. Yuan // IMA J. Numer. Anal. – 1991. – Vol. 11. - № 10. – P. 325.
151. Monkhorst H. J. Special points for Brillouin-zone integrations / H. J. Monkhorst, J. D. Pack // Phys. Rev. B – 1976. – Vol. 13. - № 12. – P. 5188.
152. Marzari N. Thermal contraction and disordering of the Al (110) surface / N. Marzari, D. Vanderbilt, A. De Vita, M. C. Payne // Phys. Rev. Lett. – 1999. – Vol. 82. - № 16. – P. 3296.